Thesis presented to the Instituto Tecnológico de Aeronáutica, in partial fulfillment of the requirements for the degree of Doctor of Science in the Graduate Program of Physics, Field of Nuclear Physics.

Michael Aleixo dos Santos

COMPACT STARS PROPERTIES FROM A D3/D7 HOLOGRAPHIC MODEL

Thesis approved in its final version by signatories below:

Prof. Dr. Wayne Leonardo Silva de Paula

Advisor

Prof. Dr. José Abdalla Helayël-Neto

Co-advisor

Campo Montenegro
São José dos Campos, SP - Brazil
2025

Cataloging-in Publication Data
Documentation and Information Division

Santos, Michael Aleixo dos
COMPACT STARS PROPERTIES FROM A D3/D7 HOLOGRAPHIC MODEL / Michael Aleixo dos Santos.
São José dos Campos, 2025.
205f.

Thesis of Doctor of Science – Course of Physics. Area of Nuclear Physics – Instituto Tecnológico de Aeronáutica, 2025. Advisor: Prof. Dr. Wayne Leonardo Silva de Paula. Co-advisor: Prof. Dr. José Abdalla Helayël-Neto.

1. Modelos holográficos. 2. Estrelas híbridas. 3. Objetos compactos. I. Instituto Tecnológico de Aeronáutica. II. Title.

BIBLIOGRAPHIC REFERENCE

SANTOS, Michael Aleixo dos. **COMPACT STARS PROPERTIES FROM A D3/D7 HOLOGRAPHIC MODEL**. 2025. 205f. Thesis of Doctor of Science – Instituto Tecnológico de Aeronáutica, São José dos Campos.

CESSION OF RIGHTS

Michael Aleixo dos Santos
Departamento de Física | Instituto Tecnológico de Aeronáutica (ITA)
Praça Mal. Eduardo Gomes, 50. – CEP 12228-900 | São José dos Campos – SP

COMPACT STARS PROPERTIES FROM A D3/D7 HOLOGRAPHIC MODEL

Michael Aleixo dos Santos

Thesis Committee Composition:

Prof. Dr.	Brett Vern Carlson	Presidente	-	ITA
Prof. Dr.	Wayne Leonardo Silva de Paula	Advisor	-	ITA
Prof. Dr.	José Abdalla Helayël-Neto	Co-advisor	-	CBPF
Prof. Dr.	Carlos Alfonso Martin Ballon Bayona		-	UFRJ
Prof. Dr.	José Domingo Arbañil Vela		-	UPN
Profa. Dra.	Laura Paulucci Marinho		-	ITA

ITA

Acknowledgments

Thank God for my life.

To my beloved mother Conceição Aparecida, father, stepfather and grandmother who rest in peace eternally. To my family: Michelli A., Willian A., M^a do Carmo. To my wife Laís Imbelloni for all these years with love and affection. To friendly families: Imbelloni and Borges. To all my dearest friends who helped me unconditionally. To my advisor Dr. Wayne de Paula and my co-advisor Dr. José Helayel for the opportunity. To my all professors mainly the ones from ITA who helped me intensely. To Dr. César Lenzi for all the contribution with the paper.

To CNPq for financial support.

TO UERJ for being my second home during my undergraduate and master's studies.

To ITA and CBPF for the new horizons.

And to all those who directly or indirectly allowed this to happen.

Thank you very much.

"*And never forget, my son: time will pass all the same.*"

"*E nunca se esqueça, meu filho: o tempo passará da mesma forma.*"

Obrigado, mãe. Consegui. Um dia nos encontraremos.

Resumo

O comportamento da matéria nuclear em densidades extremas permanece como uma das fronteiras mais desafiadoras da astrofísica moderna. Este trabalho investiga, sob a ótica da correspondência holográfica AdS/CFT, configurações estelares compostas por matéria de quarks utilizando um modelo top-down baseado na configuração de branas D3-D7, no qual não há distinção entre os sabores dos quarks considerados. As classes de objetos compactos analisadas abrangem tanto estrelas de quarks puras quanto estrelas híbridas com núcleo de quarks, incorporando efeitos de estabilidade dinâmica e comparações com observações astrofísicas recentes.

Para as estrelas de quarks puras, obtém-se a equação de estado a partir do modelo holográfico, tendo como parâmetro livre a massa constituinte do quark. A análise revela que, embora essas configurações estáveis atinjam massas elevadas e estejam de acordo com parte dos dados observacionais, elas não conseguem simultaneamente satisfazer as restrições de deformabilidade de maré impostas pelo evento GW170817.

Como segunda aplicação do modelo holográfico, o foco recai sobre estrelas híbridas compostas por uma crosta hadrônica, descrita pela parametrização NL3* do modelo relativístico de campo médio, e um núcleo de quarks desconfinados modelado pela configuração D3/D7. Considerando transições de fase lentas e de primeira ordem, sob a

prescrição de Maxwell, conduz-se uma análise de estabilidade baseada em oscilações radiais, a qual evidencia a existência de soluções estáveis com núcleo de quarks. Essas configurações alcançam massas máximas próximas a 2,7 massas solares. Entre os resultados mais relevantes, destacam-se a compatibilidade com relações massa-raio observacionais, a manutenção da causalidade e a estimativa do tamanho do núcleo de quarks.

Abstract

The behavior of nuclear matter at extreme densities remains one of the most compelling frontiers in modern astrophysics. This work investigates compact star configurations composed of quark matter within the framework of the AdS/CFT holographic correspondence, employing a flavor-independent top-down D3/D7 holographic model. The study focuses on two types of compact objects: pure quark stars and hybrid stars with quark cores, incorporating dynamical stability criteria and comparisons with recent observational constraints.

In the case of pure quark stars, the equation of state is derived from the holographic model, with the constituent quark mass treated as a free parameter. While the resulting stable configurations reach high masses consistent with some observational bounds, they fail to simultaneously satisfy the tidal deformability limits inferred from the GW170817 event.

As a second application, we investigate hybrid stars composed of a hadronic crust — described by the NL3* parameterization of the relativistic mean-field model — and a deconfined quark core governed by the same flavor-independent holographic model. Assuming slow, first-order phase transitions and adopting the Maxwell construction, we perform a dynamical stability analysis based on radial oscillations. The results reveal sta-

ble hybrid star configurations with quark cores, reaching maximum masses near 2.7 solar masses. Among the most significant outcomes are the compatibility with observational mass-radius relations, the preservation of causality, and the estimation of quark core sizes.

List of Figures

List of Abbreviations and Acronyms

HHS	Holographic Hybrid Star
AdS	Anti de-Sitter
CFT	Conformal Field Theory
QCD	Quantum Chromodynamics
EOS	Equations of State
TOV	Tolman-Oppenheimer-Volkoff
EMD	Einstein-Maxwell-Dilaton
IR	infrared
UV	ultraviolet
QGP	quark-gluon-plasma
LT	Legendre transform
SUGRA	Supergravity
SYM	Super Yang – Mills
GW	gravitational waves

Contents

1 Introduction

Building a theory that can describe the simultaneous interactions between all the four forces of Nature has been an unsolved problem. Although we do have the Standard Model that unifies the electromagnetic, weak and strong nuclear forces, we do not have so far, a generalized theory including also the gravitational force. So far, we have not yet understood how to make the quantum framework accommodate the gravitational one. As a result, the construction of a "quantum theory of gravity" remains an open and ongoing endeavor.

The Quantum Chromodynamics (QCD), which is the quantum field theory for the strong nuclear force between quarks and gluons, has many particularities. When we move towards to the infrared (IR) regime, the behavior of the theory is completely different if we compare to the ultraviolet (UV) one. This behavior reflects the fact that QCD is a theory with a characteristic energy scale. This natural scale is close to 300 MeV.

At high energy, that is, at the UV regime, QCD experiences the asymptotic freedom and physically it represents the appearance of the quark-gluon-plasma (QGP): a plasma state where quarks and gluons are free and mixed, without any bound states. On the other hand, at low energy, at the IR regime, the opposite happens. Quarks and gluons experience the *hadronization* process composing hadrons: bound states of quarks such as

protons and neutrons.

The hadronization guarantees that quarks cannot be found isolated or free in low energy and instead they are always confined. That is the confinement phenomenon and this statement is one of the most important features of the theory. If one varies, for example, the energy from the high (low) energy to low (high) energy, at some specific point the system will undergo a phase transition, in which the system shifts from a deconfined (free) phase to a confined (bounded) phase. That is the region where the QGP transforms into hadrons and vice-versa.

The difficulty of dealing with QCD at low energy comes from the multiple infinities that appear when you try to solve the problem in a perturbative way (the standard procedure at high energy). To bypass this problem, many attempts were developed and one of them is the lattice QCD, whose model is built from a discretized gauge theory where the spacetime corresponds to the infinite 4D grid.

On the other hand, in 1997 Maldacena presented on his article the correspondence between a type-IIB 10D string theory with the 4-dimensional $\mathcal{N} = 4$ Super Yang-Mills gauge theory. This idea might help to address the problem, as it provides a way to understand the strongly coupled quantum side of the duality through its weakly coupled gravitational side. This is the key advantage of gauge/gravity duality: it allows one to study a strongly coupled theory using a weakly coupled one.

Although this correspondence was not fully proved, if it really exists, the gauge part of the duality could be represented by QCD. That is the core of this investigation. This way of understanding the gauge theory by studying the gravitational part is called holography.

There are two ways to approach this situation, trying to construct a gravitational

theory that allows us to better understand the theory which mimics QCD: top down and bottom up. The first one starts from the 10D string theory to construct the model and the second one starts by considering the phenomenological features from a 5D theory.

For the Top Down case, we will present the model for brane intersections, the Dp-Dq system. And after constructing this generalized model, we will apply to the D3-D7 case. There is an ongoing work for the Bottom Up case. We want to present, in the future, this original model constructed from a deformation of the metric after adding a black hole-like structure to get the temperature concept and the chemical potential.

All of these models are important to investigate compact stars, that is, neutron stars, white dwarf, hybrid stars and quark stars. In this thesis we will focus on compact stars, in particular quark stars — composed entirely of deconfined quark matter — and hybrid stars, which contain a quark matter core surrounded by a hadronic crust.

In Chapter (2) we will discuss important concepts to better understand the description of the holographic models. We will start with the 't Hooft work (HOOFT, 1993) in which he uses the previous concept of the black hole entropy proposed by Hawking (HAWKING, 1976) and Bekenstein (BEKENSTEIN, 1973). We introduced the 't Hooft idea to promote the expansion $1/N$ to bypass the QCD non-perturbative regime. Later we discuss about the need to map all the symmetries present in the AdS/CFT conjecture context and we do it discussing about isometries, killing vectors and also the conformal transformations. We finish this second chapter after discussing some QCD features and two kinds of holographic models.

In Chapter (3), we began with a brief introduction to the structure of neutron stars. Given that the composition of a hybrid star assumes the existence of a phase transition region, we presented the Maxwell and Gibbs constructions as two possible frameworks

commonly used in this type of study (CONSTANTINOU *et al.*, 2023). We emphasized that our approach adopts the Maxwell construction, which assumes a sharp, first-order phase transition. We introduced the mass-radius relation and its numerical derivation, followed by a discussion of the stability criteria employed in our analysis—both for quark stars and hybrid stars. The chapter concludes by introducing tidal deformability as a key observable derived from binary systems, whose results will be presented specifically for the case of quark stars.

In Chapter (4) we will have a detailed discussion of the construction for a Dp-Dq brane system of a Top Down holographic model. We will start by brane configuration in the 10D space and after that we will construct the components of the Dirac-Born-Infeld (DBI) action. That action must be regulated on-shell and after this process we will recognize this outcome as the free energy. We will use (KARCH; O'BANNON, 2007) and (ITSIOS *et al.*, 2016) as guides. We will apply the model to D3-D7 system. There, we will use (HOYOS *et al.*, 2016) as a guide to setting all the parameters. We will get an expression for the pressure by using thermodynamic relations. We will use the equation of states to get the Tolman-Oppenheimer-Volkoff (TOV) equations. We will see that this equation of state has a free mass parameter, which will be used in the study of both quark stars and hybrid stars.

Chapter (5) is dedicated to the study of quark stars, which led to the development of the first original research work (ALEIXO *et al.*, 2024). In this chapter, we apply the D3/D7 holographic model to investigate the properties of this class of compact objects. The constituent quark mass parameter, denoted by m, is treated as a free parameter in this flavor-independent model. We present and analyze the results obtained from this study, which include the mass–radius diagram and the tidal deformability for binary star

systems.

Chapter (6) is dedicated to the study of hybrid stars and forms the basis for the second original research work of this thesis (ALEIXO *et al.*, 2025). In this chapter, we apply the D3/D7 holographic model—previously used for quark stars—to describe the quark phase, while the hadronic phase is modeled using the relativistic mean-field model NL3* (LALAZISSIS *et al.*, 2009). The equation of state is constructed via the Maxwell construction, assuming a sharp first-order phase transition. We investigate various physical properties of hybrid stars, including the mass–radius relation, phase transition behavior, and pressure and energy-density profiles, considering the slow phase transitions (LUGONES *et al.*, 2023). Additionally, we analyze the impact of the constituent quark mass on the structure and stability of the stars, as well as on the size of the quark core.

2 The AdS/CFT correspondence

When Maldacena presented in his article the AdS/CFT duality, he was proposing an exact map between type IIB superstring theory defined in 10 dimensions and $\mathcal{N} = 4$ supersymmetric Yang-Mills theory defined in 4-dimensional Minkowski spacetime (MALDACENA, 1998).

The ten-dimensional spacetime can be splitted into two different spaces. The first is a five-dimensional anti-de Sitter space, denoted AdS_5, which captures the spacetime symmetries of the gauge theory and will be further discussed in subsection (2.4.4.1). The second is a five-dimensional sphere, S^5, often referred to as the internal or compact space, which is associated with the R-symmetry group of the dual $\mathcal{N} = 4$ SYM theory.

The fact that the gauge theory exists in four dimensions while the string theory is defined in ten dimensions is a striking realization of the holographic principle. More precisely, the boundary of the AdS_5 spacetime — where the conformal field theory resides — is four-dimensional, and the extra five dimensions of S^5 encode internal symmetries. Thus, the duality manifests as a correspondence between a higher-dimensional gravitational theory in the bulk and a lower-dimensional non-gravitational quantum field theory on the boundary.

That is, the process is about to connect the gravitational side of the conjecture

(represented by the AdS) with a Conformal Field Theory (CFT) that is defined at the boundary (with one less dimension). A significant advantage emerges from this correspondence: the possibility of studying a field theory in a strongly coupled regime, where perturbation theory methods are not applicable. By assuming that the duality predicted by the correspondence holds, one can investigate the strong coupling regime through mapping to another theory that lies in a weakly coupled regime.

To reach the duality, both theories must have the conformal invariance that, as we will discuss in section (2.4.2), contains the invariance by rescaling.

At low energy, the type-IIB string theory becomes a supergravity theory (SUGRA). From this point, the string action becomes a classical action and the equivalence can be done

$$Z_{SUGRA}\left[\phi_0(\vec{x})\right] = e^{-I_S[\phi(\vec{x},z)]|_{\phi(\vec{x},0)=\phi_0(\vec{x})}} = < e^{\int d^4x\, \phi_0(\vec{x})\, \mathcal{O}(\vec{x})} >, \tag{2.1}$$

I_S being the classical action with the field $\phi(\vec{x}, z)$ living in a 5-dimensional space (bulk) whereas the field $\phi_0(\vec{x})$ is defined at the boundary, i.e., in a 4-dimensional space, $\mathcal{O}\ (\vec{x})$ is a CFT operator living at the boundary, which is the core of this mapping process. It is responsible for connecting certain information from the bulk to the corresponding correlator that is defined at the boundary.

If we suppose this duality exists, one can try to replace "CFT" by "QCD". The Quantum Chromodynamics is a gauge theory for the strong force. QCD has a natural scale close to 300 MeV, which means that this theory has different behaviors if we compare, for example, the IR part with the UV one. At high energy, where the assymptotic freedom is established and quarks/gluons become free, one can recognize QCD as a conformal theory, but at low energy, QCD breaks the conformal invariance.

There are two main frameworks for employing the AdS/CFT correspondence to investigate properties of Quantum Chromodynamics (QCD). The first is the top-down approach, in which one starts from a complete string theory setup and seeks to identify a dual gravitational background that captures key features of QCD. The second is the bottom-up approach. In this framework, one constructs an effective five-dimensional gravitational theory based on phenomenological inputs from QCD, aiming to reproduce its nonperturbative dynamics.

A fundamental difficulty shared by both approaches arises from the fact that QCD is not a conformal theory, particularly at low energies. Since the original AdS/CFT correspondence connects a conformal field theory to a gravitational dual in Anti-de Sitter space, applying this correspondence to QCD requires breaking conformal symmetry on the gravitational side. This symmetry breaking is a crucial step in building realistic models, and several constructions have been proposed within the "AdS/QCD framework" to implement this feature phenomenologically (BALLON-BAYONA *et al.*, 2023) (PAULA *et al.*, 2020) (PAULA; FREDERICO, 2010) (KARAPETYAN *et al.*, 2023).

Several models were built within this perspective such as the Hard Wall, the Soft Wall and the Dynamical Soft Wall. We will present these models in the section (2.5). These models have a Bottom Up approach, that is, all the model is constructed from a 5d phenomenological point of view. But there are the Top Down ones that are constructed by using a 10d string theory. One of them is called D3-D7 model and it will be our focus on this current work. This model will be presented in details in the Chapter (4).

In this section we will present brief comments on some steps that will allow a better understanding of the AdS/CFT conjecture. We will see from the first idea of holography how to connect a quantum gauge theory with a gravitational theory like string theory.

2.1 Some aspects of the duality

In this section, we will present some aspects related to the context of duality and motivate how extra dimensions can be interpreted from the perspective of the AdS/CFT correspondence.

2.1.1 Interpretation of extra dimensions

Gerard 't Hooft was the first who postulated the holographic principle (HOOFT, 1993). That principle tells us that inside a quantum theory with gravity (what happens for string theory) all the information contained in the bulk (*n-dimensional*) can be mapped on a corresponding boundary ($n-1$- *dimensional*). Many works about the holographic principle and its applications were made after this starting point (SUSSKIND, 1995) (CORLEY; JACOBSON, 1996) (HOOFT, 1997) (BOSCHI-FILHO; BRAGA, 2001) (SUSSKIND; WITTEN, 1998) (HOOFT, 2001) (THORN, 1991).

This principle was inspired by the studies of Hawking (HAWKING, 1976) and Bekenstein (BEKENSTEIN, 1973) about the black hole entropy. It was conjectured that the entropy S of a black hole with radius R was related to R^2 instead of the volume (third power), as might be expected. Therefore, all information that has fallen into the black hole (the bulk region) might be encoded in the event horizon. Since a black hole is a three-dimensional object, the boundary is a surface defined in two dimensions. For this reason, one can say that the entropy of a black hole is proportional to the area of its event horizon in Planck units: $S_{BH} \sim A_{surface}$.

The idea of establishing a correspondence between a physical theory defined in an n-dimensional spacetime and another living in $(n-1)$ dimensions — where the lower-

dimensional theory fully encodes the dynamics of the higher-dimensional one — is known as *holography*, reflecting the notion that all information of a higher-dimensional system can be stored on its boundary.

This principle suggests that the degrees of freedom of a quantum gravity theory in a volume V_{d+1} in $(d+1)$ dimensions are formulated in terms of the degrees of freedom of a theory defined on the boundary of this volume, that is, $\partial V_{d+1} = A_d$, where A_d is the surface that bounds the bulk volume V_{d+1}.

There is another interpretation that originates from the Wilson-Kadanoff Renormalization Group approach in an analysis performed on a lattice.

Consider the explanation provided in (RAMALLO, 2015) regarding a non-gravitational system on a lattice with spacing a. The corresponding Hamiltonian is

$$H = \sum_{x,i} J_i(x,a)\, \mathcal{O}^i(x), \tag{2.2}$$

where x represents the different positions on the lattice, and i is the index for the different operators $\mathcal{O}^i$. The terms $J_i(x,a)$ represent the sources (or coupling constants) of the operators at a given position x on the lattice. Note the dependence of J_i on the lattice spacing a. In the renormalization group approach, we increase the lattice spacing and replace multiple sites with a single one that represents the average of the lattice variables. In this process, the form of the Hamiltonian remains unchanged; however, different operators will acquire different weights, as increasing the lattice spacing a ensures that the sources also change.

To make this approach clearer, one can consider increasing the spacing by doubling

its values, that is,

$$J_i(x,a) \to J_i(x,2a) \to J_i(x,4a) \to \ \ldots, \tag{2.3}$$

which can be rewritten as $J_i(x,u)$, where $u = (a,\ 2a,\ 4a, \ldots)$ represents the length scale used to study the system.

The way these couplings evolve with the scale is determined by a flow equation called the Renormalization Group Equation, which has the form (SCHWARTZ, 2014).

$$u\ \frac{\partial J_i(x,u)}{\partial u} = \frac{\partial J_i(x,u)}{\partial(\ln u)} = \beta_i\ (J_j(x,u),u), \tag{2.4}$$

where β_i is known as the β-function of the i-th coupling constant and can be obtained through perturbation theory in the weak coupling regime. It is important to emphasize that this function is local with respect to the scale u used. Therefore, one can interpret the role of this scale as an extra spacetime coordinate, meaning an additional dimension, since the physics is considered local with respect to this scale parameter.

This beta function is extremely important in defining the nature of the theory concerning conformality. Anticipating: if the beta function is positive, one can conclude that the coupling constant diverges with the renormalization scale parameter. In this case, we say that there is a Landau pole at an energy scale Λ, which is characterized by $J_i(u) \to \infty$ as $u \to \Lambda$. However, if it is negative, the relation promotes a convergent behavior.

Moreover, when it is zero, this indicates that the coupling constant does not vary with the renormalization scale. From an energy scale perspective, a vanishing beta function ensures that we are dealing with a scale-invariant theory, meaning a theory that possesses

a conformal character.

Since the sources can be interpreted as fields in this extra-dimensional space, they can be rewritten in the form

$$J_i(x,u) = \phi_i(x,u). \tag{2.5}$$

In the context of the AdS/CFT duality, the sources (couplings) of the field theory (CFT) in the ultraviolet (UV), that is, at short distances, are identified as fields $\phi(x,u)$ evaluated at the boundary of this extra-dimensional space. Through this, one can consider that the CFT resides at the boundary of this higher-dimensional space.

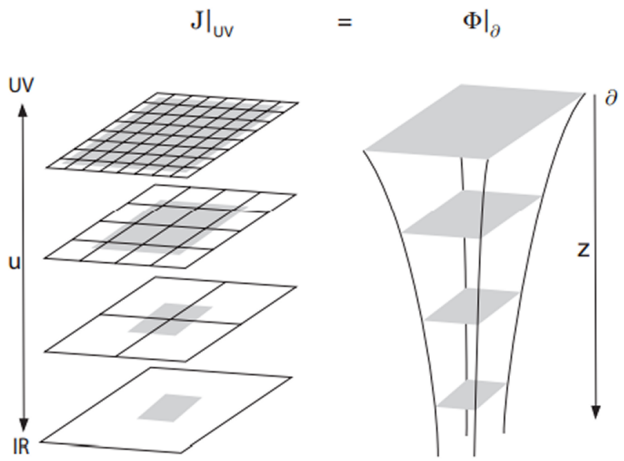

FIGURE 2.1 – On the left, we depict the Kadanoff-Wilson renormalization process for a lattice system. In the AdS/CFT correspondence, lattices at different scales are interpreted as layers of the higher-dimensional space, as shown on the right side of the figure. Figure extracted from (RAMALLO, 2015).

Illustration (2.1) demonstrates the Wilson-Kadanoff method on a lattice and shows the existing equivalence between u and z, the coordinate of the extra dimension. The AdS/CFT Correspondence itself is often regarded as the geometrization of the quantum dynamics encoded by the Renormalization Group.

2.1.2 The 't Hooft limit

With the article (HOOFT, 1974), 't Hooft proposed a relation between the SU(N) gauge theories and string theories. But this relation just happens in the case when N [1] is large.

That is one attempt to solve the issue about the strong coupling that happens in QCD. At low energy, quarks and gluons are bounded together establishing the confinement regime. QCD is a gauge theory defined by the group SU(3), where "3" means 3 charges called by colors.

One can imagine that considering a model with an infinite number of color/charge could be more complex, but it is not true.

Because the interaction is strong at low energy, the QCD coupling constant g diverges and any attempt of applying the regular perturbative methods fails incredibly by countless infinites that appear. Therefore 't Hooft suggested the expansion $1/N$ instead of N or g, and with a large N, one could apply perturbative methods. The expansion is performed using the 't Hooft coupling constant, defined as $\lambda = g^2 N$. The 't Hooft limit is formally defined by taking $N \to \infty$ while keeping $g \to 0$ in such a way that λ remains fixed.

The result of this approach comes when 't Hooft realized that the dominant Feymann diagrams are the planar ones, which are present in a perturbative expansion of a free string theory. For this reason, he proposed this duality between SU(N) gauge theory and string theory in the large-N limit.

To verify this conclusion, one can start from the so-called double-line representation, in which 't Hooft proposes that the rule for drawing Feynman diagrams should be based on illustrating one line for each index, rather than the usual approach of drawing one line

[1] Actually this N is frequently named by N_c. This label is just a reminder that this is about the number of colors.

for each virtual particle. In this way, for example, we can check from figure 2.2 that the gluon propagator will have a double line, while the quark propagator will be represented by a single line.

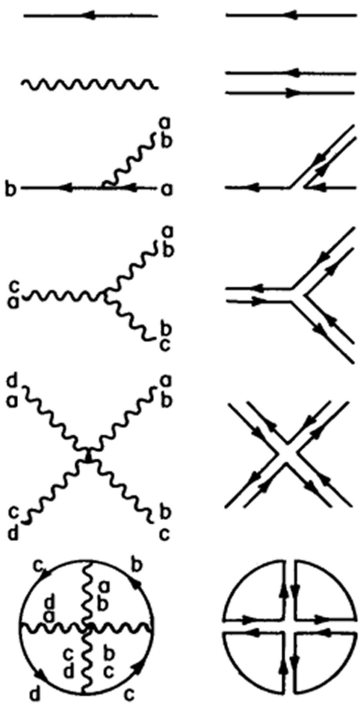

FIGURE 2.2 – Single-line and Double-line representation to Feynman diagrams. Extracted from (COLEMAN, 1988).

Considering, for simplicity, a pure Yang-Mills theory without matter fields such as quarks or scalars, the Lagrangian of this non-Abelian gauge theory can be written as

$$\mathcal{L} = -\frac{1}{g_{YM}^2}\, tr[F^{\mu\nu}\, F_{\mu\nu}], \tag{2.6}$$

where $F_{\mu\nu}$ is defined as

$$F_{\mu\nu} = \partial_\mu A_\nu - \partial_\nu A_\mu - ig\, [A_\mu, A_\nu]. \tag{2.7}$$

Here, the non-Abelian gauge field A_μ is in the adjoint representation of the SU(N)

group, and for this reason, it takes the form in the Lie algebra of the group, represented as

$$A_\mu \equiv A_\mu^a \, T^a \quad ; \quad a = 1, \ldots, N^2 - 1, \tag{2.8}$$

where T^a are the generators of the Lie algebra of SU(N). The term $N^2 - 1$ represents the number of generators that define the dimension of the vector space of the matrices in the SU(N) group, as seen with 3 generators in SU(2) and 8 generators in SU(3). Such group generators satisfy the Lie algebra defined by

$$[T^a, T^b] = i f^{abc} \, T^c, \tag{2.9}$$

where f^{abc} are the structure constants of the SU(N) group. Such structure constants of the group define the internal symmetry.

As mentioned earlier, the constant known as the 't Hooft coupling, $\lambda = g_{\mathrm{YM}}^2 N$, can help us rewrite the Lagrangian in the form

$$\mathcal{L} = -\frac{N}{\lambda} \, tr[F^{\mu\nu} \, F_{\mu\nu}]. \tag{2.10}$$

The 't Hooft limit is established when we consider the limiting case $N \to \infty$ in this expression, which would lead to a divergent behavior in the previous equation for this classical limit. However, the analysis of this divergence changes when we realize that the global behavior of the theory can remain controlled. This is because, to ensure that the 't Hooft coupling constant remains finite and constant, the gauge coupling g_{YM} must be very small. In the limiting case $N \to \infty$, this requires $g_{\mathrm{YM}} \to 0$.

There is an additional consequence elucidated by 't Hooft that represents the main focus of our discussion. He discovered that only planar Feynman diagrams contribute within this limit. To understand how this occurs, we need to identify the contributions that arise from the structure of these diagrams.

A Feynman diagram can be classified according to its powers of g and N. A generic diagram is composed of propagators, loops, and interaction vertices. Each of these structures contributes with factors related to the power of g_{YM}.

If we were to explicitly compute the square of the field strength tensor $F_{\mu\nu}$ in the Lagrangian, we would see that the possible interaction vertices are represented by the cubic and quartic terms in the gauge field. The cubic terms are associated with g_{YM}, while the quartic terms are proportional to g_{YM}^2, meaning they appear - the vertices - as powers of g_{YM}. By using the definition of the 't Hooft coupling constant, we can conclude that the vertices are proportional to the factor N/λ, since the Lagrangian explicitly contains the term $1/g_{\mathrm{YM}}^2$.

The same procedure can be applied to obtain the expression for the propagator of the gauge field A_μ^a. This propagator arises from the quadratic term of A_μ^a in F^2 in the Lagrangian. By carrying out this procedure, it is found that the final expression for the propagator is proportional to g_{YM}, which allows us to conclude that each propagator contributes with a factor proportional to λ/N.

Finally, we can analyze the contribution of closed lines, that is, the loops present in the diagrams. The calculation is performed by summing over the gauge group indices, which results in a contribution to the Feynman diagrams of the form $\delta_i^i = N$. Generalizing, for a generic diagram with multiple loops, the contribution will be given as powers of N.

In summary, each diagram contributes with

each propagator	λ/N
each vertex	N/λ
each closed loop	N

Thus, the total contribution of a generic diagram is determined by counting the number of propagators, vertices, and loops, resulting in an overall dependence on powers of N.

Therefore, we can combine these contributions into a single expression for each diagram

$$Diagram = \left(\frac{\lambda}{N}\right)^{\#\text{Propagators} - \#\text{Vertices}} N^{\#\text{Closed lines}} . \tag{2.11}$$

An interesting perspective arises when we reinterpret Feynman diagrams in terms of a bidimensional structure. By adopting 't Hooft's double-line notation, each gauge field propagator is represented by two lines corresponding to color indices, while quark propagators remain as single lines. This visualization naturally suggests that closed loops in Feynman diagrams can be viewed as the faces of a discretized surface.

Therefore, one can imagine such a surface having a number F of faces, which we already know is directly related to the number of loops (closed lines). The same applies to internal lines, representing propagators, which can be denoted by a quantity P present in the diagram. Finally, we can also consider the existence of V vertices, which are the points where interactions occur.

These three quantities define what is known as the Euler characteristic, whose defini-

tion is given by (NAKAHARA, 2003)

$$\chi = V - P + F. \tag{2.12}$$

This number is considered a topological invariant because it remains unchanged under continuous deformations of the surface. In other words, χ does not depend on the specific shape of the diagram but only on its fundamental topological structure. This property allows us to classify different surfaces and relate Feynman diagram expansions in gauge theories to topological properties of two-dimensional manifolds.

Rewriting equation (2.11), using $\tilde{D}$ to represent the diagram, we obtain

$$\tilde{D} = \left(\frac{\lambda}{N}\right)^{\mathrm{P}\,-\,\mathrm{V}} N^{\mathrm{F}} \;=\; N^{\chi}\,\lambda^{\mathrm{P}\,-\,\mathrm{V}}\,. \tag{2.13}$$

The topological invariant can be rewritten in terms of the number of holes (or handles) (H) [2] in the considered surface and, for this reason, is always a positive quantity. It is related by the expression (NAKAHARA, 2003)

$$\chi = 2 - 2H. \tag{2.14}$$

A surface without handles, defined by $H = 0$, has $\chi = 2$ and represents a sphere. However, a surface with $H = 1$ has $\chi = 0$ and can be represented by a torus, which has a single handle.

Using expression (2.14), which represents Euler's theorem, each diagram can be rewrit-

[2] H is sometimes represented by "g" and is known as the surface genus.

ten in the form

$$\tilde{D} = N^{(2\,-\,2\mathrm{H})}\,\lambda^{\mathrm{P}\,-\,\mathrm{V}}\,. \tag{2.15}$$

Through the previous expression, we can conclude the effect of the classical 't Hooft limit, which by definition considers that the 't Hooft coupling $\lambda = g^2 N$ is kept fixed while taking $N \to \infty$ and $g \to 0$.

In this limit, the expansion is dominated by surfaces with the smallest number of holes (or handles), meaning surfaces that are topologically equivalent to the sphere (or the plane with a point at infinity). These surfaces are called planar, and from the previous equation, it is evident that they contribute with a factor of N^2 in the perturbative expansion of the diagrams.

It is interesting to highlight that surfaces with handles are called non-planar. These surfaces contribute with a factor of N^{-2n}, where $n = 0, 1, \ldots$. Therefore, all contributions from these surfaces are suppressed in the perturbative expansion, ensuring a significant simplification within this limit, known as the Large-N expansion.

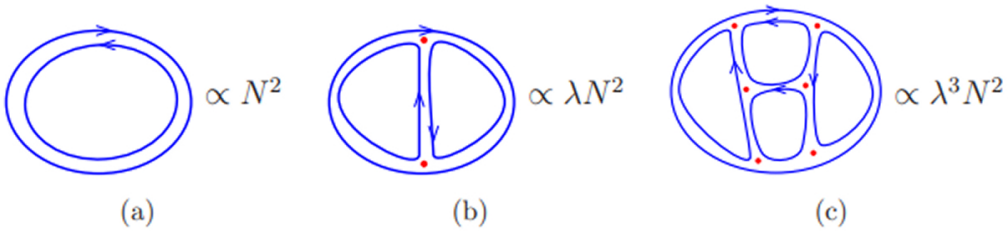

FIGURE 2.3 – Planar diagrams. Extracted from (MCGREEVY, 2010).

Figure 2.3 presents three examples of planar diagrams. The contribution of all these diagrams is proportional to N^2, differing only by powers of the 't Hooft coupling constant, justified by the difference between the number of propagators and the number of vertices.


$\propto g^2 N = \lambda N^0$

FIGURE 2.4 – Non-planar diagrams. Extracted from (MCGREEVY, 2010).

In Figure 2.4, we have an example of a non-planar diagram with a single handle ($H = 1$), making its contribution proportional to $N^0\lambda$, since it contains three propagators and only two vertices.

Through these examples, it becomes evident that equation (2.15) for the amplitude ($\tilde{D}$) describing the perturbative expansion of a diagram can be expressed as a power series expansion in the form

$$\tilde{D} \;=\; \sum_{H=0}^{\infty} N^{2-2H} f_H(\lambda), \tag{2.16}$$

where $f_H(\lambda)$ is a polynomial in λ.

For surfaces that are considered planar, the explicit form of this expression is

$$N^2 \sum_{k=0}^{\infty} c_k \lambda^k \;=\; N^2 \left(c_0 + c_1\lambda + c_2\lambda^2 + c_3\lambda^3 + ...\right) \;=\; N^2\, f(\lambda), \tag{2.17}$$

where c_k are numerical coefficients that depend on the detailed computation of each Feynman diagram.

From the partition function perspective, the expression becomes

$$Log\ Z = \sum_{H=0}^{\infty} N^{2-2H}\ f_H(\lambda), \tag{2.18}$$

and now we know that, by considering the 't Hooft limit in the previous expression, only the planar diagrams will contribute.

Moreover, it is possible to conclude that, within this Large-N limit, string theory is weakly coupled. In the 't Hooft limit, an SU(N) field theory is dual to a string theory, establishing a deep connection between the two frameworks.

This dual relationship between the two theories can become more explicit through the perturbative expansion of a closed string theory, which expresses its physical quantities in terms of the propagation of a string through spacetime.

When we consider that a closed string, as it propagates, creates a worldsheet represented by a compact two-dimensional surface, we can interpret the perturbative expansion as one associated with the topology of the generated bidimensional surfaces.

In a completely analogous way, these strings can interact at vertices, leading to splitting or joining processes. Depending on the configuration, the generated surfaces may develop handles, similar to the representations we previously discussed in the context of field theory.

On the other hand, the perturbative expansion of a closed string theory takes the following form (CASALDERREY-SOLANA *et al.*, 2014)

$$Log\ Z_{\text{string}} = \sum_{H=0}^{\infty} g_s^{2H-2}\ f_H(\alpha'), \tag{2.19}$$

where g_s is the string coupling constant, and $f_H(\alpha')$ represents the contribution from worldsheet topologies of genus H, with α' defined as $\alpha' = \frac{1}{T}$, where T represents the string tension (energy per unit length). This parameter characterizes the intrinsic length scale of the string theory, with the fundamental string length given by $l_s = \sqrt{\alpha'}$.

By identifying the string coupling constant g_s with $1/N$, we observe that the expression (2.18) becomes identical to (2.19). Therefore, these two formulations provide strong evidence that gauge theories and string theory are related in some fundamental way.

2.1.3 Why AdS?

As we will see in the following discussions, it is possible to assume that a field theory in a d-dimensional space can be described by a gravity theory or even a string theory in a $(d+1)$-dimensional space. This is the fundamental principle of holographic models, as we will discuss.

If we were to consider the most general metric description of a d-dimensional space using Poincaré symmetry, we would obtain

$$ds^2 = \Omega^2(z)\ (-dt^2 + d\vec{x}^2 + dz^2), \tag{2.20}$$

where z represents the extra spatial dimension coordinate. The dependence on z only in function $\Omega(z)$ ensures invariance under translation transformations in the other dimensions $(t, \vec{x})$.

If we are interested in investigating field theories that are conformal, meaning they exhibit invariance under scale transformations (we will discuss this aspect in more detail in Section (2.4.2)), the functional form of $\Omega(z)$ can be determined through the constraint imposed by this consideration. A theory that is said to be conformally invariant becomes truly invariant under the following scaling transformation

$$(t, \vec{x}) \to C\ (t, \vec{x}), \tag{2.21}$$

where C is a constant. To keep the metric (2.20) invariant under the previously proposed scale transformation, an additional transformation in the coordinate z must be considered such that $z \to C\ z$. Algebraically, it can be verified that invariance is established if the function $\Omega(z)$ undergoes the following simultaneous transformation

$$\Omega(z) \to C^{-1}\ \Omega(z). \tag{2.22}$$

Thus, considering all these simultaneous transformations, the form of the metric, and the requirement that the function Ω must be dimensionless, the form that ensures invariance is

$$\Omega(z) = \frac{R}{z}, \tag{2.23}$$

where R here is a constant with spatial dimension. The form of the function $\Omega(z)$ previously presented can thus be used to update the expression for the metric (2.20)

$$ds^2 = \frac{R^2}{z^2}\ (-dt^2 + d\vec{x}^2 + dz^2), \tag{2.24}$$

It is possible to see that this is precisely the line element that describes the Anti-de Sitter space in $(d+1)$ dimensions, AdS_{d+1}.

2.2 String theory essentials

In this section, we will discuss essential aspects of string theory concerning the AdS/CFT Correspondence. The discussion will cover possible string configurations, the represen-

tation of D-branes, and the interpretations that can be made when aiming to construct a holographic model, such as the D3/D7 model, which we will explore in the following chapters.

2.2.1 Some string theory concepts

String theory can be viewed as a quantum theory of relativistic one-dimensional objects, known as strings. Two fundamental parameters characterize the theory: g_s, a dimensionless coupling constant that controls the interaction strength between strings; and T_s, the string tension, analogous to the tension in classical strings.

The string tension is defined in terms of the fundamental string length scale, l_{string}, which is commonly expressed using the Regge parameter, also known as the Regge slope. The corresponding relations are

$$T_{\text{string}} = \frac{1}{2\pi\alpha'} \quad ; \quad \alpha' \equiv l^2_{\text{string}}. \tag{2.25}$$

A particle with a given mass and spin is interpreted as a vibrational mode of the string. When string theory is formulated in a D-dimensional Minkowski spacetime, consistency conditions require that $D = 26$. This version of the theory, known as bosonic string theory, contains a finite number of massless particles and an infinite tower of massive excitations with masses on the order of $m_s \equiv l_s^{-1}$, corresponding to the harmonic vibrational modes of the string (ORTíN, 2015).

If one attempts to formulate the theory in fewer than 26 dimensions, anomalies emerge, leading to inconsistencies. These are explicitly manifested by the appearance of negative-norm states, which violate unitarity and render the theory physically unacceptable.

Incorporating supersymmetry into the framework reduces the number of required spacetime dimensions to 10. This is typically achieved through compactification and results in a theory with extended symmetry between bosons and fermions—giving rise to superstring theory.

A prominent example is Type IIB superstring theory, whose spectrum includes the graviton, a spin-2 particle responsible for mediating the gravitational force, a scalar field known as the dilaton (denoted by ϕ), antisymmetric tensor fields, and the corresponding fermionic partners required by supersymmetry.

A crucial feature of closed string theory is that the graviton arises as one of its massless modes. This provides a natural and consistent mechanism for describing gravity within a quantum framework, positioning string theory as a compelling candidate for a quantum theory of gravity.

In these perspectives, interactions can be understood in geometric terms. It is postulated that two strings can join into one, or a single string can split into two—processes that occur at a vertex whose strength is governed by the coupling constant g_s. These two interaction types correspond to different topologies in string theory, as illustrated in figure 2.5. It is worth highlighting that physical observables, such as scattering amplitudes, can be obtained by summing over all string propagations that share the same initial and final states, differing only in the number of internal processes—analogous to virtual processes in quantum field theory—of string joining and splitting. In other words, the sum runs over diagrams with distinct topologies, as illustrated in figure 2.6.

It is equally important to emphasize that the string coupling constant g_s is not merely a parameter, but rather the vacuum expectation value of the dilaton field ϕ, which can

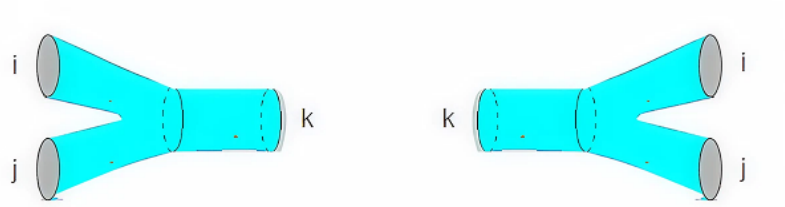

FIGURE 2.5 – Interactions in string theory. **Left**: joining process — two strings interact at a vertex to form a new string. **Right**: splitting process — one string divides into two new strings. Extracted from (CASALDERREY-SOLANA *et al.*, 2014).

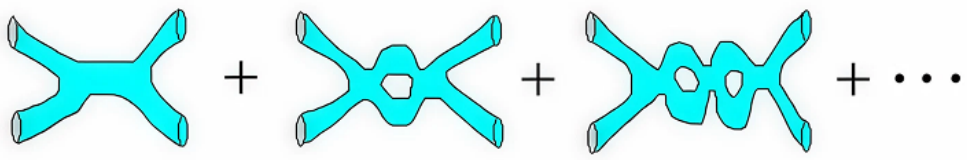

FIGURE 2.6 – 2-to-2 amplitude topologies. Handles are formed through internal splitting and joining processes. Extracted from (CASALDERREY-SOLANA *et al.*, 2014).

be expressed as (ALWIS, 1996)

$$g_s = < e^{-\phi} > \tag{2.26}$$

More precisely, it is the dilaton field that determines the strength of the interactions.

2.2.2 D-branes

There are two configurations for strings: open and closed. A closed string, whose spectrum corresponds to the dynamical fluctuations of spacetime, can propagate freely through the bulk, whereas open strings are constrained by their endpoints to a D-brane [3]. That object is where open strings can end. These open strings can describe gauge theories. From the connection between the open string and the D-brane, we can conclude that the gauge theory described by the D-brane is indeed defined on the D-brane.

[3]The "D" in the name has an important meaning. It means the Dirichlet condition which describes that the endpoints of the string lie at some constant position defined by $\delta X^\mu = 0$ at $(\sigma = 0, \pi)$, being σ the parameterization.

To better understand the configuration, we can explicitly exhibit information of dimensionality by the notation and write Dp-brane, where p always represents the number of spatial coordinates. The time component is not included on that notation and, therefore, a Dp-brane will always describe a (p+1)-dimensional gauge theory. If we want to describe a point-like general object, we can write "D0-brane". In case of representing a string-like object, it could be "D1-brane", and so on. In Type IIA superstring theory, stable Dp-branes exist only for even spatial dimensions, that is, for $p = 0, 2, 4, 6, \ldots$ In contrast, in Type IIB superstring theory [4], stable Dp-branes correspond to odd spatial dimensions, with $p = 1, 3, 5, 7, \ldots$ Remember that we want to discuss the creation of Dp-Dq brane configuration to exhibit the D3-D7 configuration, where we have a brane with 3 spatial dimensions interacting with another kind of brane with 7 spatial dimensions. We will discuss below how we can set the intersection, but here it is important to highlight that we have, for D3-D7 system, three spatial common directions. But the D7-brane has the 4 outer dimensions compactified [5] in the Calabi-Yau cone.

D-branes are therefore solitons—stable, non-perturbative solutions to the string equations of motion that minimize the energy functional—on which closed strings can collide and open, and to which open strings can attach at their endpoints. When a closed string breaks, it becomes an open string whose endpoints can then attach to D-branes.

The interaction of open string with D-branes depends on the configuration. If we have a stack of D-branes, we could have many kinds of interactions. We can consider

[4]Type IIA and IIB belong to the family of 10-dimensional closed superstring theories with $\mathcal{N} = 2$ spacetime supersymmetry, distinguished by the chirality of their spinors: IIA is non-chiral, while IIB is chiral. They are related by T-duality, which connects their spectra upon compactification of a spatial dimension. In contrast, Type I is a single, isolated theory — not a family — obtained as an orientifold projection of Type IIB. It uniquely incorporates both open and closed strings and features an $SO(32)$ gauge group, making it the only consistent theory among the five that includes open strings.

[5]To simplify this idea, one can imagine all these four dimensions compactified inside a hypersphere with a tiny radius found on each point of the space. Check a geometrical approach in (DASGUPTA *et al.*, 2025).

the configuration where the open string has its endpoints on the same brane, but we could have another possibility where one endpoint belongs to one brane and the other endpoint belongs to another different brane. Each possibility can describe a different physical reality. These possibilities are referred to as sectors (ZWIEBACH, 2009). When considering two parallel Dp-branes of the same dimensionality, four distinct sectors arise. Two involve open strings with both endpoints on either brane individually, while the other two correspond to strings stretched between the branes, with endpoints on each. String orientation plays a crucial role, as reversing it changes the sign of the associated charge. Check the figure 2.7.

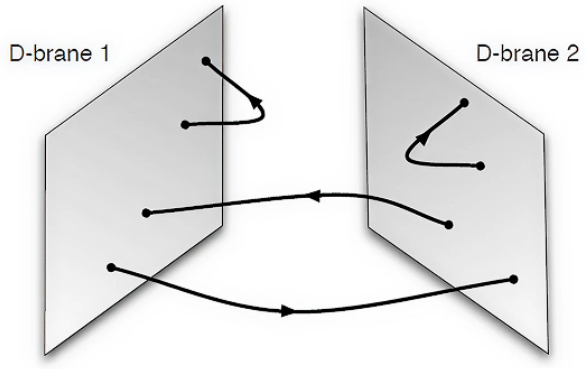

FIGURE 2.7 – Four sectors for strings between two branes. Extracted from (CASALDERREY-SOLANA *et al.*, 2014).

The mass of a Dp-brane is considered infinite due to its infinite extension along q spatial dimensions. To better understand this, one can think of a plane: mathematically, a plane is a surface that extends infinitely in two directions. Similarly, a Dp-brane spans an infinite volume in its spatial directions, which leads to both its total mass and volume being divergent.

However, despite these divergences, the ratio of mass to volume remains finite. This finite quantity is defined as the tension of the Dq-brane. The explicit expression for this

tension can be found in Appendix (**A**).

The notion of a particle in this framework arises from the configuration of an open string stretched between two distinct D-branes. Consider, for instance, a scenario where one endpoint of the open string is attached to a D3-brane and the other to a D7-brane. In this setup, the mass of the corresponding particle can be interpreted as arising from the tension of the open string and the spatial separation between the branes, specifically measured along the transverse directions.

The mass of the fundamental mode of the string, interpreted as a particle, is given by

$$m = T_{\text{open}} \cdot L = \frac{L}{2\pi\alpha'}, \tag{2.27}$$

where $T_{\text{open}} = 1/2\pi\alpha'$ is the tension of the open string, and L is the transverse distance between the two branes (AMMON; ERDMENGER, 2015).

From this expression, it follows that the particle is massless when the branes coincide ($L = 0$), and acquires mass when they are separated. In this way, the massive spectrum of the theory is generated from the geometry of brane configurations.

An open string can oscillate basically in two different ways: in and out of the brane. As we want to apply this construction for a 4D gauge theory, we can illustrate with an example. The oscillations that happen in the brane represent the gauge fields whereas all the oscillation out of the brane would represent scalars. That is the way we interpret the oscillations with a physical meaning.

There is a great discussion about the dimensionality relation on this perspective. I will illustrate it here. You can check the details on (NATSUUME, 2016). Remember: we want to construct a relation between a superstring theory defined in 10 dimensions and

a 4D gauge theory. As discussed above, the 4D gauge theory is represented by the D3 brane. But how could we think about the oscillations of an open string? The open strings are oscillating in the full 10-dimensional space, indeed. Inside this space, we have one time dimension and 9 spatial dimensions. Considering just the spatial ones, we have 6 spatial dimensions outside the D3-brane. The conclusion is: we have 6 scalar fields on this structure. These scalar fields are related with the degrees of freedom of this configuration.

In the case of $\mathcal{N} = 4$ Super Yang–Mills theory in four dimensions, the fields that compose the supersymmetric multiplet arise from the quantization of open strings with endpoints attached to a D3-brane. The table below summarizes these fields, indicating their types, quantities, and the associated physical degrees of freedom.

Field	**Type**	**Quantity**	**Degrees of Freedom**
A_μ	Vector (spin 1)	1	2 (transverse polarizations)
ϕ^i	Real scalars (spin 0)	6	6
λ^a	Weyl fermions (spin 1/2)	4	$4 \times 2 = 8$

TABLE 2.1 – Fields and physical degrees of freedom in the $\mathcal{N} = 4$ SYM multiplet in 4D.

It is important to note that the balance between bosonic and fermionic degrees of freedom is a defining feature of supersymmetry. In the $\mathcal{N} = 4$ SYM multiplet, we have a total of $2 + 6 = 8$ bosonic degrees of freedom—2 from the gauge field A_μ and 6 from the scalar fields ϕ^i. On the fermionic side, there are 4 Weyl fermions [6], each contributing 2 degrees of freedom, totaling $4 \times 2 = 8$. This exact matching between bosonic and fermionic degrees of freedom ensures the off-shell closure of the supersymmetry algebra and reflects the high degree of symmetry present in the $\mathcal{N} = 4$ theory, which is also conformally invariant in four dimensions.

[6] Weyl fermions are massless spin-$\frac{1}{2}$ particles described by two-component spinors. In four-dimensional theories, they represent the chiral components of Dirac fermions—massive particles that combine both left- and right-handed chiralities into a four-component spinor. Weyl fermions play a central role in supersymmetric models due to their transformation properties under the Lorentz group.

In summary, the fundamental spectrum of Type IIB superstring theory contains only closed strings, meaning that open strings do not propagate freely within the purely perturbative regime. However, when D-branes—non-perturbative solutions of the theory—are introduced, open strings can emerge with their endpoints attached to these branes. This allows for the interpretation of particles as modes of open strings, such as gauge fields or fermions.

In holographic contexts like the AdS/CFT correspondence, these open strings attached to D-branes play a crucial role in modeling matter (e.g., quarks and mesons), while closed strings continue to describe gravity in the bulk. Therefore, although D-branes are not part of the original perturbative spectrum of Type IIB theory, they are essential for extending the theory and enabling realistic physical applications, such as the study of compact objects, quark-gluon plasmas, and strongly coupled nuclear matter.

2.3 QCD fundamentals

Since the advent of the Quantum Cromodynamics, enormous advances have been made to increase our knowledge of the strong interaction. In particular, QCD has very accurate predictions for high energies collisions of hadrons, where asymptotic freedom is ensured. Nevertheless, at the low-energy region, there are still conceptual questions that challenge us as the mass gap, confinement and the linear Regge trajectories.

There are non-perturbative approaches to QCD. The most successful is lattice QCD (KOGUT, 1983), which relies on a discretization of the Euclidean spacetime and requires a massive computational power. It is worth to cite also the dynamical models based on the solution of integral equations as Dyson-Schwinger equations (ROBERTS; WILLIAMS, 1994)

and the Bethe-Salpeter equations (PAULA *et al.*, 2016).

In this context, holographic models are a new tool to investigate non-perturbative QCD. The goal is to build a model capable to capture some features of QCD and investigate low-energy phenomena. This is precisely our goal, as it enables the investigation of environments where nuclear matter is subjected to extreme conditions, such as those found in compact astrophysical objects. To achieve this, we must first contextualize the challenges involved in constructing models that effectively mimic QCD, particularly in its strongly coupled regime where traditional methods break down.

In this section, we will present fundamental aspects of Quantum Chromodynamics (QCD) that are central to the construction of its holographic dual. The discussion will focus on two key features of the theory: the strong coupling regime, where perturbative techniques fail, and the phenomena of confinement and chiral symmetry breaking, which play a crucial role in the low-energy behavior of QCD. Understanding these elements is essential for developing reliable holographic models that aim to capture the non-perturbative dynamics of strongly coupled gauge theories.

2.3.1 Fundamental Features of QCD

Quantum Chromodynamics (QCD) is a local gauge theory based on the non-Abelian symmetry group $SU(3)_c$, where the subscript c refers to color. As a Yang–Mills theory, QCD is formulated to be locally invariant under $SU(3)_c$ transformations at each point in spacetime. It describes the strong interaction between quarks and gluons, which are the fundamental fields of the theory.

Quarks are spin-1/2 fermions that transform under the fundamental representation

of $SU(3)_c$. They carry one of three color charges—red, green, or blue—and come in six flavors: up, down, charm, strange, top, and bottom. These quantum numbers determine how quarks interact via the strong force.

Gluons are the gauge bosons associated with the $SU(3)_c$ symmetry and serve as mediators of the strong force. They belong to the adjoint representation of the gauge group and are responsible for exchanging color charge between quarks. There are eight gluons in total, corresponding to the eight generators of the $SU(3)$ algebra, typically represented by the Gell-Mann matrices. Unlike photons in Quantum Electrodynamics (QED), gluons themselves carry color charge, allowing them to interact with each other. This feature gives rise to gluon self-interactions, making QCD a highly non-linear and complex theory, particularly in its strongly coupled, non-perturbative regime.

The fundamental dynamics of Quantum Chromodynamics (QCD) are encoded in its Lagrangian density, which governs the behavior of quarks and gluons under the local $SU(3)_c$ gauge symmetry

$$\mathcal{L}_{\text{QCD}} = -\frac{1}{4} F^a_{\mu\nu} F^{\mu\nu,a} + \sum_{f=1}^{N_f} \bar{\psi}_f \left(i\gamma^\mu D_\mu - m_f \right) \psi_f \tag{2.28}$$

In this expression:

- $F^a_{\mu\nu}$ is the non-Abelian field strength tensor of the gluon field, defined as

$$F^a_{\mu\nu} = \partial_\mu A^a_\nu - \partial_\nu A^a_\mu + g_s f^{abc} A^b_\mu A^c_\nu, \tag{2.29}$$

where A^a_μ are the eight gluon gauge fields, g_s is the strong coupling constant, and f^{abc} are the structure constants of the $SU(3)$ Lie algebra, reflecting the non-Abelian nature of the

gauge group.

- The first term in the Lagrangian, $-\frac{1}{4}F^a_{\mu\nu}F^{\mu\nu,a}$, describes the self-interactions of the gluons, a unique feature of non-Abelian gauge theories that leads to the non-linear dynamics of QCD.

- The second term sums over all quark flavors $f = 1, \ldots, N_f$, where ψ_f denotes the Dirac spinor field for the quark of flavor f, and m_f is its corresponding mass.

- The covariant derivative is given by

$$D_\mu = \partial_\mu - ig_s A^a_\mu T^a, \tag{2.30}$$

where T^a are the generators of the $SU(3)_c$ group in the fundamental representation, acting on the color indices of the quark fields.

- The term $\bar{\psi}_f(i\gamma^\mu D_\mu)\psi_f$ describes the kinetic energy and gauge interaction of quarks with gluons, while $m_f\bar{\psi}_f\psi_f$ is the mass term for each quark flavor.

Altogether, this Lagrangian captures the rich structure of QCD, including asymptotic freedom at high energies and color confinement at low energies—two key features that emerge from its non-Abelian gauge structure. We will explore these concepts in the following sections.

2.3.2 Asymptotic Freedom and the Running Coupling

A fundamental property that distinguishes Quantum Chromodynamics (QCD) from other gauge theories is the way its coupling constant evolves with the energy scale. In QCD, the strength of the interaction between quarks and gluons is not fixed—it depends

on the energy μ at which the process takes place. This behavior, known as the *running of the coupling constant*, is a direct consequence of the renormalization group and is central to understanding the theory across different energy regimes.

The energy dependence of the strong coupling $g_s(\mu)$ is governed by the renormalization group equation

$$\mu \frac{dg_s}{d\mu} = \beta(g_s), \tag{2.31}$$

where $\beta(g_s)$ is the so-called beta function [7] . At one-loop order in perturbation theory, the QCD beta function is given by (AMMON; ERDMENGER, 2015)

$$\beta(g_s) = -\frac{g_s^3}{48\pi^2}\left(11\ N_c - 2\ N_f\right), \tag{2.32}$$

with N_c representing the number of colors (equal to 3 in QCD) and N_f the number of active quark flavors at the scale μ.

The sign of the beta function is determined by the balance between the self-interactions of the gluons (which dominate for small N_f) and the screening effect due to virtual quark loops. As long as $N_f < \frac{11}{2}N_c$, the coefficient in parentheses remains positive, resulting in a negative beta function

$$\beta(g_s) < 0 \quad \Rightarrow \quad \mu \uparrow \Rightarrow\ g_s(\mu) \downarrow . \tag{2.33}$$

This means that the coupling becomes weaker at higher energies, a phenomenon known as **asymptotic freedom**. In the ultraviolet regime (large μ, corresponding to short

[7] We previously mentioned the concept of the beta function in the context of the Wilson–Kadanoff renormalization group approach applied to extra dimensions. See equation (2.4) for reference.

distances), quarks and gluons interact weakly and behave nearly as free particles. This justifies the use of perturbative techniques, which have proven remarkably successful in describing high-energy processes, such as those probed in particle colliders.

In contrast, as the energy decreases, the situation changes drastically. The coupling becomes stronger as the scale approaches a characteristic value $\Lambda_{\rm QCD}$, associated with the onset of non-perturbative dynamics

$$\mu \to \Lambda_{\rm QCD} \quad \Rightarrow \quad g_s(\mu) \gg 1. \tag{2.34}$$

Here, perturbation theory breaks down, and phenomena like *confinement* and *spontaneous chiral symmetry breaking* emerge. These effects dominate the infrared (IR) regime of the theory and lie beyond the reach of standard perturbative methods.

Understanding the scale dependence of the strong coupling is thus crucial—not only for calculating cross-sections at high energies but also for motivating alternative approaches to describe the strongly coupled phase of QCD. These include lattice QCD, effective field theories, and holographic dual models, which we will explore in the upcoming sections.

2.3.3 Confinement and Chiral Symmetry Breaking

At low energies, Quantum Chromodynamics (QCD) enters a regime in which the strong coupling constant becomes large and perturbative techniques cease to be reliable. In this infrared domain, QCD exhibits two deeply interrelated and nonperturbative phenomena: confinement and the spontaneous breaking of chiral symmetry.

These features are not only central to the theoretical structure of the theory but also

essential for explaining the empirical properties of hadronic matter. Understanding them is one of the great challenges of modern high-energy physics and a major motivation for the development of effective models and alternative frameworks such as lattice QCD and holography.

Confinement refers to the fact that quarks and gluons, although fundamental fields in the QCD Lagrangian, are never observed as free particles in nature. Instead, they are permanently bound into color-singlet combinations, such as mesons and baryons. One intuitive way to understand this phenomenon is through the concept of the color flux tube. When a quark and an antiquark are pulled apart, the gluon field lines between them do not spread like in electrodynamics but instead collapse into a narrow tube due to the self-interactions of gluons. The energy stored in this flux tube increases linearly with the distance between the quarks (AMMON; ERDMENGER, 2015)

$$V(r) \sim \sigma r, \tag{2.35}$$

where σ is the string tension. Once the energy becomes large enough, it becomes energetically favorable to create a new quark–antiquark pair from the vacuum, resulting in the formation of two mesons — a process known as hadronization. Formally, confinement can be diagnosed by analyzing the behavior of Wilson loops (WILSON, 1974). In a confining theory, the vacuum expectation value of a rectangular Wilson loop $W(C)$ obeys an area law (AMMON; ERDMENGER, 2015)

$$\langle W(C) \rangle \sim e^{-\sigma A(C)}, \tag{2.36}$$

where $A(C)$ is the area enclosed by the loop. This behavior is interpreted as evidence for

a linearly growing potential and the impossibility of isolating color charges.

Another remarkable consequence of confinement is the presence of a *mass gap* in the spectrum of QCD. This means that, even though gluons are massless at the level of the Lagrangian, the theory does not admit physical excitations with arbitrarily low energy. The lowest-lying color-singlet states, such as glueballs or mesons, have a finite mass — a manifestation of the strongly coupled nature of the vacuum. The existence of this mass gap is intimately connected to confinement and remains one of the unsolved problems of theoretical physics.

The second key phenomenon at low energies is the spontaneous breaking of chiral symmetry. In the limit where the light quark masses vanish, the QCD Lagrangian possesses a global chiral symmetry [8] of the form $SU(N_f)_L \times SU(N_f)_R$, corresponding to independent rotations of the left- and right-handed components of the quark fields

$$q_L = \frac{1-\gamma^5}{2}\, q, \quad q_R = \frac{1+\gamma^5}{2}\, q. \tag{2.37}$$

However, the QCD vacuum does not respect this symmetry. Instead, it develops a non-vanishing quark condensate,

$$\langle \bar{q} q \rangle \neq 0, \tag{2.38}$$

which mixes left- and right-handed components and signals the spontaneous symmetry

[8] If a mass term such as $\mathcal{L}_{m_q} = -m_q \bar{\psi}\psi$ — with ψ a Dirac spinor — is present in the Lagrangian, chiral symmetry is explicitly broken. See the full explanation in (AMMON; ERDMENGER, 2015).

breaking pattern

$$SU(N_f)_L \times SU(N_f)_R \longrightarrow SU(N_f)_V. \tag{2.39}$$

As a consequence of this global symmetry breaking, Goldstone's theorem predicts the emergence of massless pseudoscalar bosons. For two light flavors (u and d), these are identified with the pions (π^+, π^0, π^-), which acquire a small mass due to the explicit breaking of chiral symmetry by the quark masses. The non-vanishing commutator between the quark condensate and the axial charge Q_A^a further confirms the spontaneous nature of the symmetry breaking

$$[Q_A^a, \bar{q}q] \neq 0. \tag{2.40}$$

In summary, confinement and spontaneous chiral symmetry breaking are essential features that characterize the low-energy behavior of QCD. Any model that aims to investigate QCD in this regime must be able to reproduce both phenomena in a consistent way. This represents a major theoretical challenge, especially due to the limitations of perturbative methods. One of the key advantages of using holographic models to study QCD-like theories is precisely their ability to access strongly coupled phenomena that are still not fully understood by traditional approaches.

2.3.4 Modeling QCD in the Strong Coupling Regime

In the low-energy regime of QCD, where the coupling becomes strong and perturbation theory breaks down, understanding the dynamics of quarks and gluons requires

nonperturbative approaches. Over the years, a variety of models has been developed in the literature to describe different aspects of QCD under these conditions. Although each of them highlights specific features, they all aim to explore the physics of strongly interacting matter in regimes inaccessible to perturbative techniques.

Among the earliest and most widely used models is the MIT Bag Model (CHODOS *et al.*, 1974), which treats quarks as free particles confined within a finite region of space, with a constant bag pressure simulating confinement. Despite its simplicity, the model has been successful in describing hadronic structure and has been extensively applied to the study of quark matter and its equation of state in astrophysical scenarios (NEGREIROS *et al.*, 2012) (NAKAZATO *et al.*, 2008).

Another popular approach is provided by the Nambu–Jona-Lasinio (NJL) model (NAMBU; JONA-LASINIO, 1961), which, although lacking confinement, effectively describes spontaneous chiral symmetry breaking through four-fermion interactions. Extensions such as the Polyakov-loop NJL (PNJL) model (FUKUSHIMA, 2004) incorporate aspects of confinement via a phenomenological Polyakov loop potential. These models have proven useful for investigating the QCD phase diagram and chiral transitions, especially at finite temperature and density.

Relativistic mean-field (RMF) theories (LALAZISSIS *et al.*, 1997) offer a meson-mediated description of baryonic interactions and have been widely adopted in nuclear physics and astrophysics. Parametrizations such as NL3* are known to reproduce both nuclear saturation properties and observational constraints from neutron stars, and will be introduced in the following chapters as the framework used in our holographic model to describe the hadronic sector in the study of hybrid stars.

Another promising line of research involves holographically inspired bottom-up models,

which aim to encode known QCD features by constructing dual gravitational theories. A prominent example is the V-QCD model (JARVINEN; KIRITSIS, 2012), built in the Veneziano limit ($N_f, N_c \to \infty$ with fixed $x = N_f/N_c$, where N_f and N_c state for flavor and color numbers respectively), which couples improved holographic QCD for the gluon sector with a tachyonic action for the flavor fields. It captures both confinement and chiral symmetry breaking in a unified framework, with dynamical backreaction between the sectors. Another one is the Einstein-Maxwell-Dilaton (EMD) model. In this setup, the background geometry is modified via a warp factor to mimic infrared QCD behavior to derive an equation of state for dense nuclear matter (MAMANI *et al.*, 2020).

A complementary and more fundamental perspective is offered by top-down models, derived directly from string theory constructions. The Sakai–Sugimoto model (SAKAI; SUGIMOTO, 2005) stands as the most prominent example. Based on a D4/D8/$\overline{\text{D8}}$ brane configuration, it naturally realizes chiral symmetry breaking and confinement through geometric mechanisms and has been applied to various low-energy QCD phenomena.

Another top-down construction, which forms the core of the present thesis, is the D3/D7 brane model (KARCH; KATZ, 2002). This setup introduces fundamental matter via probe D7-branes embedded in the $\text{AdS}_5 \times S^5$ background generated by D3-branes. It provides a controlled way to study the thermodynamics and transport of strongly coupled plasmas with fundamental degrees of freedom, and, more recently, has been adapted to investigate dense quark matter in compact astrophysical objects. The applications of this model to the description of quark stars and hybrid stars will be developed in the next chapters.

Each of these models contributes uniquely to our understanding of QCD in the non-perturbative regime. While no single approach is complete, together they form a diverse

and complementary toolkit for addressing the infrared structure of strongly coupled gauge theories and their implications in nuclear and astrophysical systems.

2.4 The correspondence

The AdS/CFT correspondence, or gauge/gravity duality, is a conjecture that proposes an exact equivalence between a gravitational theory in a higher-dimensional spacetime and a quantum field theory without gravity defined on its boundary.

This idea was first formulated by Juan Maldacena in 1997, in his seminal paper titled *The Large N Limit of Superconformal Field Theories and Supergravity* (MALDACENA, 1998). In that work, it was conjectured that type IIB superstring theory on an $AdS_5 \times S^5$ background is dual to $\mathcal{N} = 4$ Super Yang–Mills (SYM) theory in four spacetime dimensions, with gauge group $SU(N_c)$.

This duality is holographic in nature: it suggests that a theory with gravity in $(d+1)$ dimensions can encode the dynamics of a theory without gravity in d dimensions. This relationship can be summarized as follows

$$\begin{array}{c}\textbf{type IIB Super String Theory} \\ \text{on } AdS_5 \times S^5\end{array} \quad \Longleftrightarrow \quad \begin{array}{c}\mathcal{N} = 4 \quad \textbf{SU}(N_c)\ \textbf{Super Yang–Mills} \\ \text{in 4 dimensions.}\end{array}$$

The geometry of the Anti-de Sitter space plays a central role in this correspondence. From (2.24), the five-dimensional AdS space can be written in Poincaré coordinates as

$$ds^2 = \frac{R^2}{z^2}\left(-dt^2 + d\vec{x}^2 + dz^2\right), \tag{2.41}$$

where R and z are the radius and the radial coordinate of AdS, respectively. The boundary of the space lies at $z = 0$, which is where the conformal field theory is defined. Moving

along the radial direction corresponds to probing different energy scales in the boundary theory: small z corresponds to high energy (UV), while large z corresponds to low energy (IR), deep into the bulk.

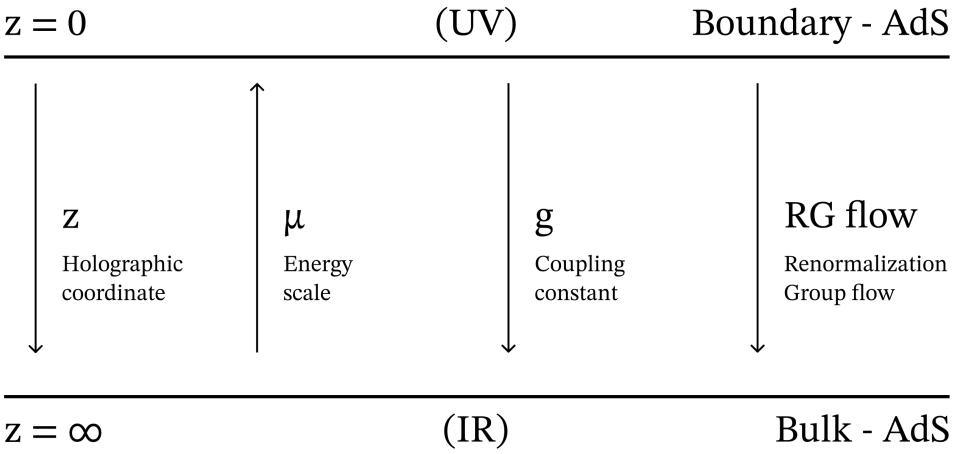

FIGURE 2.8 – Bulk/boundary structure and its energy-scale interpretation in Poincaré coordinates for QCD-like theory.

Figure 2.8 illustrates this bulk/boundary structure and its energy-scale interpretation. In global coordinates, the boundary is located at $z \to \infty$, but the physical role remains the same—the field theory always resides at the boundary.

This geometric interpretation becomes even more meaningful when we compare it to QCD, whose coupling constant evolves with the energy scale. The negative sign of its beta function implies that the interaction becomes weaker at high energies and stronger at low energies, a property known as asymptotic freedom. The correspondence thus offers a natural framework to model this behavior using the radial coordinate of AdS.

However, it is important to note that not all conformal field theories exhibit QCD-like behavior. In particular, the $\mathcal{N} = 4$ Super Yang–Mills theory is exactly conformal for all

energy scales, meaning that its beta function vanishes identically

$$\beta(g_{\mathrm{YM}}) = 0. \tag{2.42}$$

This implies the absence of a renormalization group (RG) flow in the traditional sense — there is no change in the coupling with respect to the energy scale μ. Geometrically, the RG flow is interpreted as a trajectory in the space of couplings, but for $\mathcal{N} = 4$ SYM this trajectory becomes trivial.

As a consequence, the notions of weak and strong coupling in this theory do not arise from scale dependence, but rather from the fixed value of the 't Hooft coupling $\lambda = g^2_{\mathrm{YM}} N_c$. The regime of the theory is therefore determined by the magnitude of this parameter: when $\lambda \ll 1$, the gauge theory is weakly coupled and perturbative methods apply; when $\lambda \gg 1$, the theory becomes strongly coupled and the dual gravitational description becomes classical.

The strength of the correspondence lies in its ability to map a strongly coupled gauge theory into a weakly curved gravitational background, allowing computations that would otherwise be intractable. In the following sections, we explore how bulk fields correspond to boundary operators and how correlation functions can be computed holographically—core elements of what is known as the holographic dictionary.

2.4.1 Dictionary and field-operator mapping

A central element of the AdS/CFT correspondence is the holographic dictionary, which establishes a precise connection between fields propagating in the bulk and operators defined in the boundary field theory. This mapping provides the fundamental bridge that

allows one to compute observables in a strongly coupled quantum field theory through a dual weakly coupled gravitational theory.

In this duality, the bulk theory is formulated in a $(d+1)$-dimensional spacetime (such as AdS_5 in the case of the original conjecture), while the conformal field theory (CFT) resides on its d-dimensional boundary. The basic rule of the dictionary can be summarized as

$$\boxed{\phi(z,x) \quad \longleftrightarrow \quad \mathcal{O}(x).} \tag{2.43}$$

where $\phi(z,x)$ is a bulk field and $\mathcal{O}(x)$ is a local operator in the boundary theory. The boundary value of the field ϕ, denoted $\phi_0(x)$, plays the role of a source for the operator $\mathcal{O}$ in the generating functional of the CFT.

This relation becomes more concrete through the statement that the partition function of the string (or supergravity) theory evaluated with boundary condition ϕ_0 is equal to the generating functional of the boundary field theory (WITTEN, 1998)

$$Z_{\text{string}}[\phi_0] = \left\langle \exp\left(\int d^d x \, \phi_0(x) \, \mathcal{O}(x) \right) \right\rangle_{\text{CFT}}. \tag{2.44}$$

In the classical (supergravity) limit, this simplifies to

$$Z_{\text{string}}[\phi_0] \approx e^{-S_{\text{grav}}^{\text{on-shell}}[\phi_0]}. \tag{2.45}$$

This identification allows us to compute boundary correlators by differentiating the classical on-shell action with respect to the sources $\phi_0(x)$. In this way, each field in the bulk theory corresponds to a specific operator in the boundary theory, and their scaling

dimensions and spins must match appropriately. Table (2.2) presents a standard way of illustrating how this identification can be established through the holographic dictionary.

Bulk Field	**Boundary Operator**
Scalar ϕ	Scalar operator $\mathcal{O}$
Gauge field A_M	Conserved current J^μ
Metric g_{MN}	Energy–momentum tensor $T^{\mu\nu}$

TABLE 2.2 – Standard holographic dictionary in $\mathrm{AdS}_{d+1}/\mathrm{CFT}_d$.

A fundamental consequence of the correspondence is the relation between the mass of a scalar field in the AdS bulk and the conformal dimension of the dual operator. We will explicitly show how this relation is derived in what follows, but a more comprehensive discussion can be found in (RAMALLO, 2015). This relation can be derived explicitly by starting from the action for a scalar field ϕ in AdS_{d+1}

$$S = -\frac{1}{2}\int d^{d+1}x\sqrt{g}\left(g^{MN}\partial_M\phi\partial_N\phi + m^2\phi^2\right). \tag{2.46}$$

The equation of motion, the Klein-Gordon equation, is obtained from the Euler–Lagrange equation

$$\frac{1}{\sqrt{g}}\,\partial_M\left(\sqrt{g}\;g^{MN}\;\partial_N\phi\right) - m^2\phi = 0. \tag{2.47}$$

Using the AdS_{d+1} metric in Poincaré coordinates

$$ds^2 = \frac{R^2}{z^2}\left(dz^2 + \eta_{\mu\nu}\,dx^\mu dx^\nu\right), \tag{2.48}$$

we find the relevant components

$$\sqrt{g} = \left(\frac{R}{z}\right)^{d+1}, \quad g^{zz} = \frac{z^2}{R^2}, \quad g^{\mu\nu} = \frac{z^2}{R^2}\,\eta^{\mu\nu}. \tag{2.49}$$

Inserting these into the equation of motion gives

$$z^{d+1}\partial_z\left(z^{-d+1}\partial_z\phi\right) + z^2\,\eta^{\mu\nu}\,\partial_\mu\partial_\nu\phi - m^2R^2\phi = 0. \tag{2.50}$$

To proceed, we perform a Fourier transform in the boundary coordinates

$$\phi(z, x^\mu) = \int \frac{d^dk}{(2\pi)^d}\,e^{ik\cdot x}\,f_k(z). \tag{2.51}$$

Using the Fourier transform property for derivatives, this gives $\partial_\mu\partial^\mu\phi \to -k^2\phi$, and the equation becomes

$$z^{d+1}\partial_z\left(z^{-d+1}\partial_z\,f_k(z)\right) + \left(-k^2z^2 - m^2R^2\right)f_k(z) = 0. \tag{2.52}$$

In the asymptotic limit $z \to 0$, we can neglect the k^2 term, so the equation simplifies to

$$z^{d+1}\partial_z\left(z^{-d+1}\partial_z f(z)\right) - m^2R^2f(z) = 0. \tag{2.53}$$

Assuming the ansatz of a power-law behavior near the boundary, $f(z) = z^\Delta$, we

compute

$$\partial_z \, f(z) = \Delta z^{\Delta-1}; \tag{2.54}$$

$$\partial_z \left(z^{-d+1} \partial_z \, f(z) \right) = \Delta(\Delta - d) z^{\Delta-d-1}; \tag{2.55}$$

$$z^{d+1} \cdot \Delta(\Delta - d) \, z^{\Delta-d-1} = \Delta(\Delta - d) \, z^{\Delta}. \tag{2.56}$$

Substituting back into the equation gives

$$\left[\Delta(\Delta - d) - m^2 R^2 \right] z^{\Delta} = 0, \tag{2.57}$$

and thus

$$\Delta \, (\Delta - d) = m^2 R^2. \tag{2.58}$$

This relation determines the conformal dimension of the boundary operator dual to a bulk scalar of mass m in AdS_{d+1}. For the original $\mathrm{AdS}_5/\mathrm{CFT}_4$ case, this becomes $\Delta(\Delta - 4) = m^2 R^2$. Since this equation admits two solutions, $\Delta_{\pm} = \frac{d}{2} \pm \sqrt{\frac{d^2}{4} + m^2 R^2}$, it is common to choose the larger one when both lead to normalizable modes[9].

Interestingly, a remarkable feature of AdS spacetimes is that they allow the existence of scalar fields with negative mass squared without leading to instabilities, provided a lower bound is satisfied. This is known as the Breitenlohner–Freedman (BF) bound,

[9] In certain cases, the smaller root Δ_- also yields a valid quantization. The choice depends on the range of m^2 and physical boundary conditions.

which ensures stability

$$m^2R^2 \geq -\frac{d^2}{4}. \tag{2.59}$$

Therefore, bulk fields with small negative masses—interpreted as tachyonic in flat space—can be perfectly physical in AdS if they respect this bound.

The conformal dimension Δ plays a crucial role in the AdS/CFT dictionary, as it determines the scaling behavior of the dual operator and governs correlation functions, operator product expansions, and response to sources. In this sense, Δ is one of the key quantities used to map bulk physics to field-theoretic data.

It is important to emphasize that the explicit form of the holographic dictionary may vary depending on the specific model under consideration. Different choices of supergravity theories, compactifications, boundary conditions, and global symmetries may alter the precise structure of the correspondence. For example, in top-down constructions such as D-brane embeddings, additional constraints emerge from string theory. In contrast, bottom-up phenomenological models may involve modified asymptotics or effective interactions. Nevertheless, the conceptual role of the dictionary remains the same: it links boundary observables to bulk dynamics in a geometrically dual formulation.

2.4.2 The conformal transformation

In the AdS/CFT duality the underlying theories exhibit conformal invariance. One consequence is the scale invariance, that is

$$g'_{\mu\nu}(x') = \Lambda(x)\, g_{\mu\nu}(x), \tag{2.60}$$

or

$$dx'^2 = \Omega(x)^2\, dx^2 \;\;,\;\; dx^2 = \eta_{\mu\nu}\, dx^\mu\, dx^\nu, \tag{2.61}$$

being $\eta_{\mu\nu} = \text{diag}(-1, 1, ..., 1)$ the Minkowski flat space metric or $\eta_{\mu\nu} = \delta_{\mu\nu}$ the Euclidean metric. For $\Omega = 1$, the case is reduced to the Lorentzian transformations in the Minkowski space.

A general infinitesimal transformation can be done as it follows

$$x'^\mu = x^\mu + v^\mu(x) \;\;,\;\; \Omega(x) = 1 + \sigma(x). \tag{2.62}$$

Considering terms just with the first-order, equation (2.61) becomes

$$\partial_\mu\, v_\nu + \partial_\nu\, v_\mu = 2\sigma\, \eta_{\mu\nu}. \tag{2.63}$$

From equation (2.63), it is possible to write

$$\partial_\mu v^\mu = d\, \sigma \;\;,\;\; d = \eta^\mu_\mu. \tag{2.64}$$

By using equation (2.63), after some manipulations, we get

$$\frac{1}{2}\left(\partial_\rho(\partial_\mu\, v_\nu + \partial_\nu\, v_\mu) + \partial_\nu(\partial_\mu\, v_\rho + \partial_\rho\, v_\mu) - \partial_\mu(\partial_\rho\, v_\nu + \partial_\nu\, v_\rho)\right)$$

$$\partial_\rho\partial_\nu v_\mu = \partial_\rho\sigma\ \eta_{\mu\nu} + \partial_\nu\sigma\ \eta_{\mu\rho} - \partial_\mu\sigma\ \eta_{\rho\nu}. \tag{2.65}$$

Acting on the last equation with ∂^μ

$$(d-2)\partial_\rho\partial_\nu\sigma = -\eta_{\rho\nu}\,\partial^2\sigma, \tag{2.66}$$

which leads to

$$(d-1)\,\partial^2\sigma = 0, \tag{2.67}$$

$$(d-1)(d-2)\,\partial_\rho\partial_\nu\sigma = 0. \tag{2.68}$$

Except for the 1D trivial dimension, $\partial^2\sigma = 0$, and for $d \neq 2$, $\partial_\rho\partial_\nu\sigma = 0$ and considering that σ is linear in x

$$\sigma = \kappa - 2b_\mu x^\mu. \tag{2.69}$$

From equation (2.65), one can write

$$\partial_\rho\partial_\nu v_\mu = -2b_\rho\eta_{\mu\nu} + 2b_\mu\eta_{\rho\nu} - 2b_\nu\eta_{\mu\rho}, \tag{2.70}$$

that after an integration considering (2.64)

$$v_\mu(x) = a_\mu + \omega_{\mu\nu}x^\nu + \kappa x_\mu + b_\mu x^2 - 2x_\mu b_\nu x^\nu \quad , \quad \omega_{\mu\nu} = -\omega_{\nu\mu}, \tag{2.71}$$

where the first term a_μ is responsible for the d translations, the second one $\omega_{\mu\nu}x^\nu$ to the $\frac{d(d-1)}{2}$ rotations/boosts, the third one κx_μ to one scale transform, the forth and fifth ones $b_\mu x^2 - 2x_\mu b_\nu x^\nu$ related to the d special conformal transformations.

The total number of parameters defining the conformal transformation is $\frac{(d+1)(d+2)}{2}$. The solutions of (2.63) represent the conformal Killing vectors.

Testing for the $\mathcal{N} = 4$ SYM we can see that our previous information of 15 generators is correct.

Sometimes it is easier to see these generators presented into different forms. The infinitesimal conformal transformations can be written in terms of generators G acting on the coordinates x^μ as

$$\delta x^\mu = x'^\mu - x^\mu = i\epsilon \cdot G\, x^\mu, \tag{2.72}$$

where G is any of the following differential operators

$$P_\mu = -i\,\partial_\mu \qquad \text{translations,} \tag{2.73}$$

$$M_{\mu\nu} = i\,(x_\mu \partial_\nu - x_\nu \partial_\mu) \qquad \text{Lorentz transformations,} \tag{2.74}$$

$$D = -i\,(x \cdot \partial) \qquad \text{dilatations (scale),} \tag{2.75}$$

$$K_\mu = -i\,(2x_\mu (x \cdot \partial) - x^2 \partial_\mu) \qquad \text{special conformal transformations.} \tag{2.76}$$

Generators P^μ and $M^{\mu\nu}$ span the Poincaré group and they have the following commutation relations

$$[P_\mu, M_{\rho\sigma}] = i\,(g_{\mu\rho}\, P_\sigma - g_{\mu\sigma} P_\rho), \tag{2.77}$$

$$[M_{\mu\nu}, M_{\rho\sigma}] = i\,(g_{\mu\sigma} M_{\nu\rho} + g_{\nu\rho} M_{\mu\sigma} - g_{\mu\rho} M_{\nu\sigma} - g_{\nu\sigma} M_{\mu\rho}). \tag{2.78}$$

The commutation relations with the other generators are

$$[D, P_\mu] = +i\, P_\mu, \tag{2.79}$$

$$[D, K_\mu] = -i\, K_\mu, \tag{2.80}$$

$$[K_\mu, P_\nu] = 2i\, (g_{\mu\nu}\, D - \ M_{\mu\nu}), \tag{2.81}$$

$$[K_\mu, M_{\rho\sigma}] = i\, (g_{\mu\rho}\, K_\sigma - g_{\mu\sigma}\, K_\rho), \tag{2.82}$$

with all other commutators vanishing. For more details check (RYDER, 1996).

2.4.3 Correlation functions

Correlation functions are fundamental observables in quantum field theory, measuring how local operators inserted at different spacetime points are statistically related. In a conformal field theory (CFT), these functions not only reveal information about the spectrum of operators but also reflect the underlying symmetries and dynamics of the theory.

Physically, a correlation function addresses the question: if we perturb the vacuum at a point x by inserting an operator $\mathcal{O}(x)$, how does this affect measurements of the same or another operator at a different point y? A strong effect indicates high correlation; little to no effect suggests weak or vanishing correlation.

In the context of the AdS/CFT correspondence, boundary correlation functions are dual to bulk propagators. Specifically, the two-point correlation function in the CFT corresponds holographically to the bulk-to-boundary propagator of the associated field in AdS space. This geometric relationship allows us to extract quantum information from

the boundary theory via classical gravitational dynamics in the bulk.

Consider the two-point function, a primary example. The expectation value

$$\langle \mathcal{O}(x)\, \mathcal{O}(y) \rangle, \tag{2.83}$$

describes how a disturbance at x influences point y. In conformal field theories, this function's form is constrained by symmetry (AMMON; ERDMENGER, 2015)

$$\langle \mathcal{O}(x)\, \mathcal{O}(y) \rangle = \frac{C_\Delta}{|x-y|^{2\Delta}}, \tag{2.84}$$

where Δ is the conformal dimension of the operator $\mathcal{O}$, and C_Δ is a normalization constant.[10]

This structure arises from the scaling property of the operator $\mathcal{O}(x)$

$$\mathcal{O}(x) \to \lambda^{-\Delta}\, \mathcal{O}(\lambda x), \tag{2.85}$$

under a scale transformation $x \to \lambda x$. The product of two such operators then scales with dimension 2Δ, leading to the form of the two-point function.

Within the AdS/CFT framework, the boundary operator $\mathcal{O}$ is dual to a bulk field $\phi(z, x)$, whose boundary value $\phi_0(x)$ acts as a source. The two-point function is obtained from the second functional derivative of the bulk on-shell action (AMMON; ERDMENGER,

[10]This expression can also be written as $(|x-y|^2)^{-\Delta}$, emphasizing the dependence on the squared distance between points. For operators with different conformal dimensions Δ_1 and Δ_2, the two-point function generalizes to $\langle \mathcal{O}_1(x)\mathcal{O}_2(y) \rangle = \frac{C_{\Delta_1\Delta_2}}{|x-y|^{\Delta_1+\Delta_2}}$, reflecting the combined scaling behavior. (AMMON; ERDMENGER, 2015)

2015)

$$\langle \mathcal{O}(x)\, \mathcal{O}(y) \rangle = \left. \frac{\delta^2 S_{\text{on-shell}}[\phi_0]}{\delta\phi_0(x)\, \delta\phi_0(y)} \right|_{\phi_0=0}. \tag{2.86}$$

From the bulk perspective, this corresponds to evaluating the Green's function or propagator that connects points x and y on the boundary through bulk dynamics. The bulk field mediates the correlation, with its profile encoding the interaction's strength and range.

Extending to n-point functions (AMMON; ERDMENGER, 2015)

$$\langle \mathcal{O}(x_1)\, \mathcal{O}(x_2) \cdots\, \mathcal{O}(x_n) \rangle = \left. \frac{\delta^n S_{\text{on-shell}}[\phi_0]}{\delta\phi_0(x_1) \cdots \delta\phi_0(x_n)} \right|_{\phi_0=0}. \tag{2.87}$$

These functions encapsulate multi-point interactions and facilitate the reconstruction of the operator product expansion (OPE), a crucial structure in conformal theories.

The behavior of correlation functions varies:

- **Strong correlation**: The two-point function decays slowly with distance (small Δ), indicating long-range interactions or strong entanglement.
- **Weak or vanishing correlation**: The function decays rapidly (large Δ) or vanishes, suggesting statistical independence between points.

Practically, correlation functions are essential for diagnosing physical phenomena. In thermal states, they reveal transport properties (BHATTA *et al.*, 2023); in strongly coupled plasmas, they capture collective behavior (NIJS *et al.*, 2024); in critical systems, they determine scaling laws (BERCHE *et al.*, 2012).

In summary, correlation functions bridge bulk gravitational physics and boundary field dynamics in AdS/CFT, computed via bulk propagators, manifesting as non-local functions on the boundary, and encapsulating key physical properties such as mass spectra, operator dimensions, and interaction strengths.

2.4.4 Looking for symmetries

An important consequence of the AdS/CFT correspondence is the fact that the isometries of the metric of the gravitation theory are mapped into the symmetries of the field theory. Thus, in this section, we will identify how this relation is defined after understanding the structure of the AdS space.

2.4.4.1 The AdS space and its isometries

The generalized Einstein-Hilbert action in D dimensions has the form

$$S_{EH} = \frac{1}{16\,\pi\,G_D} \int d^D x\, \sqrt{|g|}\,(R + \Lambda), \tag{2.88}$$

where G_D is the Newton constant defined in D dimensions, R is the scalar curvature and Λ is the cosmological constant.

We can apply the Euler-Lagrange equation with respect to the metric $g_{\mu\nu}$ and obtain the *Einstein Equations*

$$R_{\mu\nu} - \frac{1}{2}\, g_{\mu\nu}\, R = \frac{1}{2}\, \Lambda\, g_{\mu\nu}, \tag{2.89}$$

where the $R_{\mu\nu}$ is the Ricci tensor.

One can take the trace of this expression to obtain

$$\mathrm{Tr}\,(2g^{\mu\nu}\,R_{\mu\nu} - g^{\mu\nu}\,g_{\mu\nu}\,R) = \mathrm{Tr}\,(\Lambda\,g^{\mu\nu}\,g_{\mu\nu})\,. \tag{2.90}$$

By using the relation $\mathrm{Tr}(g^{\mu\nu}\,g_{\mu\nu}) = D$, we can get

$$\begin{aligned}
&\mathrm{Tr}\,(2g^{\mu\nu}\,R_{\mu\nu}) - \mathrm{Tr}\,(g^{\mu\nu}\,g_{\mu\nu}\,R) = \mathrm{Tr}\,(\Lambda\,g^{\mu\nu}\,g_{\mu\nu}) \\
&\Rightarrow \mathrm{Tr}\,(2\,R^{\mu}_{\mu}) - \mathrm{Tr}\,(g^{\mu}_{\mu}\,R) = \mathrm{Tr}(\Lambda\,g^{\mu}_{\mu}) \\
&\Rightarrow 2\,R - D\,R = \Lambda\,D \\
&\Rightarrow R = \frac{\Lambda\,D}{(2-D)}.
\end{aligned} \tag{2.91}$$

One can substitute this expression in (2.89) to get

$$\begin{aligned}
&R_{\mu\nu} - \frac{1}{2}\,g_{\mu\nu}\left(\frac{\Lambda\,D}{2-D}\right) = \frac{1}{2}\,\Lambda\,g_{\mu\nu} \\
&\Rightarrow R_{\mu\nu} = \frac{1}{2}\,g_{\mu\nu}\left(\frac{\Lambda\,D}{2-D} + \Lambda\right) \\
&\Rightarrow R_{\mu\nu} = \frac{\Lambda}{2-D}\,g_{\mu\nu}.
\end{aligned} \tag{2.92}$$

That is an important relation. When the Ricci tensor is proportional to the metric tensor, we can say we are dealing with an *Einstein space*. And if the Λ is positive ($\Lambda > 0$) we have the de-Sitter (dS) space structure. On the other hand, if we have a negative Λ ($\Lambda < 0$), we get an Anti-de-Sitter (AdS) structure. The Anti-de-Sitter and the de-Sitter spaces are exact solutions of the vacuum Einstein equation (2.89) [11].

[11] The Minkowski space itself is another solution of the Einstein equation, but in this case, we have a **zero** curvature in opposition to the AdS and dS spaces, which have negative and positive curvatures, respectively.

The n-dimensional AdS space, AdS_n, is embedded in a $(n+1)$-dimensional space with 2 dimensions with *minus sign* and $(n-1)$ dimensions with a *plus sign*. We can represent this structure on the following

$$x_1^2 + \cdots + x_{n-1}^2 - x_n^2 - x_{n+1}^2 = a^2\,, \tag{2.93}$$

where a is the AdS radius. One can rewrite the previous equation on that form

$$x_{n+1}^2 = x_1^2 + \cdots + x_{n-1}^2 - x_n^2 - a^2\,. \tag{2.94}$$

Therefore, we have one coordinate defined from the others, i.e., we do have n independent dimensions.

To better understand the structure, one can set $n = 1$, getting the AdS_1. In this example, we get a space with 1 independent dimension living in a space with 2 dimensions, being one coordinate with a *minus sign* and another one having a *plus sign*. One could write

$$x_1^2 - x_2^2 = a^2. \tag{2.95}$$

Or it can be rewritten in the form

$$\left(\frac{x_1}{a}\right)^2 - \left(\frac{x_2}{a}\right)^2 = 1\,, \tag{2.96}$$

which is a hyperbole. For this reason, the AdS space is said to have the shape of a hyperboloid. From a group theory perspective, the AdS_{s+1} has SO(2,s) as its symmetry

group. Therefore, the AdS_5 has the SO(2,4) as its pseudo-orthogonal symmetry group.

The *AdS* space is said to be **maximally symmetric**. That property is important on the study of *homogeneous* [12] and *isotropic* [13] spaces. These two features of this kind of space are defined by how isometric the space is, that is, whether there are transformations that keep the invariance in space.

Isometries are defined as coordinate transformations of x into x' that leave a metric invariant, that is, $g_{\mu'\nu'}(x') = g_{\mu\nu}(x')$. In order to calculate all the isometries of a general metric, one can consider an infinitesimal coordinate transformation such as

$$x^\mu \quad \rightarrow \quad x'^\mu = x^\mu + \epsilon\,\xi^\mu \quad , \quad \epsilon \ll 1, \tag{2.97}$$

on the metric transformation

$$g_{\mu\nu}(x) = \frac{\partial x'^\rho}{\partial x^\mu}\frac{\partial x'^\sigma}{\partial x^\nu}\, g_{\rho\sigma}(x'). \tag{2.98}$$

After keeping linear terms in ϵ we get, after some manipulations, equation

$$\nabla_\nu\,\xi_\mu + \nabla_\mu\,\xi_\nu = 0, \tag{2.99}$$

where ∇_μ is the covariant derivative defined by

$$\nabla_\nu\,\xi_\mu = \frac{\partial \xi_\mu}{\partial x^\nu} - \xi_\lambda\,\Gamma^\lambda_{\mu\nu}, \tag{2.100}$$

[12] The space is said to be **homogeneous** if for two different points in the space, there is an isometry of the metric that takes the first one into the second one.

[13] Let us consider a timelike tangent vector **u** and two orthogonal spacelike tangent vectors v_1 and v_2 at every point p in the space. If there is an isometry of the metric such that p and **u** are unchanged even though v_1 is rotated into v_2, the space is said to be **isotropic**.

being $\Gamma^{\lambda}_{\mu\nu}$ the Christoffel symbol defined in terms the metric

$$\Gamma^{\lambda}_{\mu\nu}\ g_{\lambda\alpha} = \Gamma_{\alpha\mu\nu} = \frac{1}{2}\left(\frac{\partial g_{\mu\alpha}}{\partial x^{\nu}} + \frac{\partial g_{\alpha\nu}}{\partial x^{\mu}} - \frac{\partial g_{\mu\nu}}{\partial x^{\alpha}}\right). \tag{2.101}$$

Equation (2.99) is a **Killing equation** and actually all ξ_{μ} that satisfy this equation, presented on the infinitesimal transformation, are the Killing Vectors. They define the isometries of the metric we are considering. Each isometry, such as translation or rotation, has its respective associated Killing vectors. Finding the Killing vectors means finding all isometries of a particular metric.

Killing vectors exhibit a closure property, that is, a linear combination of Killing vector will be another Killing vector. If we have a Killing vector at a specific point X and its covariant derivative at the same point, we can define a Killing vector at any point Y.

One might ask about the maximum number of linearly-independent Killing vectors in a N-dimensional space. After performing a Taylor expansion we can check that the Killing vector has N independent components. From the anti-symmetry of the Killing equation there are $\frac{N(N-1)}{2}$ independent components and adding all of them, we get $\frac{N(N+1)}{2}$ independent components.

A space that has $\frac{N(N+1)}{2}$ Killing vectors for its metric is known as a maximally symmetric space. And it happens to AdS space, because for the 5 dimensions of the AdS space we get precisely 15 Killing Vector. And the same happens to the inner space S^5 (BOSCHI-FILHO; BRAGA, 2004).

2.4.4.2 Symmetries of $\mathcal{N} = 4$ SYM

The conformal field theory considered by the conjecture has a $\mathcal{N} = 4$ Supersymmetric Yang-Mills as its framework. This theory has two classes of symmetries. The first one comes from the 4 Weyl supercharges represented by $\mathcal{N} = 4$. This part exhibits a spectrum that forms a symmetry defined by the SU(4) group. Since the SU(N) has N^2-1 generators, the SU(4) presents 15 generators. The one vector and the sets of scalars and fermions are rotated among each other by a supersymmetric transformation. The second class comes from the set of field transformations. They are also 15. We have 4 generators for all translations on the spacetime, 4 generators for special conformal transformations, 1 for scale transformation (dilatation) and 6 Lorentz generators being 3 for rotations e the last 3 for boosts.

Summarizing one can say that the 15 isometries of the space time metric AdS_5 are related to the 15 generators of the field transformations (the conformal Lie Algebra) whereas the 15 isometries of the inner space (S^5) are related with all 15 generators for the supersymmetry.

2.5 Approaches for holographic models

When Maldacena presented the gauge/gravity duality, he was considering a mapping process between two conformal theories. If we suppose the duality exists, one can try to apply to non-conformal theories. One of them could be Quantum Chromodynamics (QCD).

We actually know that QCD does not exhibit conformal invariance. In other words, the theory behaves differently if we compare the high and low energy scales. For example:

at high energy scale, QCD promotes the asymptotic freedom, where we can consider the theory as free. Whereas at low energy scale, QCD shows confinement, which explains the fact that quarks and gluons are bounded together and as you try to separate them, the strong force becomes much stronger.

Conformal invariance is also broken because QCD has a natural scale (~ 0.3 GeV). If we want to construct a model to mimic QCD by using AdS/CFT conjecture, one could try to build the "AdS/QCD" duality by imposing the conformal invariance breakdown on the gravitational side, that is, on the AdS part.

There are two possibilities to approach the gauge/gravity duality in that way.

The first one starts considering the features of the theory we want to describe by an effective 5D theory with phenomenological approach. That is the Bottom-Up approach. The second one comes from a 10D string theory (usually the type IIB string theory) and the brane configuration is created to mimic the gauge theory, such as QCD. That is the Top-Down approach, which, here, we focus on the D3/D7 model (KARCH; KATZ, 2002).

On the following, we will present these two different approaches with examples.

2.5.1 Bottom Up

The Bottom-Up approach has a phenomenological construction. There are many models created to simulate QCD on different ways. Below, we present two of the most prominent models known as the *hard wall* and *soft wall*.

The Hard Wall

The Hard Wall model, proposed by Polchinski and Strassler (POLCHINSKI; STRASSLER, 2002), is the simplest way of breaking the conformal invariance of the AdS metric. The idea is to consider one brane at $z = z_0$ and another one at $z = z_m$, called the UV and IR brane, respectively. The brane that is located at the IR part can promote a *cut-off* in space. It exists for two reasons: mimicking the confinement and introducing a scale

$$z_m = \Lambda_{QCD}^{-1}. \tag{2.102}$$

Physically, it represents that the propagating wave function must go to zero at this wall, that is, it works as an infinite potential well in usual Quantum Mechanics. This happens because at $z = z_m$ the space ends.

The Hard Wall can describe several features of QCD, such as form factors, effective coupling constants and correlation functions. But the Regge trajectories have a quadratic form (non-linear), differently of what is expected.

The Soft Wall

The Soft Wall model, proposed by Karch, Katz, Son and Stephanov (KARCH *et al.*, 2006), also intend to break conformal invariance, but in a different way. In this model, the conformal invariance breaking comes from the introduction of a scalar field $\phi(z)$, the dilaton field, which depends on the holographic coordinate z. On the string theory perspective, the dilaton is the one-particle state that comes from a standard decomposition of the closed string sector.

Whereas the AdS_5 geometry does not suffer any change, the dilaton background field is responsible for breaking conformal symmetry. One can construct the following effective gravity dual in AdS_d space

$$S = \int d^d x\, e^{-2\Phi(z)} \sqrt{-g}\, \mathcal{L}_{grav} + \int d^d x\, e^{-\Phi(z)} \sqrt{-g}\, \mathcal{L}_{matter} + \dots . \tag{2.103}$$

The dilaton field is also responsible for modifying the equation of motion and it will modify all the results we could obtain from this action, such as form factors, correlation functions and meson mass spectra.

If we generalize the definition of the dilaton field, one could write

$$\Phi(z) = (\mu\, z)^{\nu} \tag{2.104}$$

After setting for simplicity $\mu = \Lambda_{QCD}$, one can get after some calculations

$$m_n^2 \sim n^{2-\frac{2}{\nu}}, \tag{2.105}$$

where the case $\nu = 2$ represents the linear Regge trajectories. It is important to highlight that the combination AdS with dilation is not a solution of the Einstein equation. Indeed, there are dynamical models that consider the back-reaction effect of the dilaton on the metric (GURSOY; KIRITSIS, 2008; PAULA *et al.*, 2009). In particular, Ref. (PAULA *et al.*, 2009) presents a model that is a solution of the Einstein–Dilaton equations, reproduces the linear Regge trajectories, and exhibits confinement according to the Wilson loop criterion (area law).

2.5.2 Top Down

There are several models of Top Down approach. One of the most famous is the Witten-Sakai-Sugimoto model where a system with D4-D8 branes configuration is used to map the duality from a type-IIA superstring theory [14]. Beyond that, we have these important type-IIB solutions such as Maldacena-Nunez (MALDACENA; NUNEZ, 2001) and Klebanov-Strassler (KLEBANOV; STRASSLER, 2000).

In this work, we are going to discuss the construction of the Dp-Dq Top Down model from a brane configuration. Later, it will be important to perform a series of calculations that will be useful in building the equation of states, the TOV and many phenomenological aspects that represent the observables.

2.6 Summary

This chapter provided a comprehensive overview of the AdS/CFT correspondence and its relevance as a framework for studying strongly coupled gauge theories such as QCD. We began by exploring the conceptual basis of the duality, including the role of extra dimensions, the 't Hooft limit, and the motivations for using Anti-de Sitter space. Key elements of string theory and D-brane physics were introduced to support the holographic construction.

In particular, we focused on the main features of QCD, emphasizing asymptotic freedom, the running of the coupling constant, and the non-perturbative phenomena

[14] On the supersymmetric perspective, there is one way to differeciate type IIA from type IIB string theory. It is about the number of spatial dimensions of the branes. On type IIA string theory, we just have even numbers to keep the supersymmetry: D0, D2, D4, D6, D8. On type IIB string theory, we always have configurations with odd numbers: D1, D3, D5, D7. Therefore, the D4-D8 WSS is a supersymmetric system and the model D3-D7, that we will discuss in this work, is another supersymmetric example. See the details on (SEN, 2000).

of confinement and chiral symmetry breaking. These aspects were then connected to holographic techniques, highlighting how effective models attempt to mimic QCD in the strong coupling regime.

We closed the chapter by comparing bottom-up and top-down holographic approaches, setting the stage for their application in modeling physical systems. The next chapter will build upon these foundations to address compact astrophysical objects — such as neutron stars — where the physics of strongly interacting matter plays a critical role.

3 Compact Objects

Understanding compact stars requires first revisiting the broader picture of stellar evolution. Stars are not static entities; they undergo complex evolutionary processes driven by the balance between two competing forces: gravity and internal pressure. This balance is what defines their structure and determines their fate.

Stars begin their life in giant molecular clouds — cold, dense regions filled with gas and dust. Under the influence of gravity, these regions collapse, forming protostars, the earliest stage in the stellar lifecycle. As the core temperature increases, hydrogen fusion ignites, and the star enters the main sequence phase, where it spends most of its life converting hydrogen into helium through nuclear fusion. This phase is characterized by a stable equilibrium between gravitational collapse and radiation pressure from nuclear burning (SHAPIRO; TEUKOLSKY, 2004).

The Hertzsprung–Russell (H–R) diagram is a key tool in visualizing a star's evolutionary path (FILHO; SARAIVA, 2017). Figure 3.1 plots stellar luminosity against surface temperature. Main sequence stars form a distinct band from hot, luminous blue stars to cooler, dimmer red stars. As a star exhausts its hydrogen fuel in its core, it evolves off the main sequence and begins fusing heavier elements, entering the old age phase.

The course of evolution from this point depends critically on the star's mass. Low- and

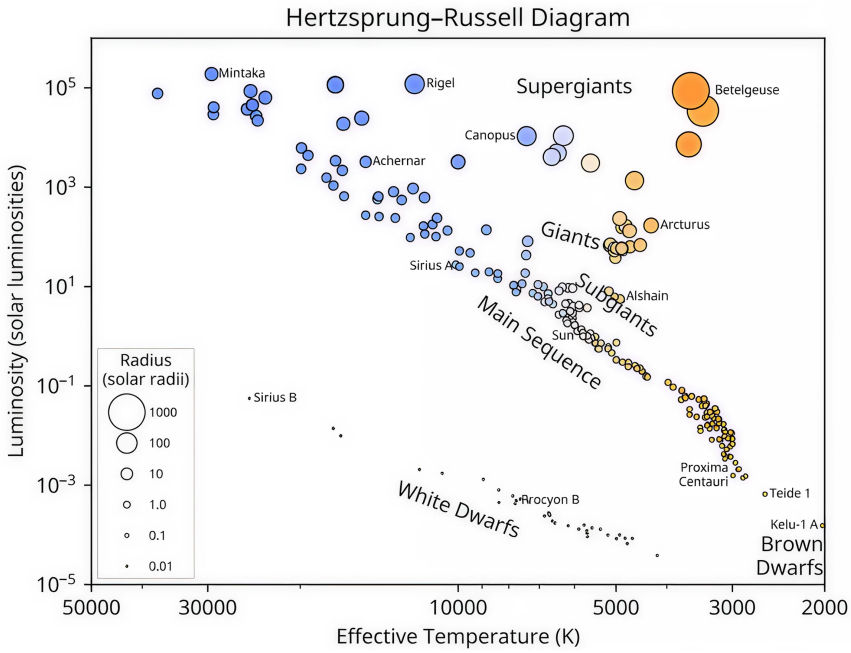

FIGURE 3.1 – H-R diagram representation showing some known stars. Extracted from https://www.astro4edu.org/media/diagrams/pdf/hr_diagram_en.pdf.

intermediate-mass stars (up to $\sim 8\,M_\odot$) evolve into red giants and later shed their outer layers, forming a planetary nebula. The core that remains is a white dwarf, supported by electron degeneracy pressure, and composed mostly of carbon and oxygen.

Massive stars ($\gtrsim 8\,M_\odot$) continue fusion beyond helium, producing successively heavier elements: carbon, neon, oxygen, and silicon. Ultimately, the fusion process produces iron, an element that cannot release energy via fusion due to its maximal binding energy per nucleon. When the iron core becomes too massive (typically above $\sim 1.4\,M_\odot$), it collapses catastrophically in a supernova explosion — a violent and luminous event that marks the end of stellar life and the beginning of a compact remnant (WOOSLEY *et al.*, 2002).

The remnant depends on the mass of the progenitor core after the explosion

- White dwarfs result from low-mass cores ($\lesssim 1.4\,M_\odot$), stabilized by electron degen-

eracy pressure.

- Neutron stars form when the collapsing core exceeds the Chandrasekhar limit [1] but remains below the Tolman–Oppenheimer–Volkoff (TOV) limit (typically $\lesssim 2.5\,M_\odot$), with stabilization now provided by neutron degeneracy and strong nuclear forces.

- Black holes emerge when even these pressures fail to halt collapse, and gravity dominates entirely, curving spacetime to the point of forming a singularity (ÖZEL; FREIRE, 2016).

Throughout this evolution, the remnants that emerge — white dwarfs, neutron stars, and black holes — are known as compact objects. Due to their extreme densities, temperatures, and gravitational fields, these objects serve as natural laboratories for testing the frontiers of fundamental physics. Among them, neutron stars are particularly valuable, as they allow us to probe the behavior of matter under conditions inaccessible in terrestrial experiments.

Their interiors may reach densities several times greater than the nuclear saturation density, potentially creating environments in which hadrons dissociate into their fundamental constituents: quarks. This possibility gives rise to exotic stellar configurations such as hybrid stars, which possess a quark core surrounded by hadronic matter, and quark stars, which are entirely composed of deconfined quark matter. These hypothetical stars open an exciting window into the study of QCD in the non-perturbative, strongly coupled regime at low energies.

In this chapter, we introduce the structure and composition of neutron stars. We will explore the conditions under which phase transitions in dense matter may occur, examine

[1] The Chandrasekhar limit is the maximum mass ($\sim$1.4 $M_\odot$) that a white dwarf can have before electron degeneracy pressure is no longer sufficient to prevent collapse (CHANDRASEKHAR, 1931).

the theoretical predictions and observational data related to mass-radius relations, and analyze the role of tidal deformability — a key observable in gravitational wave astronomy. These discussions will establish the necessary groundwork for investigating holographic models of dense nuclear matter in subsequent chapters.

3.1 Neutron stars

The idea of neutron stars began to take shape in the early 1930s, during a time of major discoveries in nuclear physics. In 1932, James Chadwick discovered the neutron — a neutral particle found inside atomic nuclei. Just one year earlier, physicist Lev Landau had proposed the existence of extremely dense stars that could behave like a single gigantic atomic nucleus. Although his explanation was not fully correct, his idea anticipated the basic concept of what we now call a neutron star.

A more complete and modern picture came in 1933, when Walter Baade and Fritz Zwicky suggested that certain stars could collapse into compact objects after a supernova explosion. They introduced the term "neutron star" and described it as being composed mostly of neutrons, with densities much higher than anything found in ordinary matter.

Today, neutron stars are understood as compact remnants of massive stars that have exploded as supernovae. They usually have masses between 1.1 and 2.3 $M_\odot$ [2], and radii between 10 and 14 kilometers. Their core densities can reach more than five times the nuclear saturation density, $\rho_0 \approx 2.8 \times 10^{14}$ g/cm^3. These stars are mainly composed of neutrons, but also contain protons, electrons, and muons. Some models predict the presence of more exotic particles, like hyperons or even deconfined quark matter. A special

[2] A neutron star with a mass of $2.35\,M_\odot$ was reported in (ROMANI *et al.*, 2022), representing one of the most massive pulsars observed to date.

type of neutron star,known as a pulsar, is a highly magnetized and rapidly rotating object that emits beams of electromagnetic radiation from its magnetic poles, observed as regular pulses due to its rotation.

From the outer surface to the deepest core, a neutron star reveals a thermodynamically layered structure, where each region plays a specific role in its cooling process and observable features.

The journey begins at the atmosphere — a thin layer approximately 1 cm thick (HAENSEL *et al.*, 2007) composed of ionized hydrogen, helium, and carbon (PIEKAREWICZ, 2022) with densities below 10^4 g/cm^3 — which, despite its low mass, critically shapes the thermal emission (ÖZEL; FREIRE, 2016) and the spectrum captured by telescopes (ZAVLIN; PAVLOV, 2002).

Right below lies the thermal envelope, composed of light ions surrounded by partially degenerate electrons (ÖZEL; FREIRE, 2016). With densities ranging from 10^4 to 10^{10} g/cm^3, this region acts like a thermal insulator, regulating heat flow from deeper layers and influencing the cooling behavior of the star (BEZNOGOV; YAKOVLEV, 2016).

The next layer is the crust. The outer crust consists of neutron-rich nuclei embedded in a sea of degenerate electrons, forming a crystalline lattice that supports mechanical stresses (PIEKAREWICZ, 2022). As the density increases — reaching up to 4×10^{11} g/cm^3 (SHAPIRO; TEUKOLSKY, 2004) — the inner crust emerges. Here, free neutrons begin to "drip" out of nuclei, forming a superfluid that coexists with the nuclear lattice. This environment enables sudden rotational shifts known as *glitches*, observed in pulsars and often explained by vortex unpinning in the neutron superfluid (BAYM *et al.*, 2017) (CHAMEL, 2017), though other mechanisms have been suggested.

Approaching nuclear saturation density ($\sim 10^{14}$ g/cm^3), the structure transitions into the so-called nuclear pasta phase. It is represented in figure 3.2.

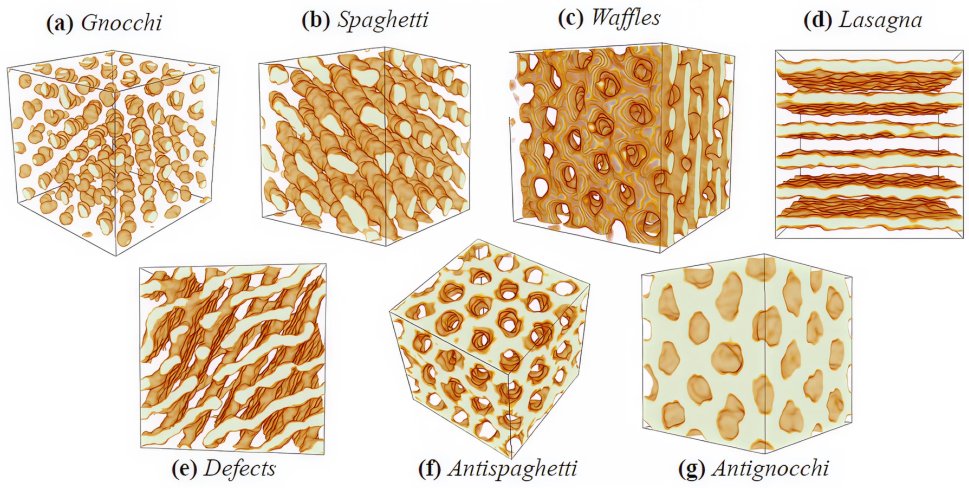

FIGURE 3.2 – Nuclear pasta: topological configurations. Extracted from (CAPLAN; HOROWITZ, 2017).

Due to a balance between nuclear attraction and Coulomb repulsion — a phenomenon known as *Coulomb frustration* — matter organizes into exotic geometries nicknamed "spaghetti", "lasagna", and "gnocchi" (HOROWITZ *et al.*, 2004; PIEKAREWICZ, 2022). For this reason, it is referred to as the pasta phase. These topological phases affect key transport properties like thermal conductivity and neutrino opacity (HOROWITZ; BERRY, 2008).

Deeper still is the outer core, where densities rise to around 5×10^{14} g/cm^3 (HAENSEL *et al.*, 2007). In this region, matter behaves as a degenerate Fermi liquid of neutrons, protons, electrons, and muons (PIEKAREWICZ, 2022). Neutrons form a superfluid[3] and protons a superconductor (SHAPIRO; TEUKOLSKY, 2004). This environment enables rapid cooling via the URCA process — cycles of beta decay and electron capture that emit neutrinos (HOROWITZ; PIEKAREWICZ, 2002).

Inside the inner core of neutron stars, which is believed to reach densities close to or

[3]The $^3P_2$ channel represents anisotropic pairing between neutrons at high densities, while the $^1S_0$ channel describes isotropic proton pairing at lower densities.

exceeding nuclear saturation ($> 5 \times 10^{14}$ g/cm^3) (HAENSEL *et al.*, 2007), many theoretical models predict the appearance of new degrees of freedom — such as hyperons[4] (GLENDENNING; MOSZKOWSKI, 1991; BOMBACI *et al.*, 2008; DEXHEIMER; SCHRAMM, 2008) or deconfined quark matter (BODMER, 1971; WITTEN, 1984; LATTIMER; PRAKASH, 2007) — giving rise to exotic phases.

Among the most compelling possibilities are the color-superconducting states known as *2SC* and *CFL*[5] (ALFORD *et al.*, 1998). If such phases occur in nature, they may lead to a distinct class of compact stars — the so-called third family — potentially identifiable by a discontinuity in the mass–radius relation (HAENSEL *et al.*, 2007).

To synthesize the layered structure discussed above, a schematic cross section of a neutron star is shown in figure 3.3, highlighting the distinct physical regimes and compositions from the outer atmosphere down to the innermost core.

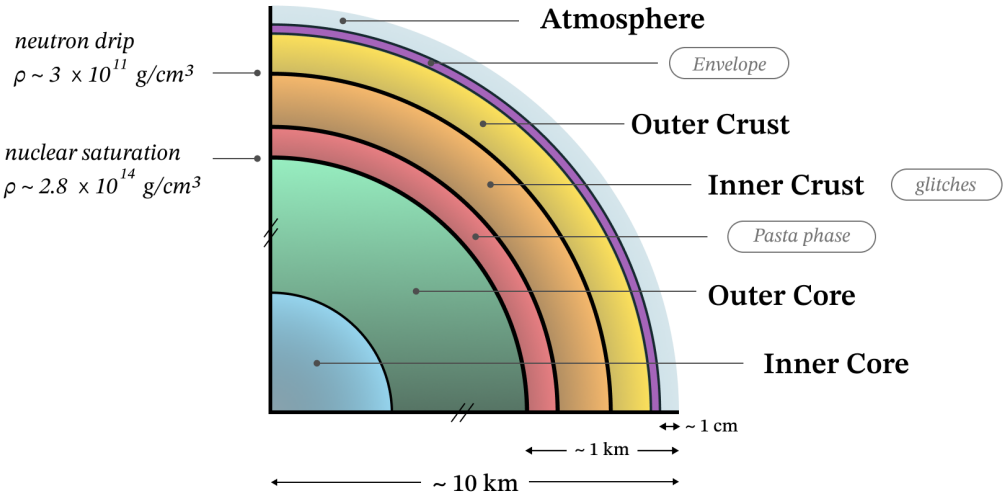

FIGURE 3.3 – The cross section of a neutron star. Illustration out of scale.

[4]Hyperons are baryons containing at least one strange quark, such as the Λ, Σ, and Ξ particles. They are more massive than protons and neutrons and may appear in the dense core of neutron stars where the Fermi energy becomes high enough to favor their formation.

[5]The 2SC phase features pairing among u and d quarks in specific color channels, while CFL involves all flavors and colors, forming a more symmetric and energetically favorable phase.

Among the many open questions is the possibility of deconfinement in the deepest core, where transitions from hadronic to quark matter may occur. These transitions lie at the heart of the next section, where we explore the physics of phase transitions in dense nuclear matter.

3.2 Phase transitions in dense matter

Understanding phase transitions in dense matter is crucial for modeling the internal composition of neutron stars and predicting observable signatures of exotic phases in compact objects.

At the heart of the study of these transitions lies the QCD phase diagram — a theoretical construct that organizes the different phases of strongly interacting matter as a function of temperature T and baryon chemical potential μ_B. See figure 3.4 in which the baryon chemical potential μ_B is represented by μ. The region of high temperature and low baryon density — where quark deconfinement and chiral symmetry restoration are expected to occur — has been successfully explored through lattice QCD simulations and is experimentally probed in heavy-ion collisions.

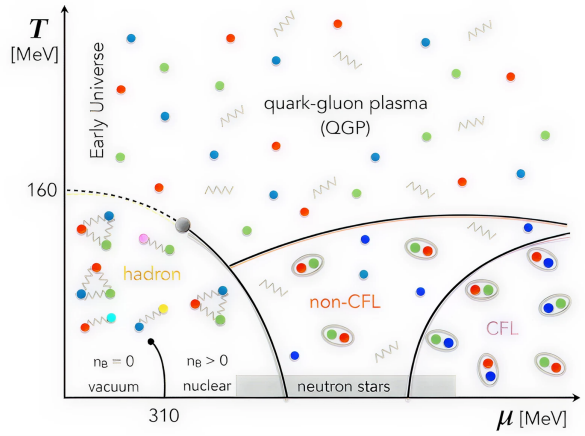

FIGURE 3.4 – QCD phase diagram extracted from (RODRIGUEZ *et al.*, 2021).

In contrast, the low-temperature, high-density region — relevant for the physics of compact stars — remains largely inaccessible to first-principles calculations due to the sign problem (FORCRAND, 2009). The so-called *sign problem* arises when attempting to apply Monte Carlo methods to simulate QCD at finite baryon chemical potential. In this regime — particularly relevant when the baryon density is high, as in compact stars — the fermion determinant in the QCD partition function becomes complex, which invalidates its interpretation as a probability weight. Since probabilities must be real and positive, the complex phase introduces severe cancellations between contributions, making numerical convergence extremely difficult. As a result, lattice QCD — a powerful non-perturbative tool at zero or small chemical potential — becomes ineffective in this region of the phase diagram. Despite ongoing efforts using complex Langevin dynamics (AARTS *et al.*, 2012), reweighting techniques (FODOR; KATZ, 2002), and Lefschetz thimble methods (CRISTOFORETTI *et al.*, 2012), a robust and general solution remains elusive.

Despite this limitation, effective models suggest that, at low T and large μ_B, QCD matter undergoes a first-order phase transition[6] from hadronic matter to deconfined quark matter. This transition is typically associated with a discontinuity in the energy density, a latent heat release, and the possibility of a mixed phase region. The endpoint of this first-order line is expected to be a critical point — the so-called QCD critical point — which marks the onset of a smooth crossover transition for higher temperatures.

In the context of compact stars, we are particularly interested in the cold and dense sector of this diagram, where such a phase transition might occur naturally in the core of neutron stars (or hybrid stars, as we will see in Chapter (6)). Matter inside neutron stars

[6]A first-order phase transition is characterized by a discontinuity in the first derivative of the thermodynamic potential (e.g., entropy or volume), often accompanied by latent heat and phase coexistence. In contrast, a second-order (or continuous) phase transition features continuous first derivatives but discontinuous or divergent second derivatives, such as specific heat or susceptibility. Second-order transitions do not involve latent heat. (HAENSEL *et al.*, 2007)

is considered to be cold in the sense that its thermal energy is negligible compared to its Fermi energy. Typical core temperatures ($T \sim 10^8$–10^9 K) correspond to a few tenths of MeV, which is small relative to the Fermi energy ($E_F \sim 10^2$ MeV) of degenerate baryons (HAENSEL *et al.*, 2007). Therefore, thermal effects play a minor role in the equation of state. This justifies modeling the star's interior as cold, strongly interacting matter. As a result, compact stars probe a region of the QCD phase diagram characterized by high baryon density and low temperature, making them unique astrophysical laboratories for exploring phenomena inaccessible to heavy-ion collisions, which probe high temperatures but low densities.

In addition to the nature of the phase transition, an important classification arises when one considers the dynamic behavior of the interface between hadronic matter and quark matter under perturbations. This classification distinguishes between **rapid** and **slow** phase transitions — a distinction that emerges from the comparison between two characteristic timescales: the nucleation timescale (i.e., the time required to convert matter from one phase to the other) and the timescale of the star's perturbations (typically associated with its radial oscillation period). This latter timescale is of the order of $\tau_{\rm osc} = 2\pi\omega_0^{-1}$, with ω_0 represents the oscillation natural frequency, that for a typical neutron star, one has $\tau_{\rm osc} \sim 1$ ms (LUGONES *et al.*, 2023).

Slow transitions occur when the nucleation time is much longer than the period of oscillation. In this case, elements of volume near the phase interface do not convert from one phase to another in response to local pressure variations. Instead, they co-move with the perturbation, expanding and compressing as a unified element. Because there is no phase conversion, there is no mass transfer across the interface. *Rapid transitions*, on the other hand, assume that the phase conversion is instantaneous compared to the timescale

of perturbation. As a result, elements of volume at the interface can change their nature from one phase to another during compression or rarefaction. This enables mass transfer between the two phases (PEREIRA *et al.*, 2018).

This behavior is strongly influenced by the microphysics of the transition, particularly by the surface tension between the hadronic and quark phases. As shown in (PALHARES; FRAGA, 2010), the surface tension σ plays a central role in defining the energy barrier for nucleation. High values of σ inhibit rapid conversion and favor the slow-transition regime by effectively delaying the nucleation process, which becomes comparable to or longer than the characteristic timescale of stellar oscillations. In this context, one may interpret a large surface tension as resembling a stiffer or more rigid phase boundary, hindering mass transfer between phases. Remarkably, even radial perturbations on the order of 1 cm — seemingly small — represent significant distortions in a neutron star due to its extreme compactness (HØYE, 1999).

To model first-order phase transitions inside compact stars, it is essential to apply thermodynamic criteria that govern the equilibrium between hadronic and quark matter phases. Two widely used approaches are the **Maxwell** and **Gibbs constructions**, each reflecting different assumptions about local properties and the nature of the transition interface.

Maxwell construction. This scheme assumes *local charge neutrality* — each phase must be electrically neutral independently — and imposes a sharp transition surface between the two phases (SPINELLA *et al.*, 2020) (CONSTANTINOU *et al.*, 2023). As a result, the surface tension is considered to be extremely high ($\sigma \to \infty$), effectively preventing the formation of intermediate structures. The transition is isobaric: it occurs at a fixed pressure and baryon chemical potential (GLENDENNING, 2000) (CONTRERA *et al.*, 2017).

Only a single conserved charge (usually the baryon number) is considered, and the electron chemical potential μ_e exhibits a discontinuity across the interface. No mass conversion occurs during radial oscillations near the transition interface. The corresponding equilibrium conditions can be written as

$$P_H(\mu_B) = P_Q(\mu_B), \quad \mu_B^H = \mu_B^Q, \quad \mu_e^H \neq \mu_e^Q. \tag{3.1}$$

Figure 1 in (LUGONES; GRUNFELD, 2021) provides a cross-sectional view of a hybrid star, illustrating the sharp phase transition between hadronic matter and deconfined quark matter — a feature that is characteristic of the Maxwell construction.

Gibbs construction. In contrast, the Gibbs approach assumes *global charge neutrality*, allowing the electric charge to be redistributed across the two phases (CONSTANTINOU *et al.*, 2023). The surface tension is effectively zero ($\sigma \to 0$), enabling the formation of spatially extended mixed phases, with soft transitions between pure hadronic and pure quark matter (SPINELLA *et al.*, 2020). Pressure varies continuously through the transition, and each phase has its own chemical potential for the conserved charges (CONTRERA *et al.*, 2017). The electron chemical potential remains continuous. Mass conversion occurs dynamically during perturbations. The equilibrium conditions for the Gibbs construction are expressed as

$$P_H(\mu_B, \mu_e) = P_Q(\mu_B, \mu_e), \quad \mu_B^H = \mu_B^Q, \quad \mu_e^H = \mu_e^Q. \tag{3.2}$$

In the Gibbs construction, phase transition is modeled as a continuous and spatially extended mixed phase, where both hadronic and quark matter coexist. The volume

fraction of quark matter is denoted by χ (with $0 \leq \chi \leq 1$), and the global conservation of electric charge and baryon number must be satisfied. Total charge density Q and baryon density n_B in the mixed phase are given by (HAENSEL *et al.*, 2007)

$$Q = \chi\, q_Q + (1 - \chi)\, q_H + q_e = 0, \tag{3.3}$$

$$n_B = \chi\, n_Q + (1 - \chi)\, n_H, \tag{3.4}$$

where q_Q and q_H are the electric charge densities of quark and hadronic matter, respectively, and q_e is the charge density of electrons. Similarly, n_Q and n_H denote the baryon number densities of each phase.

When $\chi = 0$, the system consists entirely of hadronic matter, and the quark contribution vanishes. Conversely, when $\chi = 1$, the system is composed purely of deconfined quark matter. In the intermediate regime ($0 < \chi < 1$), the two phases coexist [7], and χ smoothly interpolates between them, regulating the composition and ensuring global charge neutrality.

See figure 2 of (LUGONES; GRUNFELD, 2021), which presents a cross-sectional view of a hybrid star, highlighting the mixed phase transition between hadronic matter and deconfined quark matter — a feature that is characteristic of the Gibbs construction.

It is important to note that some studies argue that surface tension values near the critical threshold $\sigma_{\text{crit}} = 60$ MeV/fm^2 (VOSKRESENSKY *et al.*, 2003) characterize the transition as sharp, thereby favoring a Maxwell construction. Consequently, any surface tension value ranging from 0 to 60 MeV/fm^2 would define the transition through the Gibbs construction.

[7] In this coexistence region — the so-called mixed phase — matter may enter a regime known as the *nuclear pasta phase*, as previously discussed.

In practice, the necessary and sufficient condition for establishing a Maxwell construction can be visualized in a pressure versus chemical potential diagram (CONTRERA *et al.*, 2017). If the hybrid equation of state is built such that the curve describing the hadronic sector intersects the one representing the quark phase, a first-order phase transition will occur precisely at this intersection point. In contrast, for the Gibbs construction, such a crossing is not sufficient. It is also required that global charge conservation be satisfied so that pressure, chemical potential, and energy density vary monotonically throughout the phase transition region.

Although certain scenarios favor *rapid phase transitions*—such as those obeying the *Seidov limit* [8], where a sufficiently large energy density discontinuity between phases enables an almost instantaneous conversion—this is not the regime adopted in the present work. Rapid transitions are particularly relevant from an exoenergetic perspective, as they involve the release of significant latent heat, which can influence stellar stability during and after the conversion process.

[8]The *Seidov limit* (SEIDOV, 1971) establishes a criterion for the maximum energy density discontinuity $\Delta\varepsilon$ that can occur during a rapid first-order phase transition (PEREIRA *et al.*, 2018) in a neutron star without compromising its stability. This limit applies to transitions involving a small core of exotic matter (e.g., quark matter) and is derived within the framework of General Relativity. It quantifies how much excess energy the new phase can introduce without triggering gravitational collapse. The discontinuity is expressed as (SEIDOV, 1971)

$$\Delta\varepsilon = \varepsilon_Q - \varepsilon_H = \varepsilon_H \left(\frac{1}{2} + \frac{3}{2} \frac{P_H}{\varepsilon_H} \right), \tag{3.5}$$

where ε_H and P_H refer to the energy density and pressure of the hadronic phase at the transition interface, and ε_Q is the energy density of the quark (or exotic) phase. This condition is particularly relevant in the presence of latent heat release, which can be evaluated from the energy per nucleon difference (LOPE-OTER; LLANES-ESTRADA, 2022)

$$\Delta E = \frac{P_H}{n_E n_H}(n_E - n_H), \tag{3.6}$$

where n_E and n_H are the baryon densities in the exotic and hadronic phases, respectively. The latent heat per nucleon, $L = \Delta E/M_N$, normalized by the neutron mass M_N, serves as a thermodynamic signature of the phase transition strength. It is important to note that $\Delta\varepsilon$ is a *macroscopic* quantity, expressing the jump in energy density per unit volume, while ΔE is a *microscopic* quantity, corresponding to the latent heat per baryon. A simple connection between them can be expressed as $\Delta E \approx \Delta\varepsilon/n_B$, where n_B is the baryon number density.

Instead, we focus on the *slow-transition regime*, characterized by a well-defined interface between the phases, modeled through the **Maxwell construction**. This choice is supported by studies such as (PALHARES; FRAGA, 2010), which demonstrate that increasing the surface tension at the interface drastically suppresses the formation of a mixed phase and substantially raises the nucleation time. In practical terms, one may interpret this behavior as producing a sharper and more rigid boundary, hindering mass transfer between the two phases. That is, the transition becomes *spatially abrupt* but *temporally slow*, suppressing phase coexistence and favoring a scenario in which the conversion proceeds without intermediate configurations—consistent with the assumptions behind the Maxwell construction.

There are also theoretical scenarios in which hybrid stars may undergo more than one phase transition as a function of increasing density. For instance, some models admit the presence of two successive first-order phase transitions, which lead to the construction of a multi-layered equation of state defined by distinct regions governed by different forms of matter (LI *et al.*, 2023) (RAU; SEDRAKIAN, 2023). These models are usually formulated by partitioning the EoS into distinct density intervals, each described by a specific theoretical framework tailored to hadronic, exotic, or quark phases. Such approaches require selecting a suitable description for each matter sector and matching them at thermodynamically consistent boundaries, as discussed previously.

While these approaches allow for more intricate internal structures, in this work we focus on a single first-order phase transition between hadronic and quark matter to investigate hybrid star properties using this framework as the basis for our holographic hybrid model. Both the model and our resulting analysis will be presented in Chapter (6), where we adopt the Maxwell construction under the assumption of a slow phase transition

regime.

3.3 Mass-radius relations

The mass–radius (M–R) diagram is a fundamental tool for investigating the equilibrium and stability properties of compact stars. It establishes a relationship between the gravitational mass M and the radius R of a star for a given equation of state (EoS), encoding both microphysical interactions and general relativistic effects. Each point on the M–R curve corresponds to a stellar configuration that satisfies the Tolman–Oppenheimer–Volkoff (TOV) equations of hydrostatic equilibrium, which were explicitly derived in Appendix (**E**)

$$\frac{dM_r}{dr} = 4\pi r^2 \rho(r), \tag{3.7}$$

$$\frac{dP}{dr} = -\frac{GM_r\rho}{r^2}\left(1+\frac{4\pi r^3 P}{M_r c^2}\right)\left(1+\frac{P}{\rho c^2}\right)\left(1-\frac{2GM_r}{rc^2}\right)^{-1}. \tag{3.8}$$

In these equations, $P(r)$ is the pressure, $\rho(r)$ is the mass-energy density, and M_r is the enclosed gravitational mass at radius r. To obtain the M–R curve numerically, the TOV equations are integrated from the center ($r = 0$), where

$$M_r(0) = 0, \quad P(0) = P_c, \tag{3.9}$$

up to the surface $r = R$, where the pressure drops to zero (HAENSEL *et al.*, 2007)

$$P(R) = 0, \quad M_r(R) = M. \tag{3.10}$$

Here, R is the stellar radius, and M is the total gravitational mass of the star. The central pressure P_c is varied to produce a full sequence of solutions that collectively form the M–R curve.[9]

Although commonly used to study neutron stars, the M–R diagram also finds application in describing other astrophysical objects such as white dwarfs, brown dwarfs, and massive planets. However, compact stars inhabit a distinct region of the diagram due to their ultra-dense cores and relativistic structure. The behavior of the M–R curve depends sensitively on the stiffness of the EoS: a stiffer EoS tends to produce stars with larger radii and higher maximum masses, while a softer EoS yields more compact configurations (RILEY *et al.*, 2021).

The M-R diagram also reflects the existence of three distinct families of compact objects [10]. The first family corresponds to white dwarfs, which are supported against gravitational collapse by electron degeneracy pressure and exhibit densities ranging from 10^6 to 10^9 g/cm^3. Neutron stars, in turn, belong to the second family and occupy the high-density regime above 10^{14} g/cm^3, reaching up to 10^{15} g/cm^3. The third family — where hybrid stars are located — emerges as a second stable branch beyond the white dwarf and neutron star sequences. It is worth noting that within the intermediate density range from 10^9 to 10^{14} g/cm^3, no stable stellar configurations are expected to exist (SCHERTLER *et al.*, 2000).

From a dynamical perspective, each stellar configuration along the M–R curve can be analyzed via its radial perturbation spectrum. These perturbations form a discrete set of

[9]The standard boundary condition $P(R) = 0$ is a practical approximation that simplifies the numerical treatment. In the present study of quark and hybrid stars, we will adopt this condition as our surface boundary. Physically, it implies that the atmospheric pressure outside the star is negligible, although in reality the atmosphere of a neutron star exerts a nonzero, albeit tiny, pressure (HAENSEL *et al.*, 2007).

[10]In contrast, objects such as massive planets lie in the region of large radii and low masses — corresponding to low-density configurations — near the beginning of the white dwarf branch on the curve in figure 15 of (SCHERTLER *et al.*, 2000).

eigenmodes described by the Sturm–Liouville problem (SHAPIRO; TEUKOLSKY, 2004)

$$\omega_0^2 < \omega_1^2 < \omega_2^2 < \ldots, \tag{3.11}$$

where ω_n^2 are the eigenfrequencies of radial oscillations. Stability requires that $\omega_0^2 > 0$. A mode becomes unstable when its corresponding $\omega_n^2 < 0$.

To determine the onset of instability, one may use two complementary criteria:

Static stability criterion

The **Harrison–Zel'dovich–Novikov (HZN)** (HARRISON *et al.*, 1965) (ZEL'DOVICH; NOVIKOV, 1971) criterion asserts that the star is stable if the gravitational mass increases with the central energy density ρ_c

$$\frac{dM}{d\rho_c} > 0. \tag{3.12}$$

This is a *necessary (but not sufficient) condition* for stability (SHAPIRO; TEUKOLSKY, 2004). When the derivative becomes negative, the configuration becomes unstable. However, this condition alone does not account for how many modes are unstable.

BTM dynamical stability criterion

The **Bardeen–Thorne–Meltzer (BTM)** criterion (HARRISON *et al.*, 1965) (BARDEEN *et al.*, 1966) (MELTZER; THORNE, 1966) offers a geometric interpretation based on the properties of the M–R curve:

1. Each extremum (maximum or minimum) in $M(\rho_c)$ or $M(R)$ signals the gain or loss

of one unstable mode.

2. At each extremum of the M–R curve, one radial eigenmode changes stability. Specifically, at a maximum or minimum where $dR/d\rho_c < 0$, an *even* mode (such as ω_0^2, ω_2^2, ...) undergoes a sign change. Conversely, if $dR/d\rho_c > 0$, the mode that changes stability is *odd* (such as ω_1^2, ω_3^2, ...).

3. If the curve turns clockwise in the M–R plane, a previously unstable mode becomes stable; if it turns counterclockwise, stability is lost.

In the following chapters, we will explore the M–R diagram as we examine quark and hybrid star models. In particular, the static stability criterion will be applied in the context of stars with a single phase (such as quark stars), while the full dynamical stability analysis — involving radial oscillations and eigenfrequencies — will be carried out in the study of hybrid stars in Chapter (6).

3.4 Tidal deformability

Since the first observation of the gravitational waves made by LIGO (ABBOTT *et al.*, 2016), many researches used this new achievement to constrain theoretical astrophysical models. On October 2017 the LIGO/VIRGO collaboration announced the first-ever detection of gravitational waves created by two neutron stars which formed a binary system (ABBOTT *et al.*, 2017). This kind of system with at least two massive and dense bodies can provide a lot of considerable effects of deformations not only on the spacetime but in themselves. One of these effects is **tidal deformability** (DAMOUR; NAGAR, 2009).

If we consider a system with two massive bodies (for simplicity you can imagine the

Earth-Moon system) orbiting each other, we will check the tidal effects promoted by their proximity. That deformability on Earth, for example, exhibits the linear regime whereas if we considered a system with two neutron stars, the effects of the non-linear regime would be much more intense. This dynamical property can be defined as (LOGOTETA; BOMBACI, 2019) (ZHANG; HUANG, 2022)

$$\lambda = \frac{Q_{ij}}{\varepsilon_{ij}}, \tag{3.13}$$

where λ is the tidal deformability, Q_{ij} is the quadrupole momentum and ε_{ij} is the tidal field. The induced quadrupole moment, which mathematically comes from a multipoles expansion, is associated with the deformation of a spherically symmetrical object with respect to the flattening of the poles. The tidal field is the responsible for the deformation.

A small tidal deformability means that we are dealing with a very compact star and hard to be deformed. On the other hand, if we have a large tidal deformability, the star is less compact and easily deformable.

The tidal deformability is dimensionally expected to scale as the fifth power of the star radius, that is, R^5. It can be explained by checking that the quadrupole momentum has units of length cubed and the tidal field, at the newtonian limit, is defined as the second spatial derivative of the external field.

One can see the tidal deformability λ being defined in natural units by the gravitational Love number κ_2 [11] for a quadrupolar momentum (KATAGIRI *et al.*, 2024) (BINNINGTON;

[11] For realistic neutron stars $\kappa_2 \sim 0.05 - 0.15$ (*ABBOTT et al.*, 2017).

POISSON, 2009)

$$\lambda = \frac{2}{3}\kappa_2 \, R^5, \tag{3.14}$$

where κ_2 [12] is defined by (HINDERER, 2008)

$$\begin{aligned}
\kappa_2 = \frac{8\mathcal{C}^5}{5} \, & (1-2\mathcal{C})^2 \, \left(2+2\mathcal{C}(y_R-1)-y_R\right) \\
& \times\Big\{2\mathcal{C} \, \left(6-3y_R+3\mathcal{C} \, (5y_R-8)\right) \\
& +4\mathcal{C}^3 \left(13-11y_R+\mathcal{C} \, (3y_R-2)+2\mathcal{C}^2 \, (1+y_R)\right) \\
& +3 \, (1-2\mathcal{C})^2 \, \left(2-y_R+2\mathcal{C} \, (y_R-1)\right) \, \ln\left(1-2\mathcal{C}\right)\Big\}^{-1},
\end{aligned} \tag{3.15}$$

and $y_R = y(R)$ and $\mathcal{C}$ is the compactness, which will be presented shortly. The function $y(r)$ is a solution of the differential equation (PARISI *et al.*, 2021)

$$r \, (dy/dr) + y^2 + y \, F(r) + r^2 \, Q(r) = 0, \tag{3.16}$$

with

$$\begin{aligned}
F(r) &= \frac{1-4\pi r^2 \, (\varepsilon(r)-p(r))}{g(r)}, \\
Q(r) &= \frac{4\pi}{g(r)}\left(5\varepsilon(r)+9p(r)+\frac{\varepsilon(r)+p(r)}{v_s^2(r)}-\frac{6}{4\pi r^2}\right)-4\left(\frac{M(r)+4\pi r^3 p(r)}{r^2 g(r)}\right)^2, \\
g(r) &= 1-\frac{2M(r)}{r}.
\end{aligned} \tag{3.17}$$

[12] The tidal Love number k_2 corresponds to quadrupolar $l = 2$ deformations, which dominate the tidal response of compact stars. Lower-order modes are either non-physical or irrelevant for internal deformations: for $l = 0$ (monopole), there is no deformation — only a trivial change in mass-energy; for $l = 1$ (dipole), the effect results in a center-of-mass displacement without inducing internal strain. Therefore, the quadrupolar Love number k_2 is the primary quantity used in modeling tidal interactions in binary systems involving neutron stars. For further details, see (KATAGIRI *et al.*, 2024).

The quantity $v_s^2 = \frac{dp}{d\varepsilon}$ represents the squared speed of sound inside the star, reflecting how pressure responds to changes in energy density. To solve the differential equation associated with tidal deformations, it is necessary to impose a boundary condition at the stellar center, which is given by $y(0) = 2$ (See references (PARISI *et al.*, 2021) and (SOTANI; KUMAR, 2021) for further details). Therefore, once the equation of state (EoS) is specified, the system formed by the TOV equations and the tidal perturbation equation can be integrated together to determine the tidal Love number.

For convenience, it is common to find the tidal deformability on its dimensionless form. See a detailed discussion about the love number on (HINDERER, 2008). If we consider the natural unit system, where $G = c = 1$, we get:

$$[c] = 1 = [L\,T^{-1}] \quad \rightarrow \quad [L] = [T], \tag{3.18}$$

$$[G] = 1 = [M^{-1}\,L^3\,T^{-2}] \quad \rightarrow \quad [M] = [L^3\,T^{-2}] = [L]. \tag{3.19}$$

Therefore, since we have $\lambda \sim R^5$, from (3.19) the dimensionless form can be defined as it follows

$$\Lambda \equiv \frac{\lambda}{m_s^5}, \tag{3.20}$$

where m_s is the mass of the star. Replacing the definition for λ by using equation (3.14), it becomes (SOTANI; KUMAR, 2021)

$$\Lambda \;=\; \frac{2\,\kappa_2\,R^5}{3\,m_s^5} \;\equiv\; \frac{2}{3}\kappa_2\,\mathcal{C}^{-5}, \tag{3.21}$$

where $\mathcal{C} = \frac{m_s}{R}$ is the compactness. The minus sign on the exponent show us explicitly

the relation between the intensity of the tidal deformation with the ease of deforming the star gravitationally.

This quantity is very sensitive. Indeed, Λ can vary three orders of magnitude without considering the star rotation or other effects such as dynamical response of the tidal fields (CHATZIOANNOU, 2020).

The chirp mass parameter $\mathcal{M}$ is a function of the masses of two orbiting bodies that is related by the rate of energy transferred away through the gravitational waves. The definition resembles the reduced mass, and it is given by (ABBOTT *et al.*, 2017)

$$\mathcal{M} \equiv \left(\frac{m_1^3 \, m_2^3}{m_1 + m_2} \right)^{\frac{1}{5}} , \tag{3.22}$$

or using the total mass $M_T = m_1 + m_2$, the chirp mass can be defined in terms of the reduced mass $\mu = \frac{m_1 \, m_2}{m_1 + m_2}$

$$\mathcal{M} = \mu^{\frac{3}{5}} \, M_T^{\frac{2}{5}} . \tag{3.23}$$

This study of tidal deformability will be applied in Chapter (5), which is dedicated to quark stars. In the context of hybrid stars, however, we were not able to reproduce the observational data on tidal deformability.

3.5 Summary

In this chapter, we explored the key physical ingredients necessary to understand the structure and dynamics of compact stars. We began with a detailed discussion on

neutron stars, examining their internal composition, ranging from the outer atmosphere to the exotic possibilities in the inner core, such as hyperonic matter or deconfined quark phases. The concept of phase transitions in dense matter was then introduced, highlighting the challenges of modeling first-order transitions, the role of surface tension, and the distinction between slow and rapid conversions, with a particular focus on the Maxwell and Gibbs constructions.

Following this, we analyzed the mass–radius (M–R) diagram as a fundamental diagnostic tool for compact stars. We presented how to numerically obtain the M–R relation from the Tolman–Oppenheimer–Volkoff (TOV) equations and discussed the criteria for static and dynamic stability, focusing on the Harrison–Zeldovich–Novikov and Bardeen–Thorne–Meltzer (BTM) conditions. We showed how the shape of the M–R diagram reveals the appearance of different families of compact stars — from white dwarfs to neutron stars and, possibly, hybrid stars containing exotic matter.

Finally, we introduced the tidal deformability, an important observable for compact objects in binary systems. We discussed how the tidal Love number k_2 characterizes the star's response to external forces, the role of compactness, and how gravitational wave observations, particularly in events like GW170817, provide valuable constraints on the equation of state.

Overall, this chapter builds the theoretical foundation for the studies that follow, where we will construct and apply holographic models to explore the physics of strongly interacting quark matter inside compact stars.

In the next chapter, we will present the derivation of the D3–D7 holographic model (KARCH; KATZ, 2002), beginning with a general discussion of Dp–Dq brane configurations at zero temperature. This broader framework considers massive systems with finite charge

density and no external magnetic fields, as discussed in (ITSIOS *et al.*, 2016). The objective is to systematically build the holographic setup that leads to the equation of state for the D3–D7 model. This equation of state will be used to study quark stars in a holographic approach, and it will also model the quark matter sector inside hybrid stars, which will be explored in later chapters.

4 The D3-D7 holographic model

4.1 Introduction

One of the key challenges in using the AdS/CFT correspondence to study QCD-like theories is the inclusion of fields in the fundamental representation of the gauge group, such as quarks. The original duality between type IIB string theory on $\mathrm{AdS}_5 \times S^5$ and $\mathcal{N} = 4$ Super Yang–Mills theory describes only adjoint matter and exhibits exact conformal symmetry, making it unsuitable as a realistic model of strongly interacting matter.

A major development in this direction came with the proposal by Karch and Katz in 2002 (KARCH; KATZ, 2002), who introduced the idea of adding probe D7-branes into the background created by D3-branes. Their work showed that strings stretching between D3- and D7-branes give rise to fields in the fundamental representation of the gauge group on the D3-branes. This setup, now known as the D3–D7 model, realizes a holographic dual of $\mathcal{N} = 2$ Super Yang–Mills theory with N_f hypermultiplets in the fundamental representation, preserving supersymmetry while conformal invariance is broken.

By treating the D7-branes in the probe limit ($N_f \ll N_c$), their backreaction on the geometry is neglected, simplifying the gravitational side while still encoding the essential

physics of flavor. This framework has opened the door to a variety of non-perturbative studies, including meson spectroscopy, chiral symmetry, thermal phase transitions, and transport properties of flavored plasmas.

In this chapter, we present the detailed construction of the D3–D7 model from first principles (KARCH; O'BANNON, 2007) (KARCH *et al.*, 2009). We begin by outlining the general framework of Dp–Dq brane configurations (ITSIOS *et al.*, 2016), which provides the foundation for understanding how flavor is introduced in holography. We then focus on the D3–D7 system, describing the brane embedding, the resulting dual gauge theory, and the geometric interpretation of quark masses and condensates within this setup.

4.2 The model for Dp-Dq systems

At zero temperature, a general Dp-brane can be described by the metric

$$ds_{10}^2 = g_{tt}(r)\,dt^2 + g_{xx}(r)\,[(dx^1)^2 + \cdots + (dx^p)^2] + g_{rr}(r)\,d\vec{y}\cdot d\vec{y}, \tag{4.1}$$

where $g_{tt}(r)$, $g_{xx}(r)$ and $g_{rr}(r)$ are the metric components that depend on the radial direction. This radial direction is defined by the norm

$$r = \sqrt{\vec{y}\cdot\vec{y}}. \tag{4.2}$$

The terms with $g_{tt}(r)$ and $g_{xx}(r)$ belong to the space where the Dp-brane is embedded. The outer dimensions, defined by $\vec{y}$ coordinates, complete the ten-dimensional space. Therefore, they are the transverse coordinates to the Dp-brane. To determine the general notation of them, we can calculate "10 - 1 (time component) - p components (of Dp-

brane)", i.e., the tranverse coordinates can be explicitly defined by

$$\vec{y} = (y^1, \ldots, y^{9-p}). \tag{4.3}$$

To promote interaction, one can introduce a stack of Dq-branes that will be treated as probes.

To be more concrete: imagine you have a 10 dimensional space. One can insert a stack of N_p Dp-branes and do the same including N_q Dq-branes. Of course they will have common dimensions to promote interactions from the intersection of these dimensions. The number of branes of each kind is a subtle resource to mimic some characteristic of QCD. There, the quarks have color and flavor as fundamental features. We have three colors and six flavors. One could adjust the brane configuration to reproduce these properties. For this reason, the D3-branes are related with the color symmetry, represented by the SU(N_c) group whereas the D7-branes can represent the flavor symmetry and the group representation is done by SU$(N_f)_L \times$ SU$(N_f)_R$, being L and R indexes the representations of the chirality. That is why we have N_c Dp-branes and N_f Dq-branes. The probe branes, named here by Dq, will always represent the flavor sector and for being probe they do not exhibit the backreaction. That is the way we can get the proximity to QCD.

Let us consider the inclusion of N_f Dq-brane probes in that ten-dimensional space with the condition $N_c \gg N_f$. Of course it is related to the 't Hooft limit as well, but here the special meaning is to consider a smaller amount of Dq-brane to be considered as probes. Actually, by taking the 't Hooft limit, we obtain $AdS_5 \times S^5$ with N_f D7-branes wrapping the $AdS_5 \times S^3$. To simplify this idea, if we consider the zero temperature, zero mass,

and zero density as conditions, the worldvolume of the S^3 sphere is the maximum-volume equatorial where $S^3 \subset S^5$ (KARCH; O'BANNON, 2007).

These branes are extended along the directions

$$Dq : (t, x^1, \ldots, x^n, y^1, \ldots, y^{q-n}). \tag{4.4}$$

This n represents the amount of commom spatial dimensions of the Dp and Dq. There is a way to represent the intersection and one can do it by using the table

	x^1	...	x^n	x^{n+1}	...	x^p	y^1	...	y^{q-n}	y^{q-n+1}	...	y^{9-p}
Dp	×	...	×	×	...	×	-	...	-	-	...	-
Dq	×	...	×	-	...	-	×	...	×	-	...	-

This is a generalized composition of Dp–Dq branes living inside the 10-dimensional spacetime. In the table above, each "×" indicates that the corresponding brane extends along that specific spatial coordinate, meaning the brane has access to that direction in spacetime. On the other hand, a "−" symbol denotes that the brane does not span that coordinate — it is not embedded in that direction and therefore does not participate in the geometry along that axis.

There is a notation to represent this configuration $(n \,|\, p \perp q)$ where n, p and q are, respectively, the number of common spatial dimensions, the number of spatial dimensions of the Dp-brane and the number of spatial dimensions of Dq-brane (ITSIOS *et al.*, 2016). The symbol $\perp$ means the transverse relation that exists between the outer spatial dimensions of the Dp-Dq system, where we have no branes living there.

One can check from the configuration above that we have n common directions. Outside these common coordinates, one can also check that the Dp-brane has $p - n$ [1]

[1] For Dp-brane: $p - (n + 1) + 1 = p - n$.

directions whereas the Dq-brane has $q-n$ [2] directions. The outer space has $9+n-p-q$ [3] directions.

For convenience, one can replace all the outer/transverse coordinates of the Dp and Dq as

$$\vec{z} = (z^1, \ldots, z^{9+n-p-q}), \tag{4.5}$$

with

$$z^m = y^{q-n+m}, \tag{4.6}$$

for $m = 1, \ldots, 9+n-p-q$. Furthermore, it is possible to create a radial coordinate ρ responsible for the subspace spanned by $(y^1, \ldots, y^{q-n})$ on that way

$$\rho^2 = (y^1)^2 + \cdots + (y^{q-n})^2. \tag{4.7}$$

This subspace is important to describe the full space of Dq-brane without having any intersection with the Dp-brane. And this new coordinate can help us to write the infinitesimal form of the outer dimensions of the Dp-brane

$$d\vec{y}^{\,2} = d\rho^2 + \rho^2\, d\Omega^2_{q-n-1} + d\vec{z}^{\,2}. \tag{4.8}$$

The two first terms represent the generalized form of the polar coordinates in a plane, with the Ω representing the solid angle defined on that hyperspace.

[2] For Dq-brane: $q-n-1+1 = q-n$.
[3] For the outer space: $9-p-(q-n+1)+1 = 9+n-p-q$.

The Dp-background has a rotational symmetry in the y^i directions, i.e., from the 9 dimensional space (remember we must exclude the time on this count), we have $9-p$ dimensions outside the space where Dp-brane is embedded. Therefore, this rotational symmetry is defined by the group $SO(9-p)$. But this invariance is broken with the Dp-Dq intersection, after adding N_f coincident Dq-branes. Even so, when we add Dq-branes in this space, we introduce a new symmetry that represents what the Dq-branes physically can represent: the flavor symmetry. In other words, we are introducing the U(N_f) flavor symmetry [4].

The 10D background metric (4.1) can be rewriten with these coordinates (4.8) on that way

$$\begin{aligned} ds_{10}^2 = {} & g_{tt}(r)\, dt^2 + \\ & + g_{xx}(r)\, [\overbrace{(dx^1)^2 + \cdots + (dx^n)^2}^{of\ common\ terms} + \overbrace{(dx^{n+1})^2 + \cdots + (dx^p)^2}^{of\ Dp\ terms}] + \\ & + g_{rr}(r)\, [\underbrace{d\rho^2 + \rho^2 d\Omega_{q-n-1}^2}_{of\ Dq\ terms} + d\vec{z}^{\,2}]. \end{aligned} \tag{4.9}$$

That is the most general way to describe the 10D space with the intersection of these two kinds of branes. From now on, it is important to set some conditions and constraint to simplify the description.

One can start by assuming a non-trivial set of a stack of Dq-branes. This stack will be set on the transverse space of them. By using equation (4.5), one can choose the transverse coordinates in such a way that the stack can be parameterized as $\vec{z} = (z^1(\rho), 0, \ldots, 0)$.

[4] One can consider the entire system with Dp and Dq interacting within this space. The global symmetry is defined by this product SO(n,1) $\times$ U(N_f) $\times$ SO$(p-n)_p$ $\times$ SO$(q-n)_q$ $\times$ SO(9+n-p-q). The first describes the space with common directions considering the time. The second one is to describe the flavor symmetry. The third and the forth ones are, respectively, related to the spaces where Dq and Dp live. And the last one is related to the outer space.

Just to simplify the notation, we will actually write $z(\rho)$ instead of $z^1(\rho)$.

One can rewrite (4.2) on that form

$$\begin{aligned} r(\rho) &= \sqrt{\vec{y}\cdot\vec{y}} = \sqrt{(y^1)^2+\cdots+(y^{9-p})^2} \\ &= \sqrt{\underbrace{(y^1)^2+\cdots+(y^{q-n})^2}_{\rho^2} + \underbrace{(y^{q-n+1})^2}_{(z^1)^2} + \underbrace{\ldots(y^{9-p})^2}_{=0}}. \\ &= \sqrt{\rho^2+z(\rho)^{\,2}}. \end{aligned} \tag{4.10}$$

The induced metric is the new metric tensor defined within a submanifold, which is embedded on the original manifold. At zero temperature, the induced metric on the Dq-brane worldvolume is

$$\begin{aligned} ds^2_{q+1} = g_{tt}(\rho)\,dt^2 + g_{xx}(\rho)\,[(dx^1)^2+\cdots+(dx^n)^2] + \\ + g_{rr}(\rho)\,[d\rho^2+\rho^2 d\Omega^2_{q-n-1}+d\vec{z}^{\,2}]. \end{aligned} \tag{4.11}$$

Rewriting $d\vec{z}^{\,2} = \left(\frac{d\vec{z}}{d\rho}\right)^2 d\rho^2 = z'^{\,2}\,d\rho^2$, the induced metric can be rewriten on the following form

$$\begin{aligned} ds^2_{q+1} = g_{tt}(\rho)\,dt^2 + g_{xx}(\rho)\,[(dx^1)^2+\cdots+(dx^n)^2] + \\ + g_{rr}(\rho)\,[(1+z'^2)\,d\rho^2+\rho^2 d\Omega^2_{q-n-1}]. \end{aligned} \tag{4.12}$$

Let us highlight some details. The label "$q+1$" means all the q spatial directions with the one time component. All the components of the metric tensor are functions of ρ because this radial coordinate is rightly defined for Dq-branes.

One can compute the Dirac-Born-Infeld action (DBI) of the Dq-brane. The DBI action

[5] has the form

$$S_{Dq} = -N_f\, T_{Dq} \int d^{q+1}\xi\, e^{-\phi} \sqrt{-\det(g + 2\pi\, \alpha'\, F)}\,, \tag{4.13}$$

where N_f is the number related to the stack of Dq-brane, T_{Dq} is the tension of the Dq-brane, ϕ is the dilaton field and α' is the inverse of the string tension. [6] The field strength F can be defined considering the worldvolume with components $\rho\,,\, t$

$$F = \frac{\partial A_t}{\partial \rho}\; d\rho \wedge dt = (\partial_\rho A_t)\;\; d\rho \wedge dt = A_t'\; d\rho \wedge dt\,, \tag{4.14}$$

where the label t is related to the time component of A with the extra condition $A_\rho = 0$ as a gauge choice. Additionally, the Dq-brane tension can be defined as (check the details on Appendix (**A**))

$$T_{Dq} = \frac{1}{(2\,\pi)^q\, \sqrt{\alpha'}^{\,q+1}\, g_s}. \tag{4.15}$$

The term g_s is the effective string coupling (MATSUMOTO, 2022). In fact, for weak coupling regime, this term can be evaluated by the expectation value of the dilaton term, i. e., $g_s =< e^{-\phi} > + \ldots$ (ALWIS, 1996).

The infinitesimal worldvolume represented by $d^{q+1}\xi$ can be split as follows

$$\int d^{q+1}\xi = \int dt\; d^n x\; d\rho\, d\Omega_{q-n-1}\,, \tag{4.16}$$

[5] The DBI action is the action for the probe and it is defined in $AdS_5 \times S^3$. And as we will check later, the time component of the gauge field U(1) is dual to the chemical potential μ, while the asymptotic distance of the D3 and D7-branes is the mass parameter m that will be called by quark constituent mass.

[6] As previously discussed in Section (2.2), the α term is actually related to the tension from expression $T = \frac{1}{2\pi\alpha}$. At a phenomenological approach, this term is the slope of the Regge trajectories. As it is defined in units of area, it is common to find the relation $l_s = \hbar c\sqrt{\alpha'}$, where l_s is the string length. Using natural units, it is simply $l_s = \sqrt{\alpha'}$.

where the integral in $d\Omega_{q-n-1}$ is the solid angle. One can recognize this integral as corresponding to the volume of a $(q-n-1)$-dimensional sphere with radius R, that is Appendix (**B**)

$$\int d\Omega_{q-n-1} = \mathrm{Vol}_{q-n}\left(\mathrm{S}^{q-n-1}\right) = \frac{2\,\pi^{\frac{q-n}{2}}}{(q-n)\;\Gamma\left(\frac{q-n}{2}\right)}\,R^{\,q-n}. \tag{4.17}$$

To simplify the notation, we can represent all these terms on the following form (MATEOS *et al.*, 2007)

$$\mathcal{N} = N_f\,T_{Dq}\,\mathrm{Vol}_{q-n}(\mathrm{S}^{q-n-1})\,. \tag{4.18}$$

Finally, the DBI action becomes

$$S_{Dq} = -\mathcal{N}\int dt\;d^n x\;d\rho\;e^{-\phi}\sqrt{-\det(g+2\pi\,\alpha'\,F)}\,. \tag{4.19}$$

4.2.1 The DBI term

At this point, we need to analyze the DBI term appearing under the square root. To do so, we begin by writing the matrix form of the metric tensor and the field strength. The former follows directly from (4.12), while the latter requires a more careful treatment. In particular, we need to explore some concepts involving differential forms, which will facilitate the computation of the determinant.

This procedure is fully detailed in Appendix (**C**), where it is shown that the DBI term

simplifies to the following expression

$$\sqrt{-\det(g+2\,\pi\,\alpha'\,F)} = \rho^{\,q-n-1}\, g_{rr}{}^{\frac{q-n-1}{2}}\; g_{xx}{}^{\frac{n}{2}}\; \sqrt{(1+z'^2)\,|g_{tt}|\,g_{rr} - (2\,\pi\,\alpha'\,A_t')^2}. \quad (4.20)$$

4.2.2 Charge density and condensate

In the appendix of (ITSIOS *et al.*, 2016), one can verify the way to recognize all the metric components (and the dilaton field as well) after applying a perturbation method. After these manipulation and considering the entire Dq-brane space, one can get (BLUMENHAGEN *et al.*, 2013)

$$-g_{tt} = g_{xx} = \left(\frac{r}{R}\right)^{\frac{7-p}{2}} \quad , \quad g_{rr} = \left(\frac{R}{r}\right)^{\frac{7-p}{2}} \quad , \quad e^{-2\phi} = \left(\frac{R}{r}\right)^{\frac{(7-p)(p-3)}{2}} \quad (4.21)$$

Note that $|g_{tt}|\,g_{rr} = 1$. This result happens in the Schwarzschild case. Remember: when we want to construct the Schwarzschild metric, there is a condition at the exponential of the time and radial components functions and, therefore, we get this same result.

One can rewrite the DBI term by using these last results

$$\begin{aligned}\sqrt{-\det(g+2\,\pi\,\alpha'\,F)} &= \rho^{\,q-n-1}\,\left(\frac{R}{r}\right)^{\frac{(7-p)(q-n-1)}{4}}\;\left(\frac{r}{R}\right)^{\frac{n(7-p)}{4}}\;\sqrt{(1+z'^2)\,-(2\,\pi\,\alpha'\,A_t')^2} \\ &= \rho^{\,q-n-1}\,\left(\frac{r}{R}\right)^{\frac{(7-p)(2n-q+1)}{4}}\;\sqrt{(1+z'^2)\,-(2\,\pi\,\alpha'\,A_t')^2} \quad (4.22)\end{aligned}$$

Replacing the last equation into (4.19) and using the dilaton field from (4.21), one

gets

$$S_{Dq} = -\mathcal{N} \int dt\ d^n x\ d\rho\ \left(\frac{R}{r}\right)^{\frac{(7-p)(p-3)}{4}}\ \rho^{\,q-n-1}\ \left(\frac{r}{R}\right)^{\frac{(7-p)(2n-q+1)}{4}}\ \sqrt{(1+z'^2)\ -(2\,\pi\,\alpha'\,A'_t)^2}$$

$$= -\mathcal{N} \int dt\ d^n x\ d\rho\ \ \rho^{\,q-n-1}\ \left(\frac{r}{R}\right)^{\frac{(7-p)(2n-p-q+4)}{4}}\ \sqrt{(1+z'^2)\ -(2\,\pi\,\alpha'\,A'_t)^2}, \qquad (4.23)$$

and setting $R = 1$ for the radius, we get

$$S_{Dq} = -\mathcal{N} \int dt\ d^n x\ d\rho\ \ \rho^{\,q-n-1}\, r^{\frac{(7-p)(2n-p-q+4)}{4}}\ \sqrt{(1+z'^2)\ -(2\,\pi\,\alpha'\,A'_t)^2}. \qquad (4.24)$$

The term $2\pi\alpha'$ is a constant term. One can rewrite the gauge field by absorbing this term from the redefinition of A_t. The cleaner version of this expression becomes

$$S_{Dq} = -\mathcal{N} \int dt\ d^n x\ d\rho\ \ \rho^{\,q-n-1}\, r^{\frac{(7-p)(2n-p-q+4)}{4}}\ \sqrt{1+z'^2\ -A'^2_t}. \qquad (4.25)$$

To further simplify this expression, let us start a discussion about the r term.

As you can see above, the dependence on z is induced by the power of r. When this action depends on z' instead of z, the function $z(\rho)$ is a cyclic variable [7]. To guarantee this condition, we must impose

$$2n - p - q + 4 = 0 \quad \rightarrow \quad n = \frac{p+q-4}{2}. \qquad (4.26)$$

This condition is related to the cases with the **supersymmetric intersections**. From

[7] There is another way to say the same thing. In literature, you can find "symmetric" for this case. If the Lagrangian by Euler-Lagrange equations can exhibit the result $\frac{\partial \mathcal{L}}{\partial x} = 0$, you can say that this Lagrangian is symmetric in x. In other words, there is a conserved momentum related to this coordinate explained by Noether's theorem.

this, one can get the intersections $(p\,|\,p\perp p+4)$, $(p-1\,|\,p\perp p+2)$ and $(p-2\,|\,p\perp p)$. It is convenient to define a new parameter λ on that form

$$\lambda = 2(q-n-1) = 2\left(q-\frac{p+q-4}{2}-1\right) = q-p+2. \tag{4.27}$$

And it is easy to see that

$$\lambda = 6 \quad \rightarrow \quad q = p+4 \quad \rightarrow \quad \mathrm{D}p-\mathrm{D}(p+4)\text{ intersection}, \tag{4.28}$$

$$\lambda = 4 \quad \rightarrow \quad q = p+2 \quad \rightarrow \quad \mathrm{D}p-\mathrm{D}(p+2)\ \text{ intersection}, \tag{4.29}$$

$$\lambda = 2 \quad \rightarrow \quad q = p \quad \rightarrow \quad \mathrm{D}p-\mathrm{D}p\text{ intersection}. \tag{4.30}$$

From these discussions, one can rewrite the DBI action to get

$$S_{Dq} = \int dt\ d^n x\ d\rho\, \mathcal{L}_{DBI} = -\mathcal{N}\int dt\ d^n x\ d\rho\ \rho^{\frac{\lambda}{2}}\ \sqrt{1+z'^2\ -A_t'^2}, \tag{4.31}$$

the Lagrangian density being

$$\mathcal{L}_{DBI} = -\mathcal{N}\,\rho^{\frac{\lambda}{2}}\ \sqrt{1+z'^2\ -A_t'^2}\,. \tag{4.32}$$

As the DBI action does not exhibit the z and A_t dependences, one could get the following conservation laws

$$\frac{1}{\mathcal{N}}\frac{\partial\mathcal{L}_{\mathcal{DBI}}}{\partial z'} = -\frac{\rho^{\frac{\lambda}{2}}\ z'}{\sqrt{1+z'^2-A_t'^2}} \equiv -c\,, \tag{4.33}$$

$$\frac{1}{\mathcal{N}}\frac{\partial\mathcal{L}_{\mathcal{DBI}}}{\partial A_t'} = \frac{\rho^{\frac{\lambda}{2}}\ A_t'}{\sqrt{1+z'^2-A_t'^2}} \equiv d\,, \tag{4.34}$$

where c and d are constant parameters that came from $\frac{\partial \mathcal{L}_{\rm DBI}}{\partial z} = 0$ and $\frac{\partial \mathcal{L}_{\rm DBI}}{\partial A_t} = 0$.

One can invert these expression to write z' and A'_t in terms of ρ^λ, c and d. After some algebraic process, we get

$$z' = \frac{c}{\sqrt{\rho^\lambda + d^2 - c^2}}\,, \tag{4.35}$$

$$A'_t = \frac{d}{\sqrt{\rho^\lambda + d^2 - c^2}}, \tag{4.36}$$

which leads to the relation: $z' = \frac{c}{d}\, A'_t$.

Let us analyze these expressions for some possible cases.

For the case $c = d \neq 0$, we have $z' = \frac{c}{\sqrt{\rho^\lambda}}$ and $A'_t = \frac{d}{\sqrt{\rho^\lambda}}$. Both expressions state that we have a divergence at $\rho = 0$. To avoid this problem we will impose the condition $d^2 > c^2$. Doing the same calculation now, one could check that the point $\rho = 0$ is allowed.

One can start by integrating the A'_t expression above. In this process, we will use the condition $A_t(0) = 0$, i.e.

$$A_t(\rho) = d \int_0^\rho \frac{d\bar{\rho}}{\sqrt{\bar{\rho}^\lambda + d^2 + c^2}}\,. \tag{4.37}$$

The integral in Eq. (4.37) can be written in terms of hypergeometric function (ARFKEN; WEBER, 2007), as follows

$$A_t(\rho) = \frac{d}{(d^2 - c^2)^{\frac{1}{2} - \frac{1}{\lambda}}} \frac{\rho}{(\rho^\lambda + d^2 - c^2)^{\frac{1}{\lambda}}}\, {}_2F_1\left(\frac{1}{\lambda}, \frac{1}{2} + \frac{1}{\lambda}; 1 + \frac{1}{\lambda}; \frac{\rho^\lambda}{\rho^\lambda + d^2 - c^2}\right). \tag{4.38}$$

Doing exactly the same to $z(\rho)$, one can get

$$z(\rho) = \frac{c}{(d^2-c^2)^{\frac{1}{2}-\frac{1}{\lambda}}} \frac{\rho}{(\rho^\lambda + d^2 - c^2)^{\frac{1}{\lambda}}} \, {}_2F_1\left(\frac{1}{\lambda}, \frac{1}{2}+\frac{1}{\lambda}; 1+\frac{1}{\lambda}; \frac{\rho^\lambda}{\rho^\lambda + d^2 - c^2}\right). \tag{4.39}$$

As you can see, there is a subtle difference between them. With non-zero c and d, at the point $\rho = 0$, the results are $A_t(0) = z(0) = 0$, as it was built to be.

It is important to highlight that at $\rho = z = 0$, with condition $d^2 > c^2$, the brane reaches a region called *Poincaré horizon* [8], where a divergence happens.

In next section, we will discuss the way to find the free energy from this construction. There, these quantities c and d will be recognized as condensate and charge density of the dual theory, respectively.

4.2.3 The free energy

Our target on this section is to construct the free energy from that previous brane set up. The discussion happens considering the approach with no magnetic field and zero temperature. That thermodynamics condition allows us to reach our goal analytically. Let us consider intersections with $\lambda > 2$, i.e., cases with $q > p$.

Our starting point is the UV region where $\rho \to \infty$. There, from the holographic dictionary, the gauge field component A_t has a very known value (ITSIOS *et al.*, 2016) (NAKAMURA, 2008)

$$A_t\,(\rho \to \infty) \equiv \mu\,, \tag{4.40}$$

[8] The Poincaré horizon is located at a coordinate singularity.

where μ is the chemical potential related to the conserved charge.

To apply this condition into the expression that defines A_t, we need to analyze some limits. One of them is inside the hypergeometric function. The limit at infinity is

$$\lim_{\rho\to\infty} \frac{\rho^\lambda}{\rho^\lambda + d^2 - c^2} = 1 \quad , \quad \text{for } (c^2, d^2) \in \mathbb{R}^2 \ \forall\ \lambda > 0. \tag{4.41}$$

For this reason, the hypergeometric function becomes ${}_2F_1\left(\frac{1}{\lambda}, \frac{1}{2} + \frac{1}{\lambda}; 1 + \frac{1}{\lambda}; 1\right)$. By using the relation

$${}_2F_1(A, B, C; 1) = \frac{\Gamma(C)\ \Gamma(C - A - B)}{\Gamma(C - A)\ \Gamma(C - B)}, \tag{4.42}$$

we obtain

$${}_2F_1\left(\frac{1}{\lambda}, \frac{1}{2} + \frac{1}{\lambda}; 1 + \frac{1}{\lambda}; 1\right) = \frac{1}{\sqrt{\pi}}\ \Gamma\left(1 + \frac{1}{\lambda}\right)\ \Gamma\left(\frac{1}{2} - \frac{1}{\lambda}\right). \tag{4.43}$$

To simplify the notation, we define

$$\gamma = \frac{1}{\sqrt{\pi}}\ \Gamma\left(1 + \frac{1}{\lambda}\right)\ \Gamma\left(\frac{1}{2} - \frac{1}{\lambda}\right). \tag{4.44}$$

There is another term that we need to check the limit. Doing the same analysis, we get

$$\lim_{\rho\to\infty} \frac{\rho}{(\rho^\lambda + d^2 - c^2)^{\frac{1}{\lambda}}} = 1 \quad , \quad \text{for } (c^2, d^2) \in \mathbb{R}^2 \ \forall\ \lambda > 0 \tag{4.45}$$

After these steps, one can rewrite equation (4.38) in the form

$$A_t(\rho \to \infty) = \ \mu \ = \frac{d}{(d^2 - c^2)^{\frac{1}{2}-\frac{1}{\lambda}}}\,\gamma. \tag{4.46}$$

Similarly, doing the same to the z case, we can get that the UV value (at the case ρ going to the infinity) is the mass parameter. Therefore, from the holographic dictionary we can write down

$$z(\rho \to \infty) = \ m \ = \frac{c}{(d^2 - c^2)^{\frac{1}{2}-\frac{1}{\lambda}}}\,\gamma. \tag{4.47}$$

Here it is clear that those integration constants indeed have physical meanings and they come from the holographic dictionary applied at the UV regime as we did above.

One can invert these two last equations to show c and d in terms of m and μ. Subtracting after squaring these equation we immediately get

$$\mu^2 - m^2 = (d^2 - c^2)^{\frac{2}{\lambda}}\,\gamma^2. \tag{4.48}$$

From the condition we imposed before, $d^2 > c^2$, we can check from the last equation that $\mu > m$.

Using equations (4.46) and (4.47), we find after some algebric process

$$c = m\,\gamma^{\frac{-\lambda}{2}}\,(\mu^2 - m^2)^{\frac{\lambda-2}{4}}, \tag{4.49}$$

$$d = \mu\,\gamma^{\frac{-\lambda}{2}}\,(\mu^2 - m^2)^{\frac{\lambda-2}{4}}. \tag{4.50}$$

Considering just the intersections with $\lambda > 2$, the case $\mu = m$ lead us to $c = d = 0$. That result, as discussed above, is related to the vanishing density and characterized for being the Minkowski embedding. You can check more details in (KARCH; O'BANNON, 2007).

Right now we do have all the structures to evaluate the action. That action can be evaluated at the on-shell condition. The first step is to replace the expressions we found before. Let us start with the on-shell form for the DBI action

$$S_{Dq}^{\text{on-shell}} = -\mathcal{N} \int d\rho \ \rho^{\frac{\lambda}{2}} \sqrt{1 + z'^2 - A_t'^2}\,. \tag{4.51}$$

To evaluate this action we need to replace the expressions for z' and A_t'. By using equations (4.35) and (4.36), the square root term becomes

$$\sqrt{1 + z'^2 - A_t'^2}\Big|_{\text{on-shell}} = \sqrt{1 + \frac{c^2}{\rho^\lambda + d^2 - c^2} - \frac{d^2}{\rho^\lambda + d^2 - c^2}} = \frac{\rho^{\frac{\lambda}{2}}}{\sqrt{\rho^\lambda + d^2 - c^2}}. \tag{4.52}$$

Substituting this expression into Eq. (4.51), one gets

$$S_{\text{on-shell}} = -\mathcal{N} \int_0^\infty d\rho \ \ \frac{\rho^\lambda}{\sqrt{\rho^\lambda + d^2 - c^2}}. \tag{4.53}$$

This integral diverges and therefore the action must be regulated. This is a renormalization process and it is made by subtracting the divergence (the term S_0) [9]. When $d = c = 0$ the divergence is revealed and therefore we must subtract the integral with the remaining term $\frac{\rho^\lambda}{\sqrt{\rho^\lambda}} = \rho^{\frac{\lambda}{2}}$.

The regulated on-shell action, computed using the Minimal Subtraction Scheme, has

[9] The regulated action is obtained by considering the new action defined by subtracting the divergence, i. e., when the integrand is evaluated at the UV.

the form (KARCH *et al.*, 2009)

$$S^{\,\mathrm{reg}}_{\text{on-shell}} = \lim_{\zeta\to\infty}\left(S_{Dq} - S_0\right) = -\mathcal{N}\lim_{\zeta\to\infty}\left(\int_0^{\zeta} d\rho \;\; \frac{\rho^{\lambda}}{\sqrt{\rho^{\lambda}+d^2-c^2}} \;-\; \int_0^{\zeta} d\rho \;\; \rho^{\frac{\lambda}{2}}\right)$$

$$= \frac{2\mathcal{N}}{\lambda+2}\,\left(d^2-c^2\right)^{\frac{1}{\lambda}+\frac{1}{2}}\,\gamma\,. \tag{4.54}$$

At zero temperature [10], one recognizes the relation between the regulated on-shell action with the grand canonical potential (KARCH *et al.*, 2009), that is

$$S^{\,\mathrm{reg}}_{\text{on-shell}} \equiv -\mathcal{F}. \tag{4.55}$$

The minus sign is a consequence of the thermodynamic relation between the pressure and the free energy function. Explicitly, the grand canonical potential can be written as

$$\mathcal{F} = -\frac{2\mathcal{N}}{\lambda+2}\,\left(d^2-c^2\right)^{\frac{1}{\lambda}+\frac{1}{2}}\,\gamma\,. \tag{4.56}$$

By using equation (4.48) we get

$$\mathcal{F} = -\frac{2\mathcal{N}}{\lambda+2}\,\left(\mu^2-m^2\right)^{\frac{\lambda+2}{4}}\,\gamma^{\frac{-\lambda}{2}}\,. \tag{4.57}$$

From (D.14), in Appendix (**D**), we have

$$\frac{\partial\mathcal{F}}{\partial\mu} = -\rho = \mu\,\mathcal{N}\,\gamma^{\frac{-\lambda}{2}}\left(\mu^2-m^2\right)^{\frac{\lambda-2}{4}} = \mathcal{N}\,d\,. \tag{4.58}$$

[10]The free energy can be split into two parts. The first one comes from the adjoint representation, that is, the $\mathcal{F}_{\mathcal{N}=4}$ and the second one comes from the flavor field. By considering that the adjoint part has the form $\mathcal{F}_{\mathcal{N}=4}\sim T^4$, it means that when considering an approach at zero temperature, this part does not contribute to the total free energy.

In other words, the constant d is related to the charge density as we can check by equation (4.50).

See the details of these thermodynamics construction on Appendix (**D**).

For the D3-D7 brane configuration, we set $\lambda = 6$ and we obtain

$$\mathcal{F} = -\frac{\mathcal{N}}{4}\left(\mu^2 - m^2\right)^2 \gamma^{-3}\,. \tag{4.59}$$

That choice, explained by (4.28), shows that we can reach the supersymmetric case D3-D7.

The expression above has the parameter $\mathcal{N}$, which is defined by equation (4.18). From now on, we will use the expression found in (HOYOS *et al.*, 2016):

$$\mathcal{F} = -\frac{N_c N_f}{4\gamma^3\,\lambda_{YM}}(\mu^2 - m^2)^2\,, \tag{4.60}$$

being $\lambda_{YM} = \frac{3\pi^2}{\gamma^3} \sim 10.74$, the 't Hooft coupling. For our application, we set $N_c = N_f = 3$. On QCD perspective, it would be considering the three colors of quarks and three kinds of flavors. The final expression for the free energy is given by

$$\mathcal{F} = -\frac{9}{12\pi^2}(\mu^2 - m^2)^2\,. \tag{4.61}$$

At a large chemical potential where $\mu \gg m$, from a QCD perspective, the free energy reaches the Stefan-Boltzmann value (FREEDMAN; MCLERRAN, 1977). The pressure P can be easily found by the relation $P = -\mathcal{F}$ (see Appendix (**D**)).

4.3 Summary

In this chapter we have a detailed discussion of the Dp-Dq brane configuration. This model can be applied, for example, for the D3-D7 instersection, that is exactly what we do later.

We saw that the construction starts by considering the stack of branes in a 10D space where the string theory is defined. There is one condition to get just the supersymmetric cases and, after using the holographic dictionary, we found the regulated on-shell DBI action which is recognized as the grand canonical potential with opposite sign.

It is important to derive the pressure and the energy density after some thermodynamic considerations. These quantities will used in the Tolman-Oppenheimer-Volkoff equation and all the study that we can reach from it.

Next, we will present the first application of the holographic quark model introduced earlier. We will discuss its application in the investigation of compact objects known as quark stars, which generalize the possibility of quark dissociation in a nuclear environment subjected to extreme thermodynamic and gravitational conditions.

5 Quark Stars

The idea that compact stars could be entirely composed of deconfined quark matter — known as the *quark star hypothesis* — has sparked considerable interest in recent decades. See (ALCOCK *et al.*, 1986) and the references therein. Although no such objects have been confirmed observationally, the hypothesis is supported by theoretical arguments from Quantum Chromodynamics (QCD) and the physics of dense matter.

The main motivation comes from the expectation that, under extreme densities and low temperatures — as found in the cores of neutron stars — nucleons might dissolve into their constituent quarks. If this deconfinement takes place throughout the entire star, it would result in a compact object made purely of quark matter. Such a star would form a new class of compact objects, possibly more compact and stable than traditional neutron stars.

The main goal of this work is to investigate both static and dynamic properties of quark stars. The results presented in this chapter are based on original work published in (ALEIXO *et al.*, 2024), in which we applied a flavor-independent holographic model derived from a D3–D7 brane setup to study dense quark matter and its role in the internal structure of quark stars.

In that study, we analytically derived an equation of state from the dynamics of a probe

D7-brane embedded in an $AdS_5 \times S^5$ background sourced by a stack of D3-branes. The resulting EoS depends solely on a single phenomenological parameter—the constituent quark mass—and was used to solve the Tolman–Oppenheimer–Volkoff equations for static stellar configurations. We computed the corresponding mass-radius relations and the dimensionless tidal deformability for a range of constituent quark masses.

The results were compared with observational constraints from NICER, for the pulsars PSR J0030+0451 and PSR J0740+6620, as well as with data from the LIGO–Virgo collaboration related to the gravitational wave event GW170817. The analysis showed that, within the flavor-symmetric version of the model, it is not possible to simultaneously satisfy both sets of observational constraints.

5.1 Application: building the TOV

As we discussed in the last chapter, the pressure can be found by the equality $\mathcal{F} = -P$. By doing this, we get the equation for **pressure**

$$P = \frac{9}{12\pi^2} (\mu^2 - m^2)^2 \,. \tag{5.1}$$

The energy density can be found by using the relation

$$\varepsilon \,=\, \mu \,\left(\frac{\partial P}{\partial \mu}\right) \,-\, P \,, \tag{5.2}$$

which is derived in Appendix (**D**).

One can rewrite equation (5.1) for μ in terms of pressure. By doing that, we get

$$\mu = \sqrt{\frac{2\pi\sqrt{P}}{\sqrt{3}} + m^2}. \tag{5.3}$$

By replacing this last equation into (5.2) after deriving the pressure with respect to μ, we find the expression for the **energy density** (ANNALA *et al.*, 2018)

$$\varepsilon = 3P + \frac{2\sqrt{3}\,m^2}{\pi}\sqrt{P}. \tag{5.4}$$

Since we want to apply the D3-D7 model for compact stars, these stars must be at hydrostatic equilibrium. There is a way to approach this condition. Every star that satisfies this condition obeys the Tolman–Oppenheimer–Volkoff equation (TOV). The derivation is on Appendix (**E**).

The TOV equation is given by

$$\frac{dP(r)}{dr} = -\frac{GM(r)\rho}{r^2}\left(1 + \frac{4\pi r^3 P(r)}{M(r)c^2}\right)\left(1 + \frac{P(r)}{\rho c^2}\right)\left(1 - \frac{2GM(r)}{rc^2}\right)^{-1}; \tag{5.5}$$

$$\frac{dM(r)}{dr} = 4\pi r^2 \rho(r), \tag{5.6}$$

where $P(r)$ is the pressure at position r, the $M(r)$ is the mass inside the r radius and ρ is the mass density with $\varepsilon = \rho c^2$ the energy density. Using natural units, where the Newton constant G and the speed of light c are 1, one can rewrite these equations in the form

$$\frac{dP(r)}{dr} = -\frac{\left(M(r) + 4\pi r^3 P(r)\right)\left(\varepsilon(r) + P(r)\right)}{r\left(r - 2M(r)\right)}; \tag{5.7}$$

$$\frac{dM(r)}{dr} = 4\pi r^2\, \varepsilon(r)\,. \tag{5.8}$$

The set of equations has, as inputs, the pressure and the energy density. Both of them we already found above on (5.1) and (5.4). Since we enter with these relations, we can construct the TOV equation for this specific description.

One of the biggest advantage of having built the TOV equation is to get the **mass-radius relation**, that is, a diagram in which each point represents a stellar configuration that satisfies the TOV equations.

5.2 Causality

Before determining the mass–radius relation, it is worth emphasizing the speed of sound as an important parameter in assessing the causal behavior of the model. The causality condition requires that the speed of sound always remains below the speed of light. Using Equation (5.4), the analytical expression obtained for the speed of sound v_s is (BEDAQUE; STEINER, 2015)

$$v_s = \sqrt{\frac{\partial p}{\partial \varepsilon}} = \sqrt{\frac{\pi\sqrt{p}}{\sqrt{3}\,m^2 + 3\pi\sqrt{p}}}. \tag{5.9}$$

From figure 5.1, it can be confirmed that for the model under consideration — within the chosen range of constituent quark mass values — none of the results obtained violate the principle of causality.

In relativistic systems, causality imposes an upper bound on the speed of sound: $v_s \leq 1$, while thermodynamic stability requires $v_s^2 > 0$. However, it is widely conjectured that more restrictive bounds may apply in realistic materials. For example, in non-relativistic systems, the speed of sound is naturally much smaller than the speed of light.

On the other hand, in an ultrarelativistic gas composed of massless particles, one finds $v_s^2 = 1/3$, a value also predicted by conformal field theories due to the relation $\varepsilon = 3p$ implied by a vanishing trace of the energy–momentum tensor.

Introducing finite mass or interactions typically lowers the speed of sound below this conformal limit. This is confirmed in QCD at asymptotically high densities, where perturbative methods are applicable and $v_s^2 < 1/3$. It is therefore reasonable to expect that, at intermediate densities, the speed of sound interpolates between the low-density and high-density limits without exceeding the conformal bound, which happens in the actual model. Nonetheless, some models predict a possible peak — a "bump" — in v_s at intermediate densities, before asymptotically approaching 1/3 from below. For a more detailed discussion on this topic, see the analysis presented in (BEDAQUE; STEINER, 2015)

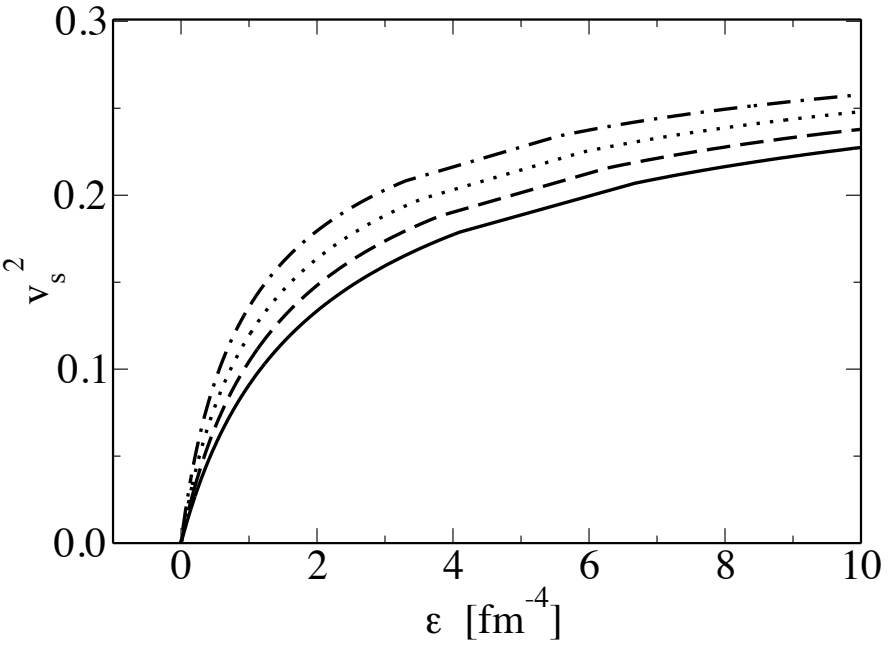

FIGURE 5.1 – v_s^2 (squared speed of sound) vs ε (energy density) for each parameterization. Dot-dashed line: m = 300 MeV. Dotted line: m = 320 MeV. Dashed line: m = 340 MeV. Solid line: m = 360 MeV. Published in (ALEIXO *et al.*, 2024).

5.3 The Mass-Radius relation

The system of equations formed by (5.7), (5.8) and the equation of state (5.4) must be solved simultaneously. To solve the TOV numerically, the standard process is considering the initial conditions. The energy density in the center has a specific value $\varepsilon(r = 0) \equiv \varepsilon_0$ and the same happens to the pressure, i.e., $p(r = 0) \equiv p_0$. After performing the chain rule $\frac{dp}{dr} = \frac{d\varepsilon}{dr}\frac{dp}{d\varepsilon}$, one can deal with ε_0 as a free parameter and after doing that, a given value determines one single point in the M-R diagram. The entire diagram is obtained by varying ε_0 numerically some orders of magnitude (VELTEN *et al.*, 2016). In general, the result provides masses related to two different radii. That is why this diagram is called mass-radius relation instead of considering $M(R)$ as if it were a function.

It is important to highlight that for the present model, we have two terms for masses. The first one m is interpreted as the constituent quark mass, which is within the model. The second one, $M(r)$, comes from the TOV equation and it related to the total mass inside the radius r.

For this model, we have a specific curve for each value for m. And this free parameter can change the behavior of the curve as we can check by figure 5.2, where the mass-radius relation was plotted. The red and blue regions in the diagram represent the 95% confidence intervals for the masses and radii of the pulsars PSR J0030+0451 and PSR J0740+6620 measured by NICER (RILEY *et al.*, 2019) (MILLER *et al.*, 2019) (MILLER *et al.*, 2021) (RILEY *et al.*, 2021). The green horizontal line represents the lower bound of all observed masses over $2M_\odot$ including the pulsars PSR J1614-2230, PSR J0348+0432 and PSR J0740+6620 (DEMOREST *et al.*, 2010) (ANTONIADIS *et al.*, 2013) (CROMARTIE *et al.*, 2019).

It is possible to notice that the value of the constituent quark mass produces a

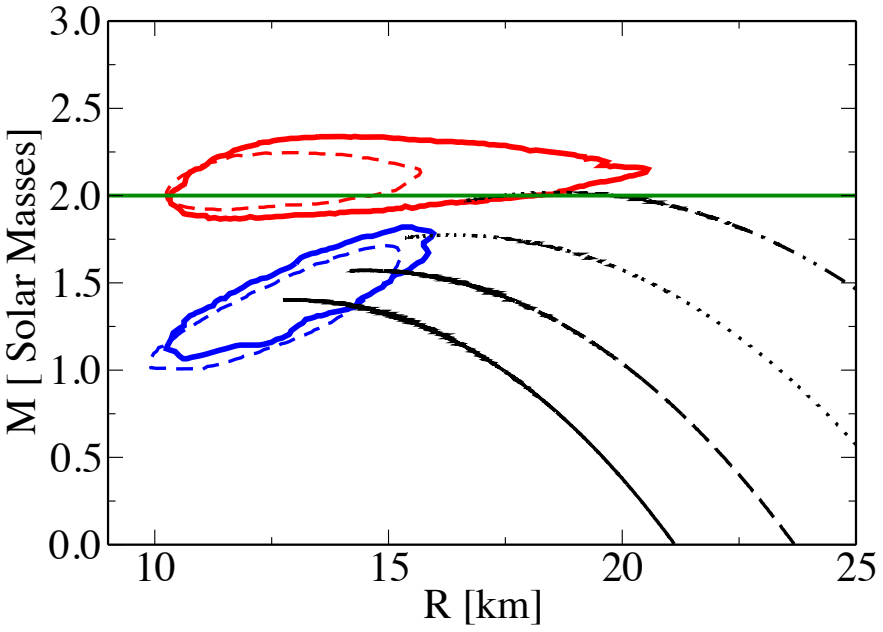

FIGURE 5.2 – Quark star mass M as a function of its radius R for different values of constituent quark mass m. Dot-dashed line: m = 300 MeV. Dotted line: m = 320 MeV. Dashed line: m = 340 MeV. Solid line: m = 360 MeV. Published in (ALEIXO *et al.*, 2024).

significant effect on the reach of the maximum mass — that is, one can conclude that as the value of m increases, the stellar maximum mass decreases.

Motivated by lattice QCD results for the infrared behavior of the quark mass function (CASTRO *et al.*, 2023) (DUARTE *et al.*, 2022), we adopt $m = 345$ MeV as a reference value. This estimate, obtained from calculations of the quark propagator (OLIVEIRA *et al.*, 2019), guides our choice of parameters. Accordingly, we explore values near this reference to confirm whether the holographic model under consideration is capable of capturing observational features related to both static and dynamical properties of neutron stars.

5.4 Stability

The TOV solutions represent the stellar configurations in hydrostatic equilibrium. But a star at hydrostatical equilibrium does not necessarily exhibit a condition of stability.

This analysis starts with the microscopic stability of matter, that is, the Le Chatelier's principle which states (GLENDENNING, 2000)

$$\frac{dP}{d\varepsilon} > 0, \tag{5.10}$$

$\epsilon = \rho c^2$ being the component T_0^0 of the energy-momentum tensor and P the pressure. That quantity is also related to the speed of sound v_s^2, defined by (5.9).

To study the equilibrium conditions, we just need to remember the classical conditions that define the unstable and stable equilibrium conditions. These configurations can be defined in the region in the mass-central density curve where (SHAPIRO; TEUKOLSKY, 2004)

$$\frac{\partial M}{\partial \varepsilon_c} > 0 \qquad \text{stable configuration,} \tag{5.11}$$

$$\frac{\partial M}{\partial \varepsilon_c} < 0 \qquad \text{unstable configuration.} \tag{5.12}$$

These conditions are precisely the same as the HZN (Harrison–Zel'dovich–Novikov) conditions previously discussed in Chapter (3). See Equation 3.12, where one can verify that the central density satisfies the equality $\rho_c = \varepsilon_c$.

In figure 5.3, four curves establishing the relation between the mass with the central energy density were plotted. By using the criteria for instability discussed above, it is

possible to see that all the circles on the figure are located on the $\frac{\partial M}{\partial \varepsilon_c} = 0$ defining, therefore, a local maximum. That maximum point of each curve defines the maximum mass.

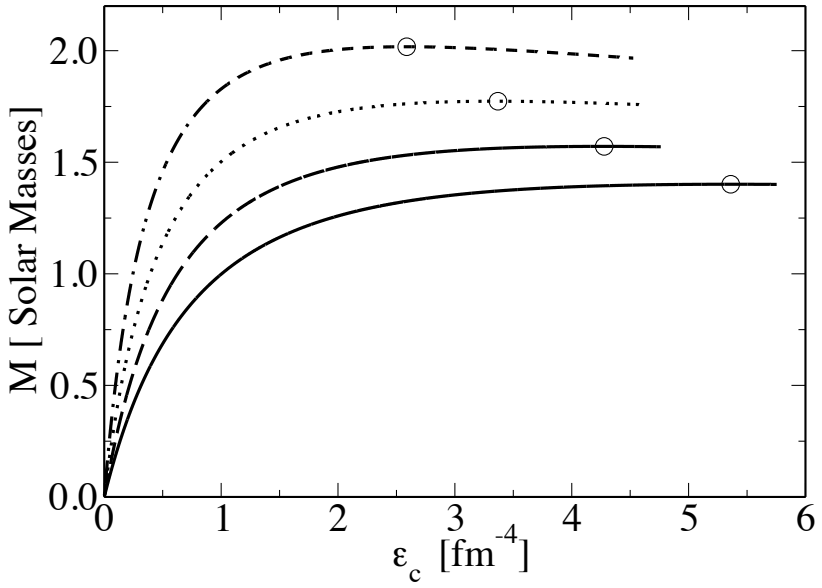

FIGURE 5.3 – Quark star mass M versus central density ε_c for different values of m. The maximum mass for each parameterization is shown by circle. Dot-dashed line: m = 300 MeV. Dotted line: m = 320 MeV. Dashed line: m = 340 MeV. Solid line: m = 360 MeV. Published in (ALEIXO *et al.*, 2024).

As an important conclusion from this diagram, one can affirm that the mass parameter works as an attenuator of the maximum value of the star mass, that is, the more we increase the value of the mass parameter m, the more it is attenuated as shown in the figure. A similar behavior with another perspective can be seen in (MATHEW *et al.*, 2020).

According to figure 5.3, all curves exhibit a very similar behavior after reaching the point corresponding to the maximum mass, showing a smooth decline as the central energy density increases. It is worth noting that as the mass parameter m decreases, the slope of the curve becomes significantly steeper at lower central densities, leading to configurations that reach masses close to $2\,M_\odot$. For mass parameter values close to 360 MeV, varying the central density above a certain value ($\varepsilon > 3$ fm^{-4}) promotes a star mass

value close to a constant $\sim 1.4M_{\odot}$, a value that will play a central role in the analysis of tidal deformabilities, whose results will be presented in the following section.

5.5 Star profiles

Another way to investigate how the star structure is established is plotting the star profiles. These diagrams can exhibit mainly the boundary conditions in addition to presenting more details about the relation that the mass and the internal pressure have with the radius. In what follows, we will present the results for the internal profiles considering the maximum mass configuration for each parameterization, under the condition $\frac{\partial M}{\partial \varepsilon_c} = 0$ shown in figure 5.3.

As discussed in (3.3), the size of a star of radius R can be defined from the condition imposed for the pressure, that is

$$P = P(r) \qquad \rightarrow \qquad P\left(r = R\right) = 0. \tag{5.13}$$

In other words, the star boundary is located where there is no pressure, no particles, or any constituent. It is the region where we can already consider the "outside". That is where the star ends. And it should be noticed by a star profile diagram that considers the relation between pressure and radius. This behavior can be clearly observed in figure 5.4, where the parameterization is defined by the mass parameter.

As we can see, the pressure reaches its highest value for $m = 360$ MeV, and when we increase the radius value all the curves go to zero defining, therefore, the radius of the star. It is another result from this holographic model and this behavior is similar to what

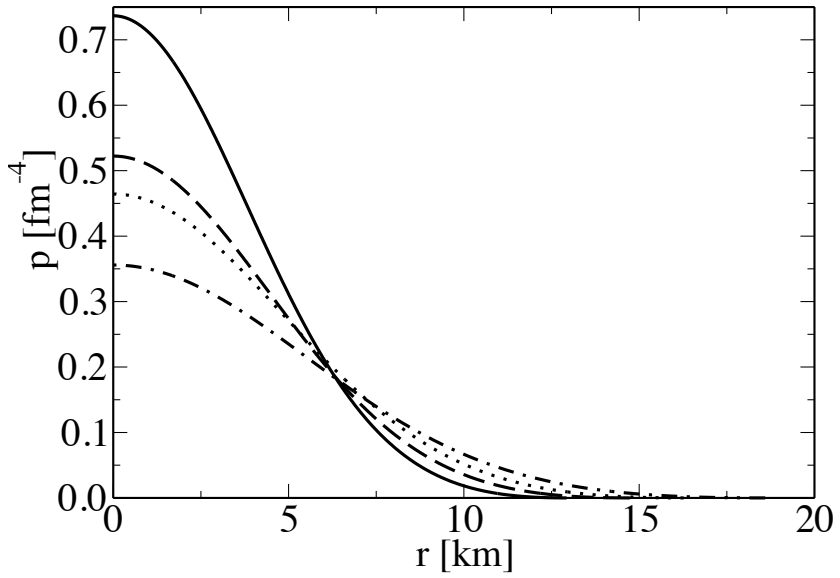

FIGURE 5.4 – Quark star profile for the maximum star mass of each parameterization. Pressure versus radial coordinate. Dot-dashed line: m = 300 MeV. Dotted line: m = 320 MeV. Dashed line: m = 340 MeV. Solid line: m = 360 MeV. Published in (ALEIXO *et al.*, 2024).

is expected.

It is interesting to note, as a curious result, that near a radius of 6.2 km and a pressure of approximately $0.2\,\mathrm{fm}^{-4}$, all the curves intersect at nearly the same point. Moreover, the behavior around this region appears to be almost independent of the mass parameter.

Another analysis can be done by using a profile diagram with the star mass along its radius. It is shown by figure 5.5 where we clearly see that mass and radius grow together up to their respective maxima. However, as the quark constituent mass m increases, both the maximum mass and corresponding radius decrease, indicating that lower values of m allow for more massive and larger stellar objects.

These four curves reach similar regions with different parameterizations. The curve with the parameterization $m = 360$ MeV approaches to the characteristic point where the neutron stars are defined, i.e., 10 km and 1.4 solar masses.

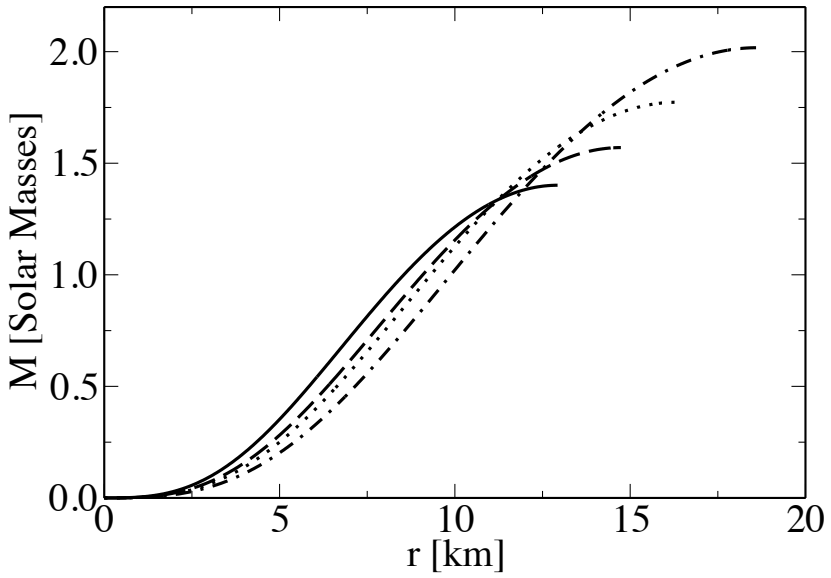

FIGURE 5.5 – Quark star profile for the maximum star mass of each parameterization. Mass inside a volume of radius r versus radial coordinate. Dot-dashed line: m = 300 MeV. Dotted line: m = 320 MeV. Dashed line: m = 340 MeV. Solid line: m = 360 MeV. Published in (ALEIXO *et al.*, 2024).

5.6 Tidal Deformability

After presenting the model and examining key features such as causality, stellar profiles, and the mass–radius relation, we now shift our focus to another fundamental property shaped by gravitational dynamics. The discussion that follows builds on the framework established in Section (3.4), where tidal deformability was introduced as a powerful probe of the internal structure of compact stars, particularly those in binary systems.

We use the available observational data to constrain the mass parameter m, which is present in the equation of state (5.4). As done previously in the mass–radius diagram analysis, we continue to restrict the mass parameter to the range from 300 MeV to 360 MeV. The result for the tidal deformability of the heavier companion in the binary system is shown in figure 5.6. The error bar presented on that figure is related to $\Lambda_{1.4} =$

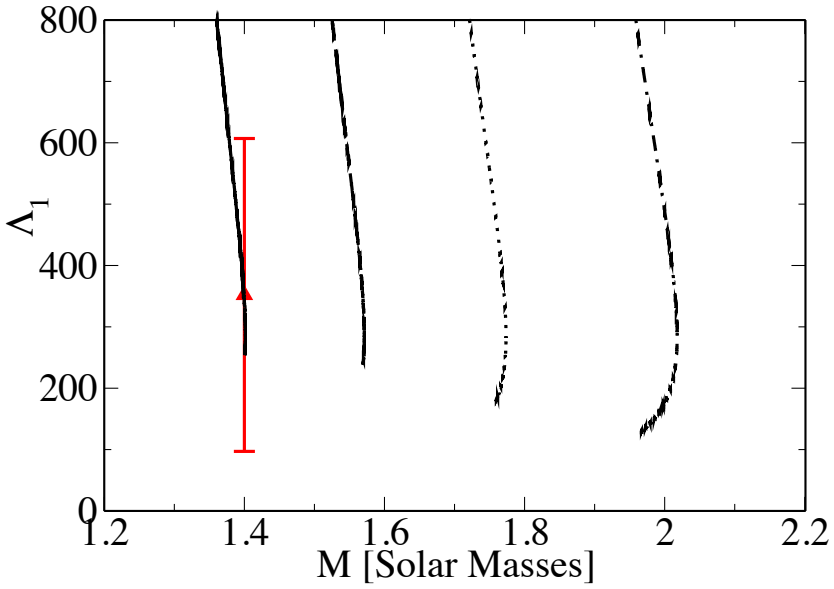

FIGURE 5.6 – The tidal deformability parameter for the heaviest companion of the neutron star binary system versus the total stellar mass for different values of m. Observational data from GW170817 event (ABBOTT *et al.*, 2017) (ABBOTT *et al.*, 2018) (ABBOTT *et al.*, 2019). Dot-dashed line: m = 300 MeV. Dotted line: m = 320 MeV. Dashed line: m = 340 MeV. Solid line: m = 360 MeV. Published in (ALEIXO *et al.*, 2024).

190^{+390}_{-120}, i.e., the tidal deformability that comes from the LIGO-VIRGO Collaboration on the event GW170817 (ABBOTT *et al.*, 2018). Therefore, it can be concluded from the figure that this dynamical property is consistent with the GW170817 event only when the quark mass parameter m in the D3–D7 holographic model is set to 360 MeV.

An interesting result is presented in figure 5.7. This diagram shows the relationship between two tidal deformability parameters Λ_1 and Λ_2 for binary compact stars mergers by using the **chirp mass** $1.188 M_\odot$ from the event GW170817 (LENZI *et al.*, 2023a). Λ_1 is related to the star with mass m_1 and Λ_2 to the star with mass m_2.

One can easily see in figure 5.7 that just one line is inside the 90% confidence level region according to the event GW170817. This line represents, in the current model, value equal to 360 MeV for the mass free parameter m that comes from the equation of state (5.4). Note that this value is compatible with the observational data region in the Figure

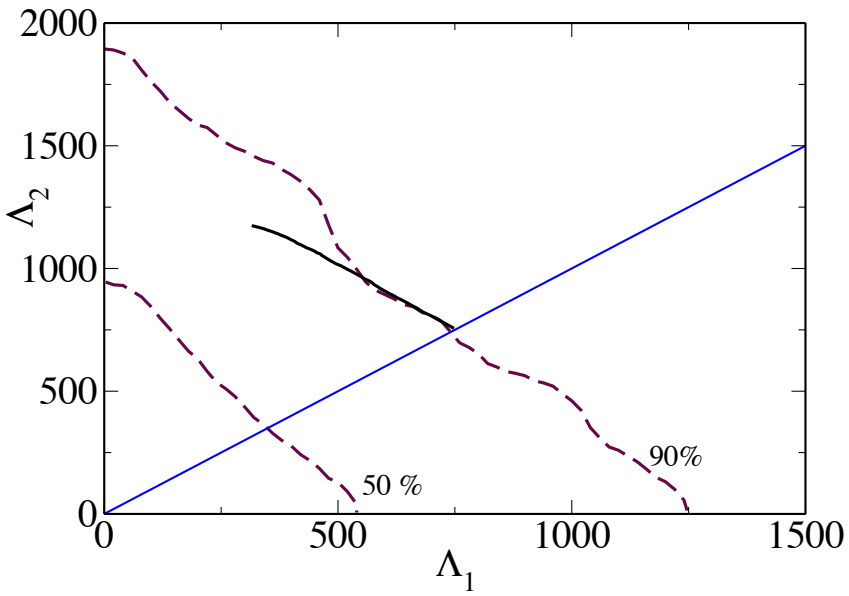

FIGURE 5.7 – Dimensionless tidal deformability parameters, Λ_1 and Λ_2, for binary compact star mergers computed using the chirp mass $1.188M_\odot$ of the GW170817 event for a constituent quark mass of 360 MeV within a holographic quark matter description (black solid line). The blue diagonal line is the identity ($\Lambda_1 = \Lambda_2$ boundary). The dashed brown curves denote the 50% and 90% LIGO-Virgo confidence levels determined by the event GW170817 in the low-spin prior scenario (ABBOTT *et al.*, 2017). Published in (ALEIXO *et al.*, 2024).

(5.6).

As shown in figures 5.6 and 5.7, when the quark mass parameter is set to $m = 360$ MeV, it becomes possible to reproduce the tidal deformability constraint observed in GW170817 event. However, as seen in the mass–radius diagram in Figure (5.2), this same mass configuration does not yield stellar masses near $2M_\odot$, a region for which observational data were obtained by NICER. We can thus conclude that quark stars composed of flavor-independent quark matter derived from the D3–D7 holographic model are not able to satisfy simultaneously the astrophysical bounds established by the LIGO–Virgo and NICER collaborations.

It is important to emphasize that quantum gravity effects emerging from the AdS/CFT framework may introduce small corrections to the thermodynamic quantities analyzed

here. These effects, including modifications to pressure and energy density, have been estimated to reach up to approximately 0.86%, and therefore are not expected to qualitatively alter our conclusions at the energy scales considered. Nonetheless, complementary methods such as the *configurational entropy* (ROCHA, 2021) (CASADIO *et al.*, 2023) approach and the *holographic entanglement entropy* (ROCHA, 2022) in QCD have been proposed as tools to further probe the stability and internal structure of compact stars. These techniques could provide additional insights, particularly in regimes where quantum corrections become non-negligible.

It is worth emphasizing that the analysis of the model across a range of constituent quark mass values m is tied to a particular choice for the 't Hooft coupling constant λ, which is commonly fixed using perturbative QCD results at high densities. However, this choice introduces a constraint that can be relaxed. If one does not impose this high-density matching condition, the equation of state (5.4) can alternatively be written as

$$\varepsilon = 3p + \frac{6m^2}{\sqrt{\lambda}\,\gamma^3}\sqrt{p}, \tag{5.14}$$

where the coefficient $\gamma = \Gamma(7/6)\Gamma(1/3)/\sqrt{\pi}$ is a numerical constant. In this form, the quark mass parameter m can be rescaled by varying the value of λ, meaning that the physical effects attributed to changing m can equivalently be interpreted as arising from variations in the 't Hooft coupling. This highlights a degree of degeneracy in the model's parameter space, emphasizing the need for care when interpreting the phenomenological role of m solely.

5.7 Summary

In this section we presented the preliminary results from the D3-D7 model applied to quark stars. We see that this model can describe phenomenological ranges according to the GW17081 event.

The free mass parameter m could help us find the best values to represent some dynamical properties such as tidal deformability and also exhibit the stars profiles to ensure that this approach can model as much as possible the structure of these systems.

As a natural extension of the present work, we suggest implementing this bottom-up model to investigate quark stars — and subsequently hybrid stars — with the goal of comparing the results and exploring features that might be inaccessible within the top-down framework. Such a comparative analysis could provide new insights into the equation of state and the phase structure of dense matter under extreme conditions. Furthermore, one could consider explicitly breaking the SU(3) flavor symmetry, allowing the quark mass parameter to vary across different flavors. This would result in a flavor-dependent model in which up, down, and strange quarks are treated with distinct masses. In such a scenario, the presence of electrons becomes essential to ensure full β-equilibrium and electric charge neutrality.

6 Hybrid Stars

This chapter presents a new application of the D3–D7 bottom-up holographic model in the astrophysical context, extending the analysis initiated in the previous chapter, where the model was first employed to describe pure quark stars. Here, we focus on conventional hybrid stars (HS) [1], compact objects composed of a quark matter core surrounded by a hadronic outer layer. The results discussed in this chapter are part of an original work currently under review, entitled *"Holographic hybrid stars with slow phase transitions"* (ALEIXO *et al.*, 2025).

In this study, the quark phase is described by the same D3–D7 holographic setup used previously, while the hadronic phase is modeled using the NL3* parameterization of a relativistic mean-field (RMF) theory. This RMF model is known for its ability to describe low-energy nuclear physics observables and to remain consistent with several astrophysical measurements. The hadron–quark phase transition is treated via a Maxwell construction, assuming a first-order transition and implementing the slow phase transitions regime.

The equation of state depends on a single free parameter in the quark sector—the constituent quark mass—which is varied between 300 and 390 MeV. Using the result-

[1] Alternative hybrid star configurations have been proposed in the literature. The HS2 model (ANNALA *et al.*, 2018) features an unconventional arrangement where a quark matter crust surrounds a hadronic core. This structure is similar to what is referred to in the literature as a cross star (or inverted hybrid star) (ZHANG; REN, 2023), where the usual layer ordering is reversed. The HS3 model, also from (ANNALA *et al.*, 2018), presents a more complex configuration in which a quark matter layer is sandwiched between hadronic phases, forming a hadron–quark–hadron structure.

ing hybrid EoS, we solve the Tolman–Oppenheimer–Volkoff equations, along with the radial oscillation equations, to investigate the stability and structure of the resulting stars. The mass–radius relations obtained for different parameter choices demonstrate that the model supports stable hybrid configurations with quark cores under slow phase transitions. All configurations analyzed produce maximum masses above two solar masses, in agreement with the observed properties of massive pulsars [2] such as PSR J1614–2230, PSR J0348+0432, and PSR J0740+6620. Additionally, the predicted stellar sequences fall within the 95% confidence intervals of NICER and XMM–Newton measurements for PSR J0740+6620 and NICER data for PSR J0030+0451.

An important outcome of this analysis is the observed correlation between the constituent quark mass and the compactness of the hybrid star core: increasing the quark mass leads to heavier and more compact cores. These results reinforce the applicability of the D3–D7 holographic model in the study of dense QCD matter inside compact stars and point toward future improvements, such as incorporating SU(3) flavor symmetry breaking and including beta equilibrium and electric charge neutrality in the quark phase.

6.1 Our holographic model

The hybrid star model employed in this work is constructed within a holographic framework, combining the D3/D7 brane setup to describe the quark matter sector and a relativistic mean-field (RMF) model to represent the hadronic phase. The two equations of state are matched via a first-order phase transition, as discussed earlier. In our numerical analysis, the constituent quark mass m is treated as a free parameter, allowing us to

[2] The naming convention PSR in pulsar cataloging refers to "Pulsating Source of Radio" and is typically followed by the coordinates of the source. For example, PSR J0740+6620 indicates a pulsar located at right ascension 07h40m and declination +66°20 (VERBIEST *et al.*, 2009).

investigate its impact on the macroscopic properties of hybrid stars.

Quark sector: D3/D7

For the quark sector, we adopt the D3/D7 holographic model previously introduced in Chapter (4) and applied to quark stars in Chapter (5). The corresponding equation of state is given by

$$\varepsilon(p) = 3p + \frac{2\sqrt{3}\,m^2}{\pi}\sqrt{p}, \tag{6.1}$$

where m is the constituent quark mass parameter. This EoS will now be used to model the quark core in hybrid stars.

Hadronic sector: NL3*

The hadronic model employed to construct our hybrid star configuration is based on a finite-range relativistic mean-field (RMF) approach formulated within the framework of Quantum Field Theory. Below, we outline the structure of the model used in the numerical analysis of the hybrid stars investigated in this work.

The Lagrangian density that describes the hadronic sector is given by (DUTRA *et al.*, 2014) (SUN *et al.*, 2024) (LI *et al.*, 2008)

$$\begin{aligned}\mathcal{L}_{had} = {} & \bar{\psi}(i\gamma^\mu\partial_\mu - M_{\text{nuc}})\psi + g_\sigma\sigma\bar{\psi}\psi - g_\omega\bar{\psi}\gamma^\mu\omega_\mu\psi \\ & - \frac{g_\rho}{2}\bar{\psi}\gamma^\mu\vec{b}_\mu\vec{\tau}\psi + \frac{1}{2}(\partial^\mu\sigma\partial_\mu\sigma - m_\sigma^2\sigma^2) - \frac{A}{3}\sigma^3 \\ & - \frac{B}{4}\sigma^4 - \frac{1}{4}F^{\mu\nu}F_{\mu\nu} + \frac{1}{2}m_\omega^2\omega_\mu\omega^\mu - \frac{1}{4}\vec{B}^{\mu\nu}\vec{B}_{\mu\nu} \\ & + \frac{1}{2}m_\rho^2\vec{b}_\mu\vec{b}^\mu.\end{aligned} \tag{6.2}$$

The nucleons and mesons are described by ψ, σ, ω^μ, and $\vec{b}_\mu$, with respective masses $M_{\rm nuc}$, m_σ, m_ω, and m_ρ. The field strength tensors are $F_{\mu\nu} = \partial_\mu\omega_\nu - \partial_\nu\omega_\mu$ and $\vec{B}_{\mu\nu} = \partial_\mu\vec{b}_\nu - \partial_\nu\vec{b}_\mu$. The coupling constants g_σ, g_ω, g_ρ, and self-interaction terms A, B are model parameters. We adopt the NL3* parameterization (LALAZISSIS *et al.*, 2009) due to its success in reproducing nuclear and neutron star properties. A broader analysis appears in (CARLSON *et al.*, 2023).

Within the mean-field approximation (DUTRA *et al.*, 2014) (LI *et al.*, 2008), the field equations are

$$m_\sigma^2\,\sigma = g_\sigma\rho_s - A\sigma^2 - B\sigma^3 \tag{6.3}$$

$$m_\omega^2\,\omega_0 = g_\omega\rho \tag{6.4}$$

$$m_\rho^2\,b_{0(3)} = \frac{g_\rho}{2}\rho_3 \tag{6.5}$$

$$[\gamma^\mu(i\partial_\mu - g_\omega\omega_0 - g_\rho b_{0(3)}\tau_3/2) - M^*]\psi = 0\,, \tag{6.6}$$

where the isospin projection τ_3 is $+1$ for protons and -1 for neutrons.

The effective nucleon mass is given by $M^* = M_{\rm nuc} - g_\sigma\sigma$. The densities are defined as

$$\rho_s = \rho_{s_p} + \rho_{s_n}, \qquad \rho = \rho_p + \rho_n, \qquad \rho_3 = (2y_p - 1)\rho \tag{6.7}$$

$$\rho_{s_{p,n}} = \frac{M^*}{\pi^2}\int_0^{k_{F_{p,n}}} \frac{k^2\,dk}{(k^2 + M^{*2})^{1/2}}\,, \tag{6.8}$$

where $k_{F_{p,n}} = (3\pi^2\rho_{p,n})^{1/3}$ and $y_p = \rho_p/\rho$.

The energy density and pressure are

$$\varepsilon_{had} = \sum_{i=p,n} \frac{1}{\pi^2} \int_0^{k_{F_i}} k^2 (k^2 + M^{*2})^{1/2} dk + g_\omega \omega_0 \rho + \frac{g_\rho}{2} b_{0(3)} \rho_3 + \frac{1}{2} m_\sigma^2 \sigma^2 + \frac{A}{3} \sigma^3 + \frac{B}{4} \sigma^4 - \frac{1}{2} m_\omega^2 \omega_0^2 - \frac{1}{2} m_\rho^2 b_{0(3)}^2 \tag{6.9}$$

$$p_{had} = \sum_{i=p,n} \frac{1}{3\pi^2} \int_0^{k_{F_i}} \frac{k^4 \, dk}{(k^2 + M^{*2})^{1/2}} + \frac{1}{2} m_\omega^2 \omega_0^2 + \frac{1}{2} m_\rho^2 b_{0(3)}^2 - \frac{1}{2} m_\sigma^2 \sigma^2 - \frac{A}{3} \sigma^3 - \frac{B}{4} \sigma^4 \tag{6.10}$$

Inclusion of electrons and muons under β-equilibrium gives

$$\rho_p - \rho_e = \rho_\mu, \qquad \mu_n - \mu_p = \mu_e = \mu_\mu \tag{6.11}$$

and modifies the thermodynamic quantities

$$\varepsilon_\beta = \varepsilon_{had} + \frac{\mu_e^4}{4\pi^2} + \frac{1}{\pi^2} \int_0^{\sqrt{\mu_\mu^2 - m_\mu^2}} k^2 (k^2 + m_\mu^2)^{1/2} dk \tag{6.12}$$

$$p_\beta = p_{had} + \frac{\mu_e^4}{12\pi^2} + \frac{1}{3\pi^2} \int_0^{\sqrt{\mu_\mu^2 - m_\mu^2}} \frac{k^4 \, dk}{(k^2 + m_\mu^2)^{1/2}} \tag{6.13}$$

with $m_\mu = 105.7$ MeV, and densities $\rho_e = \mu_e^3/(3\pi^2)$, $\rho_\mu = [(\mu_\mu^2 - m_\mu^2)^{3/2}]/(3\pi^2)$.

For completeness, the hadronic EoS also includes the crust: the outer crust follows the BPS model (BAYM *et al.*, 1971) in the range $6.3 \times 10^{-12}\,\mathrm{fm}^{-3} \leq \rho \leq 2.5 \times 10^{-4}\,\mathrm{fm}^{-3}$, while the inner crust is modeled by

$$p_{\mathrm{IC}} = \mathcal{A} + \mathcal{B} \varepsilon_{\mathrm{IC}}^{4/3} \tag{6.14}$$

with the transition to the core determined by the thermodynamical method (XU *et al.*, 2009b) (GONZALEZ-BOQUERA *et al.*, 2019) (XU *et al.*, 2009a).

6.2 Phase transition construction

In the context of hybrid star modeling, the phase transition between hadronic matter and deconfined quark matter is treated here as a first-order transition under the Maxwell construction. This approach imposes local charge neutrality and results in an abrupt isobaric transition, as discussed in section (3.2). The starting point of our analysis consists in plotting, from their respective equations of state, the pressure as a function of the baryonic chemical potential, $P(\mu)$, for both the hadronic and quark sectors. The intersection of these curves determines the transition point, ensuring that the conditions of mechanical and chemical equilibrium between the two phases are satisfied.

Figure 6.1 shows the relation between pressure and energy density in the phase transition region for each of the different hybrid configurations analyzed. By varying the flavor-independent constituent quark mass parameter m, one obtains six colored curves representing the quark sector of the hybrid configurations, while the solid black curve corresponds to the NL3* model used to describe the hadronic sector. All dashed lines indicate the phase transition region, characterized by the energy gap between the hadronic and quark phases. As can be seen in the diagram, there is a clear trend of increasing energy gap as the value of the constituent quark mass parameter m increases.

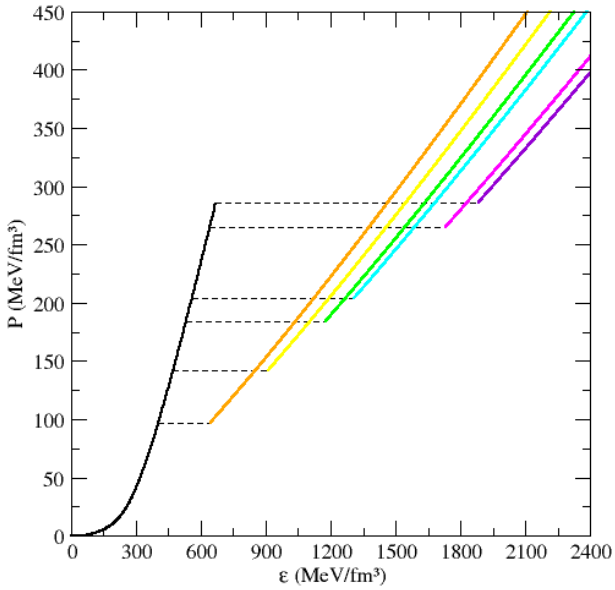

FIGURE 6.1 – Pressure as a function of the energy density for the hybrid equation of state obtained by combining the D3–D7 holographic model with the NL3* hadronic model, using the Maxwell construction to implement the phase transition. The black curve corresponds to the NL3* hadronic EoS. The colored curves represent the quark sector modeled holographically for different values of the constituent quark mass: $m = 300$ MeV (orange), $m = 320$ MeV (yellow), $m = 340$ MeV (green), $m = 350$ MeV (cyan), $m = 380$ MeV (pink), and $m = 390$ MeV (violet). Published in (ALEIXO *et al.*, 2025).

Table (6.1) presents the results obtained for the six analyzed configurations. We report the values of pressure and energy density, and explicitly show the variation in energy density across the phase transition region.

m (MeV)	**300**	**320**	**340**	**350**	**380**	**390**
$\boldsymbol{\Delta\varepsilon_t}$ (MeV/fm^3)	241.46	440.75	643.96	749.44	1091.40	1213.33
$\boldsymbol{\varepsilon_t}$ (MeV/fm^3)	403.24	472.41	531.44	558.87	640.59	668.30
$\boldsymbol{p_t}$ (MeV/fm^3)	97.18	142.25	183.79	204.17	265.36	286.00

TABLE 6.1 – Transition data for slow-stable configurations of HS using the D3-D7/NL3* model. The input is the constituent quark mass m in MeV. The following quantities are listed: ε_t indicates the density energy of the hadronic part where the phase transition starts, p_t is the corresponding transition pressure and $\Delta\varepsilon_t$ is the energy gap between the two phases. Published in (ALEIXO *et al.*, 2025).

6.3 Stability criteria

To analyze the stability of hybrid stars, we solve the system of radial oscillation equations originally formulated by Chandrasekhar (CHANDRASEKHAR, 1964). This approach investigates whether small radial perturbations can sustain stable stellar configurations. The key differential equations governing the radial oscillations are (CHANMUGAM, 1977)

$$\frac{d\xi}{dr} = -\frac{1}{r}\left(3\xi + \frac{\Delta p}{\Gamma p}\right) - \frac{dp}{dr}\frac{\xi}{(p+\varepsilon)}\,, \tag{6.15}$$

$$\begin{aligned}\frac{d\Delta p}{dr} = \xi\Bigg(&\omega^2 e^{\lambda-\nu}(p+\varepsilon)r - 4\frac{dp}{dr} + \left(\frac{dp}{dr}\right)^2 \frac{r}{(p+\varepsilon)} \\ &- 8\pi e^{\lambda}(p+\varepsilon)p\, r\Bigg) + \Delta p\left(\frac{dp}{dr}\frac{1}{(p+\varepsilon)} - 4\pi(p+\varepsilon)re^{\lambda}\right),\end{aligned} \tag{6.16}$$

In these equations, $\xi = \frac{\Delta r}{r}$ is the relative radial displacement, Δp is the Eulerian pressure perturbation, and the time dependence is assumed to be harmonic, i.e., $e^{i\omega t}$. The eigenfrequencies ω correspond to the normal modes of radial oscillation. For a stable configuration, one requires $\omega^2 > 0$. If $\omega^2 = 0$, the system reaches the onset of instability. In single-phase stars, this point usually corresponds to the maximum of the mass–central density relation, i.e., $\partial M/\partial\rho = 0$. However, in configurations with a first-order phase transition — especially those with slow conversion between phases at the interface — the fundamental mode can remain stable ($\omega^2 > 0$) even beyond the maximum mass point (LENZI *et al.*, 2023b) (LENZI *et al.*, 2023a) (PARISI *et al.*, 2021). This class of stars is referred to as *Slow Stable Hybrid Stars* (SSHSs) (LUGONES *et al.*, 2023).

A key quantity in this stability analysis is the *adiabatic index* Γ, which quantifies the stiffness of the equation of state in response to density perturbations. According to the

definition provided in (HAENSEL *et al.*, 2007), it is expressed as

$$\Gamma = \frac{n_b}{p}\frac{dp}{dn_b} = \frac{p+\varepsilon}{p}\frac{dp}{d\varepsilon}, \tag{6.17}$$

where n_b is the baryon number density, p the pressure, and ε the energy density. This index plays a central role in determining the star's response to radial perturbations: the larger the adiabatic index, the more resistant the matter is to compression, indicating a stiffer EoS. The functions $\nu(r)$ and $\lambda(r)$ in the equations are metric components obtained from solving the Tolman–Oppenheimer–Volkoff (TOV) equations. For further details, see Appendix (**E**).

6.4 Mass-Radius relation

Figure 6.2 shows the mass–radius (MR) relations obtained for the six hybrid star (HS) configurations analyzed in this work, each corresponding to a different value of the constituent quark mass m. The curves were computed up to the last stable configuration based on the condition $\omega_0^2 > 0$, assuming a slow first-order phase transition at the quark–hadron interface.

A key result is that, for all values of m, the holographic model predicts stable hybrid stars with maximum masses exceeding $2\,M_\odot$, consistent with the observed masses of heavy pulsars such as PSR J1614−2230, PSR J0348+0432, and PSR J0740+6620 (DEMOREST *et al.*, 2010) (ANTONIADIS *et al.*, 2013) (CROMARTIE *et al.*, 2019). Notably, for $m = 390$ MeV, the maximum stellar mass reaches $2.7\,M_\odot$.

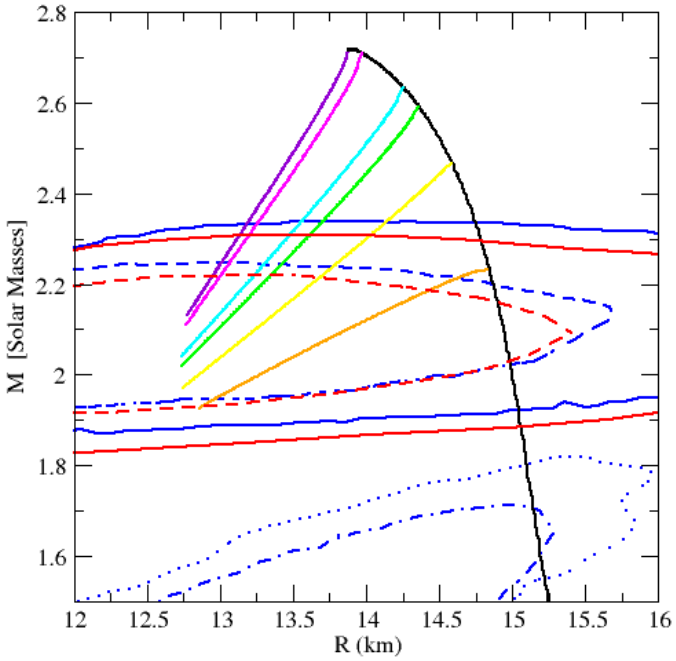

FIGURE 6.2 – Mass–radius diagram for hybrid stars based on the D3–D7/NL3* model. The solid and dashed red lines indicate the 95% confidence regions for the mass and radius of the pulsar PSR J0740+6620, as recently reported by the NICER and XMM-Newton collaboration (DITTMANN *et al.*, 2024). The blue contours correspond to NICER-only constraints: the solid and dashed lines refer to PSR J0740+6620 (MILLER *et al.*, 2021; RILEY *et al.*, 2021), while the dotted and dash-dotted lines represent the measurements for PSR J0030+0451 (MILLER *et al.*, 2019; RILEY *et al.*, 2019). In all cases, the inner and outer curves denote the 1σ and 2σ confidence intervals, respectively. The colored curves correspond to hybrid star configurations, with each color representing a different value of the constituent quark mass in the holographic quark sector: $m = 300$ MeV (orange), $m = 320$ MeV (yellow), $m = 340$ MeV (green), $m = 350$ MeV (cyan), $m = 380$ MeV (pink), and $m = 390$ MeV (violet). Published in (ALEIXO *et al.*, 2025).

The model also aligns well with recent constraints from the NICER+XMM-Newton collaboration (DITTMANN *et al.*, 2024). In particular, portions of the MR curves fall within the 95% confidence intervals for the masses and radii of the pulsars PSR J0740+6620 (MILLER *et al.*, 2021) (RILEY *et al.*, 2021) (CROMARTIE *et al.*, 2019) and PSR J0030+0451 (MILLER *et al.*, 2019) (RILEY *et al.*, 2019).

However, as shown in Fig.(5.6), none of the six configurations yield stable stars with masses near the canonical value of $1.4\,M_{\odot}$, a mass range particularly relevant for

binary neutron star systems, such as the one observed in the GW170817 event. This indicates that the present model does not reproduce the observational results reported by the LIGO–Virgo Collaboration for tidal deformability at lower masses (ABBOTT *et al.*, 2018). Nevertheless, it remains possible that future gravitational wave detections involving heavier binaries may fall within the range of validity of this model.

6.5 Sound velocity

The phase transition can be identified by the discontinuity in energy density, visible as a gap in the corresponding plot. Figure 6.3 illustrates the squared speed of sound, v_s^2, as a function of the energy density. A sharp drop in v_s^2 clearly marks the phase transition region, reflecting the change in the propagation medium due to latent heat release (LOPEOTER; LLANES-ESTRADA, 2022). The black curve corresponds to the hadronic phase, where v_s^2 reaches values close to 0.8, indicating a stiffer equation of state. In contrast, the colored curves represent the quark sector of the hybrid star for different values of the constituent quark mass, showing v_s^2 values ranging from approximately 0.2 to below 0.3—approaching the conformal limit of $v_s^2 = 1/3$.

Importantly, all curves respect the causality condition $v_s^2 < 1$, ensuring physical consistency. The comparatively lower values of v_s^2 in the quark sector highlight the greater compressibility of this phase. Physically, this contrast suggests that sound waves propagate more efficiently in the outer hadronic layer, which behaves more like a rigid material, whereas the quark matter core—where quark deconfinement occurs—exhibits a softer, more fluid-like nature.

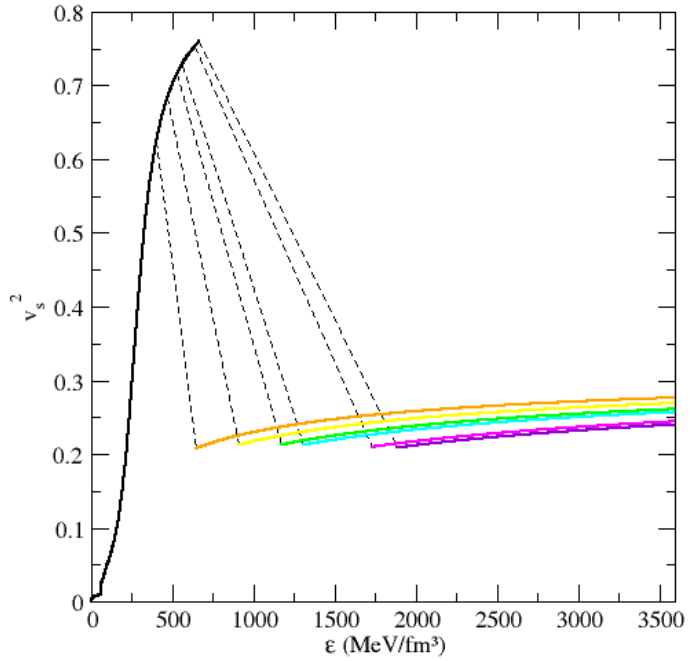

FIGURE 6.3 – Squared sound speed as function of the energy density for the D3-D7/NL3* model. The colored curves represent the quark sector modeled holographically for different values of the constituent quark mass: $m = 300$ MeV (orange), $m = 320$ MeV (yellow), $m = 340$ MeV (green), $m = 350$ MeV (cyan), $m = 380$ MeV (pink), and $m = 390$ MeV (violet). Published in (ALEIXO *et al.*, 2025).

6.6 Profiles

Figure 6.4 displays the radial pressure profiles for hybrid stars with a gravitational mass of $2.2M_{\odot}$, computed for each of the six constituent quark mass parameterizations used in this study. These profiles reveal how pressure is distributed from the stellar center to the surface. We obtained, as results, that configurations with higher values of the quark mass parameter exhibit larger central pressures. Specifically, the configuration with $m = 390$ MeV reaches the highest central pressure, while the lowest value is observed for $m = 300$ MeV.

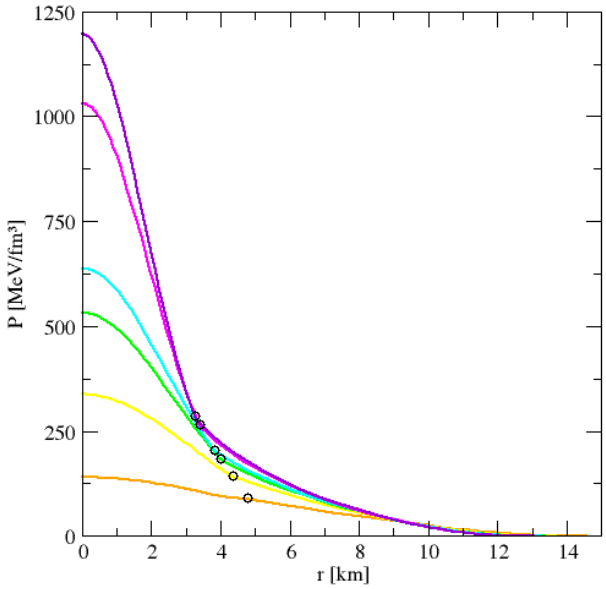

FIGURE 6.4 – Pressure versus radial coordinate of a hybrid star radial profiles for the 2.2 solar masses of each parameterization. The colored curves represent the quark sector modeled holographically for different values of the constituent quark mass: $m = 300$ MeV (orange), $m = 320$ MeV (yellow), $m = 340$ MeV (green), $m = 350$ MeV (cyan), $m = 380$ MeV (pink), and $m = 390$ MeV (violet). Published in (ALEIXO *et al.*, 2025).

One remarkable result we achieved with this study is the size of the quark core, i.e., the region where deconfined quark matter exists before transitioning to hadronic matter. The black circles overlaid on the curves indicate the radial positions at which the equation of state switches between the quark and hadronic phases—marking the interface where the phase transition occurs.

m **(MeV)**	$M_{\mathbf{core}}$ $(M/M_{\odot})$	$r_{\mathbf{core}}$ **(km)**
300	0.231	4.788
320	0.367	4.354
340	0.391	3.994
350	0.394	3.830
380	0.388	3.390
390	0.385	3.263

TABLE 6.2 – Quark core mass and radius for each parameterization for slow-stable configurations of 2.2 $M_{\odot}$ HS using the D3-D7/NL3* model.

As the constituent quark mass increases, not only does the central pressure rise, but the size of the quark core tends to shrink. This behavior is quantitatively summarized in Table (6.2), and, notably, shows an approximately linear trend.

7 Conclusion

The gauge/gravity duality has become a useful tool for investigating strongly coupled field theories. In this thesis, we discussed one model that represents an attempt to construct a QCD-like holographic model.

We saw in Chapter (4) a detailed construction of a generalized Dp-Dq holographic model. All the derivation considered only the supersymmetric intersection with the condition presented in equation (4.26). We finished this discussion with the free energy obtained from the Dirac-Born-Infeld (DBI) action. The connection was made by equation (4.55), when we recognized the regulated on-shell DBI action as the free energy.

The D3/D7 holographic model started by setting the values to specify the number of spatial dimensions of the branes. We have used in equation (4.60) the parameters that agree with (HOYOS *et al.*, 2016). After this process, by thermodynamical manipulations, we determine the equation of state, which is an input for the Tolman-Oppenheimer-Volkoff (TOV). We noticed that our equation had a parameter m, which is interpreted as the constituent quark mass and we used as a free parameter.

Moving forward in our study, we used the equation of state obtained from the holographic D3/D7 model to investigate properties of quark stars. Both the application and the results obtained were presented in Chapter (5). The study was conducted using four

parameterizations: 300, 320, 340, and 360 MeV.

From figure 5.1, we can conclude that the principle of causality is not violated, which ensures that the speed of sound propagation is always less than the speed of light. The static stability criterion (region where $\frac{\partial M}{\partial \epsilon_c} > 0$) adopted reveals, as illustrated in Figure (5.3), that all stellar configurations to the left of the circles representing the maximum mass are stable.

Figure 5.4, which shows how the pressure is distributed inside the quark star, allows us to conclude that the maximum central pressure occurs for the mass parameter equal to 360 MeV, while the minimum central pressure is reached when m is equal to 300 MeV. It is worth noting that there is a region in which the curves in this graph appear to converge to approximately the same point, allowing us to say that this specific region exhibits mass-independent behavior.

An additional result is shown in figure 5.5, which presents the mass distribution of quark star configurations for the maximum mass achieved for the four parameters in the study. From this diagram, we conclude that the radius of the maximum mass star decreases monotonically with the constituent quark mass parameter. Furthermore, from figures 5.2 and 5.6, we can conclude that, for the same constituent quark mass parameter, quark stars composed of flavor-independent quark matter are not able to simultaneously satisfy the astrophysical bounds set by LIGO-Virgo and NICER (ABBOTT *et al.*, 2020) (ABBOTT *et al.*, 2017) (ABBOTT *et al.*, 2018). We also present in figure 5.7 the tidal deformability result for binary compact star mergers, calculated using the chirp mass of $1.188 M_{\odot}$ from the GW170817 event defined by $\Lambda_{1.4} = 190^{+390}_{-120}$, for a constituent quark mass of 360 MeV within the holographic quark matter framework. We found that the parameterization $m = 360$ MeV was the most successful in remaining close to the 90%

confidence region based on the GW170817 event data (ABBOTT *et al.*, 2017).

As presented in Chapter (6), we used a quark model based on the D3/D7 brane configuration to build the holographic framework employed to investigate and obtain results for hybrid stars. The hadronic sector of the holographic model was described using a phenomenological relativistic mean-field model with finite range, known as NL3* (LALAZISSIS *et al.*, 2009), which is particularly advantageous due to its accurate ability to reproduce fundamental nuclear properties such as ground-state binding energies.

The phase transition region was determined from the $p \times \mu$ curve, which highlights the phase transition points through the intersection between the hadronic and quark curves for each of the constituent quark mass parameters used in this investigation. In this case, six different values were chosen for the constituent quark mass—our free parameter in the study: 300, 320, 340, 350, 380, and 390 MeV.

Figure 6.1 shows the energy gap in the phase transition region under the Maxwell construction (CONSTANTINOU *et al.*, 2023), which treats the first-order phase transition as an isobaric process. It can be seen that as the parameter m increases, both the energy gap and the transition pressure increase accordingly.

The causality condition was once again preserved, as supported by figure 6.3, which displays values below 1. It is also observed that there is a gap in the squared speed of sound, which tends to increase with increasing m. As the energy density increases, a slightly asymptotic behavior emerges, bringing the squared speed of sound closer to the conformal value of 1/3. This behavior suggests that wave propagation is easier in the hadronic region of the hybrid star, offering a physical insight analogous to the fact that mechanical waves propagate more efficiently in stiffer media.

The mass-radius diagram shown in figure 6.2 demonstrates that the holographic model developed is capable of producing massive stellar configurations. When the parameter m is 390 MeV, the stable configuration reaches up to 2.7 solar masses. It is important to emphasize here that stability is defined under a different criterion than that used for quark stars. We assumed that stable hybrid star configurations are determined according to the dynamic criterion of radial oscillations, which are obtained from the analysis of the eigenvalue spectrum. For all six parameter sets, the red curves indicate that each configuration falls within the 95% confidence interval according to recent NICER and XMM-Newton observational data for the pulsar PSR J0740+6620 (DITTMANN *et al.*, 2024).

Additionally, figure 6.4, which shows the pressure distribution inside a 2.2 solar mass hybrid star, reveals that an increase in the constituent quark mass leads directly to an increase in central pressure. Table (6.2) presents the values illustrating the size of the quark core. It is evident that the circles in the diagram representing the phase transition region display a linear trend, allowing us to conclude that increasing the constituent quark mass results in a progressively more compact core.

To further clarify the nature of the hadron–quark phase transition in hybrid stars, it is important to consider both the symmetry structure of the underlying models and the dynamical aspects of the transition. In our approach, hadrons are confined states described by a relativistic mean-field model, while deconfined quark matter is modeled using the holographic D3/D7 setup, where chiral symmetry is explicitly broken by a finite constituent quark mass. Although our model does not feature a dynamical order parameter such as the Polyakov loop or quark condensate, the phase transition is characterized by a discontinuity in energy density, signaling a first-order transition at zero temperature. The constituent quark mass, linked to the D7-brane embedding, directly

affects the stiffness of the quark matter equation of state and, consequently, the location of the transition. Moreover, while the conversion timescale across the hadron–quark interface remains uncertain due to the complexity of modeling nucleation processes, existing studies suggest that the transition may proceed slowly—particularly when compared to typical stellar oscillation periods.

As a continuation of the research presented in this thesis, we have begun a complementary investigation based on the Einstein–Maxwell–Dilaton (EMD) model (MAMANI *et al.*, 2020), which represents a bottom-up holographic framework. This alternative approach adopts a more phenomenological strategy by introducing a deformation of AdS space to construct a black hole geometry, thereby incorporating temperature through the presence of a horizon. Moreover, by including electric charge in the system, one can define a chemical potential via the holographic dictionary, enabling the construction of an equation of state for the quark sector. In this setup, the free parameter of the EMD model is directly related to the deformation of the AdS space and may offer access to physical features that remain beyond reach in the D3/D7 top-down model employed in the present work.

Simultaneously, we also identify a key improvement to the current holographic model: the inclusion of SU(3) flavor symmetry breaking in the quark sector. This enhancement would account for the distinct masses of up, down, and strange quarks. Furthermore, to accurately reflect the physical conditions inside compact stars, the inclusion of electrons is necessary to enforce beta equilibrium and electric charge neutrality in the quark phase. Together, these parallel efforts aim to construct a more realistic and comprehensive description of strongly interacting matter.

Bibliography

AARTS, G.; JAMES, F. A.; SEILER, E.; STAMATESCU, I.-O. Complex langevin dynamics: criteria for correctness. **Phys. Rev. D**, v. 85, n. 4, p. 045008, 2012.

ABBOTT, B. P.; ABBOTT, R.; ABBOTT, T. D.; ABERNATHY, M. R.; ACERNESE, F.; ACKLEY, K.; ADAMS, C.; ADAMS, T.; ADDESSO, P.; ADHIKARI, R. X. *et al.* Observation of gravitational waves from a binary black hole merger. **Physical Review Letters**, v. 116, n. 6, p. 061102, 2016.

ABBOTT, B. P.; ABBOTT, R.; ABBOTT, T. D.; ACERNESE, F.; ACKLEY, K.; ADAMS, C.; ADAMS, T.; ADDESSO, P.; ADHIKARI, R. X.; ADYA, V. B. *et al.* GW170817: Observation of gravitational waves from a binary neutron star inspiral. **Physical Review Letters**, v. 119, n. 16, p. 161101, 2017.

ABBOTT, B. P.; ABBOTT, R.; ABBOTT, T. D.; ACERNESE, F.; ACKLEY, K.; ADAMS, C.; ADAMS, T.; ADDESSO, P.; ADHIKARI, R. X.; ADYA, V. B. *et al.* GW170817: Measurements of neutron star radii and equation of state. **Physical Review Letters**, v. 121, n. 16, p. 161101, 2018.

ABBOTT, B. P.; ABBOTT, R.; ABBOTT, T. D.; ABRAHAM, S.; ACERNESE, F.; ACKLEY, K.; ADAMS, C.; ADHIKARI, R. X.; ADYA, V. B.; AFFELDT, C. *et al.* GW190425: Observation of a compact binary coalescence with total mass $3.4\ M_{\odot}$. **The Astrophysical Journal**, v. 892, n. 1, p. L3, 2020.

ABBOTT, B. P. *et al.* GWTC-1: A Gravitational-Wave Transient Catalog of Compact Binary Mergers Observed by LIGO and Virgo during the First and Second Observing Runs. **Physical Review X**, v. 9, n. 3, p. 031040, 2019.

ALCOCK, C.; FARHI, E.; OLINTO, A. Strange stars. **Astrophysical Journal**, v. 310, n. 1, p. 261–272, 1986.

ALEIXO, M.; LENZI, C.; DUTRA, M.; LOURENÇO, O.; PAULA, W. de. Holographic hybrid stars with slow phase transitions. **Physical Review D**, v. 111, n. 11, p. 116012, 2025.

ALEIXO, M.; LENZI, C. H.; PAULA, W. de; ROCHA, R. da. Quark stars in D_3–D_7 holographic model. **Eur. Phys. J. C**, v. 84, n. 3, p. 253, 2024.

ALFORD, M. G.; RAJAGOPAL, K.; WILCZEK, F. QCD at finite baryon density: Nucleon droplets and color superconductivity. **Phys. Lett. B**, v. 422, p. 247–256, 1998.

ALWIS, S. P. de. A note on brane tension and m-theory. **Physics Letters B**, v. 388, n. 2, p. 291–295, 1996.

AMMON, M.; ERDMENGER, J. **Gauge/Gravity Duality: Foundations and Applications**. Cambridge University Press, 2015. (Cambridge Monographs on Mathematical Physics). ISBN 978-1-107-01034-5. Available at: https://doi.org/10.1017/CBO9780511846373.

ANNALA, E.; ECKER, C.; HOYOS, C.; JOKELA, N.; FERNÁNDEZ, D. R.; VUORINEN, A. Holographic compact stars meet gravitational wave constraints. **JHEP**, v. 12, p. 078, 2018.

ANTONIADIS, J.; FREIRE, P. C. C.; WEX, N.; TAURIS, T. M.; LYNCH, R. S.; KERKWIJK, M. H. van; KRAMER, M.; BASSA, C.; DHILLON, V. S.; DRIEBE, T.; AL. et. A massive pulsar in a compact relativistic binary. **Science**, v. 340, p. 6131, 2013.

ARFKEN, G.; WEBER, H. H. **Física matemática: métodos matemáticos para engenharia e física**. [*S.l.: s.n.*], 2007. ISBN 9788535220506.

BALLON-BAYONA, A.; FREDERICO, T.; MAMANI, L. A. H.; PAULA, W. de. Dynamical holographic QCD model for spontaneous chiral symmetry breaking and confinement. **Physical Review D**, v. 108, n. 10, p. 106016, 2023.

BARDEEN, J. M.; THORNE, K. S.; MELTZER, D. W. A catalogue of methods for studying the normal modes of radial pulsation of general-relativistic stellar models. **Astrophysical Journal**, v. 145, p. 505–537, 1966. Available at: https://doi.org/10.1086/148791.

BAYM, G. *et al.* From hadrons to quarks in neutron stars: a review. 2017.

BAYM, G.; PETHICK, C.; SUTHERLAND, P. The ground state of matter at high densities: Equation of state and stellar models. **The Astrophysical Journal**, v. 170, p. 299–317, 1971.

BEDAQUE, P.; STEINER, A. W. Sound velocity bound and neutron stars. **Phys. Rev. Lett.**, v. 114, n. 3, p. 031103, 2015.

BEKENSTEIN, J. D. Black holes and entropy. **Physical Review D**, v. 7, n. 8, p. 2333–2346, 1973.

BERCHE, B.; KENNA, R.; WALTER, J. C. Hyperscaling above the upper critical dimension. **Nucl. Phys. B**, v. 865, p. 115–132, 2012.

BEZNOGOV, M. V.; YAKOVLEV, D. G. Diffusive heat blanketing envelopes of neutron stars. **Monthly Notices of the Royal Astronomical Society**, v. 459, n. 2, p. 1569–1579, 2016.

BHATTA, A.; CHAKRABORTTY, S.; MANDAL, T.; MAURYA, A. Holographic thermal correlators for hyperbolic CFT_s. **JHEP**, v. 11, p. 156, 2023.

BINNINGTON, T.; POISSON, E. Relativistic theory of tidal love numbers. **Physical Review D**, v. 80, n. 8, p. 084018, 2009.

BLUMENHAGEN, R.; LÜST, D.; THEISEN, S. **Basic Concepts of String Theory**. 1st. ed. [*S.l.: s.n.*], 2013. ISBN 978-3-642-29496-9. Available at: https://doi.org/10.1007/978-3-642-29497-6.

BODMER, A. R. Collapsed nuclei. **Physical Review D**, v. 4, n. 6, p. 1601–1606, set. 1971. Available at: https://link.aps.org/doi/10.1103/PhysRevD.4.1601.

BOMBACI, I.; PANDA, P. K.; PROVIDÊNCIA, C.; VIDAÑA, I. Metastability of hadronic compact stars. **Physical Review D**, v. 77, n. 8, p. 083002, 2008.

BOSCHI-FILHO, H.; BRAGA, N. R. F. Quantum fields in anti-de-sitter spacetime and degrees of freedom in the bulk/boundary correspondence. **Physics Letters B**, v. 505, n. 1–4, p. 263–266, 2001.

BOSCHI-FILHO, H.; BRAGA, N. R. F. Isometries of a D3-brane space. **Classical and Quantum Gravity**, v. 21, n. 9, p. 2427, 2004.

CAPLAN, M. E.; HOROWITZ, C. J. Colloquium : Astromaterial science and nuclear pasta. **Rev. Mod. Phys.**, v. 89, n. 4, p. 041002, 2017.

CARLSON, B. V.; DUTRA, M.; LOURENÇO, O.; MARGUERON, J. Low-energy nuclear physics and global neutron star properties. **Phys. Rev. C**, v. 107, n. 3, p. 035805, 2023.

CASADIO, R.; ROCHA, R. da; MEERT, P.; TABARRONI, L.; BARRETO, W. Configurational entropy of black hole quantum cores. **Class. Quant. Grav.**, v. 40, n. 7, p. 075014, 2023.

CASALDERREY-SOLANA, J.; LIU, H.; MATEOS, D.; RAJAGOPAL, K.; WIEDEMANN, U. A. **Gauge/String Duality, Hot QCD and Heavy Ion Collisions**. Cambridge: Cambridge University Press, 2014.

CASTRO, A.; PAULA, W. de; FREDERICO, T.; SALMÈ, G. Exploring the 0− bound state with dressed quarks in Minkowski space. **Phys. Lett. B**, v. 845, p. 138159, 2023.

CHAMEL, N. Superfluid density of neutrons in the inner crust of neutron stars: New life for pulsar glitch models. **Physical Review Letters**, v. 119, n. 6, p. 062701, 2017.

CHANDRASEKHAR, S. The maximum mass of ideal white dwarfs. **Astrophysical Journal**, v. 74, p. 81–82, 1931.

CHANDRASEKHAR, S. Dynamical instability of gaseous masses approaching the schwarzschild limit in general relativity. **Phys. Rev. Lett.**, v. 12, p. 114–116, 1964.

CHANMUGAM, G. Radial oscillations of zero-temperature white dwarfs and neutron stars below nuclear densities. **Astrophys. J.**, v. 217, p. 799–808, 1977.

CHATZIIOANNOU, K. Neutron-star tidal deformability and equation-of-state constraints. **General Relativity and Gravitation**, v. 52, n. 11, p. 109, 2020.

CHODOS, A.; JAFFE, R.; JOHNSON, K.; THORN, C.; WEISSKOPF, V. New extended model of hadrons. **Phys. Rev. D**, v. 9, p. 3471–3495, 1974. Available at: https://doi.org/10.1103/PhysRevD.9.3471.

COLEMAN, S. **Aspects of Symmetry**. [*S.l.: s.n.*], 1988. 401 p.

CONSTANTINOU, C.; ZHAO, T.; HAN, S.; PRAKASH, M. Framework for phase transitions between the Maxwell and Gibbs constructions. **Phys. Rev. D**, v. 107, n. 7, p. 074013, 2023.

CONTRERA, G. A.; ORSARIA, M.; RANEA-SANDOVAL, I. F.; WEBER, F. Hybrid Stars in the Framework of NJL Models. **Int. J. Mod. Phys. Conf. Ser.**, v. 45, p. 1760026, 2017.

CORLEY, S.; JACOBSON, T. Focusing and the holographic hypothesis. **Phys. Rev. D**, v. 53, p. R6720–R6724, 1996.

CRISTOFORETTI, M.; RENZO, F. D.; SCORZATO, L. New approach to the sign problem in quantum field theories: High density QCD on a lefschetz thimble. **Phys. Rev. D**, v. 86, p. 074506, 2012.

CROMARTIE, H. T. *et al.* Relativistic Shapiro delay measurements of an extremely massive millisecond pulsar. **Nature Astron.**, v. 4, n. 1, p. 72–76, 2019.

DAMOUR, T.; NAGAR, A. Relativistic tidal properties of neutron stars. **Physical Review D**, v. 80, n. 8, p. 084035, 2009.

DASGUPTA, K.; GALE, C.; MIA, M.; RICHARD, M.; TROTTIER, O. Vector meson spectrum from top-down holographic QCD. **Axioms**, v. 14, p. 66, 2025.

DEMOREST, P.; PENNUCCI, T.; RANSOM, S.; ROBERTS, M.; HESSELS, J. Shapiro Delay Measurement of A Two Solar Mass Neutron Star. **Nature**, v. 467, p. 1081–1083, 2010.

DEXHEIMER, V.; SCHRAMM, S. Proto-neutron and neutron stars in a chiral su(3) model. **The Astrophysical Journal**, v. 683, n. 2, p. 943, 2008.

DITTMANN, A. J. *et al.* A More Precise Measurement of the Radius of PSR J0740+6620 Using Updated NICER Data. **Astrophys. J.**, v. 974, n. 2, p. 295, 2024.

DUARTE, D. C.; FREDERICO, T.; PAULA, W. de; YDREFORS, E. Dynamical mass generation in Minkowski space at QCD scale. **Phys. Rev. D**, v. 105, n. 11, p. 114055, 2022.

DUTRA, M.; LOURENcO, O.; AVANCINI, S. S.; CARLSON, B. V.; DELFINO, A.; MENEZES, D. P.; PROVIDÊNCIA, C.; TYPEL, S.; STONE, J. R. Relativistic Mean-Field Hadronic Models under Nuclear Matter Constraints. **Phys. Rev. C**, v. 90, n. 5, p. 055203, 2014.

FILHO, K. de S. O.; SARAIVA, M. de F. O. **Astronomia e Astrofísica**. 4. ed. [*S.l.: s.n.*], 2017. ISBN 978-8578614850.

FODOR, Z.; KATZ, S. D. A new method to study lattice QCD at finite temperature and chemical potential. **Phys. Lett. B**, v. 534, p. 87–92, 2002.

FORCRAND, P. de. Simulating QCD at finite density. *In*: **Proceedings of the XXVII International Symposium on Lattice Field Theory (LAT2009)**. **Proceedings** [...]. [*S.l.: s.n.*], 2009. LAT2009, p. 010.

FREEDMAN, B. A.; MCLERRAN, L. D. Fermions and gauge vector mesons at finite temperature and density. iii. the ground-state energy of a relativistic quark gas. **Physical Review D**, v. 16, n. 4, p. 1169–1185, 1977.

FUKUSHIMA, K. Chiral effective model with the Polyakov loop. **Phys. Lett. B**, v. 591, p. 277–284, 2004. Available at: https://doi.org/10.1016/j.physletb.2004.04.027.

GLENDENNING, N. **Compact Stars: Nuclear Physics, Particle Physics, and General Relativity**. 2nd. ed. [*S.l.: s.n.*], 2000.

GLENDENNING, N. K.; MOSZKOWSKI, S. A. Reconciliation of neutron-star masses and binding of the λ in hypernuclei. **Physical Review Letters**, v. 67, n. 18, p. 2414–2417, 1991.

GONZALEZ-BOQUERA, C.; CENTELLES, M.; NAS, X. V.; ROUTRAY, T. R. Core-crust transition in neutron stars with finite-range interactions: The dynamical method. **Phys. Rev. C**, v. 100, n. 1, p. 015806, 2019.

GURSOY, U.; KIRITSIS, E. Exploring improved holographic theories for QCD: Part I. **JHEP**, v. 02, p. 032, 2008.

HAENSEL, P.; POTEKHIN, A. Y.; YAKOVLEV, D. G. **Neutron Stars 1: Equation of State and Structure**. 1st. ed. [*S.l.: s.n.*], 2007. ISBN 978-0-387-47301-7. Available at: https://doi.org/10.1007/978-0-387-47301-7.

HARRISON, B. K.; THORNE, K. S.; WAKANO, M.; WHEELER, J. A. **Gravitation Theory and Gravitational Collapse**. [*S.l.: s.n.*], 1965. ISBN 9780226318028.

HAWKING, S. W. Breakdown of predictability in gravitational collapse. **Physical Review D**, v. 14, n. 10, p. 2460–2473, 1976.

HINDERER, T. Tidal love numbers of neutron stars. **The Astrophysical Journal**, v. 677, n. 2, p. 1216, 2008.

HOOFT, G. A planar diagram theory for strong interactions. **Nuclear Physics B**, v. 72, n. 3, p. 461–473, 1974. ISSN 0550-3213. Available at: https://www.sciencedirect.com/science/article/pii/0550321374901540.

HOOFT, G. 't. Dimensional reduction in quantum gravity. *In*: **Conference Proceedings C**. **Proceedings** [...]. [*S.l.: s.n.*], 1993. v. 930308, p. 284–296.

HOOFT, G. 't. Quantum mechanics and determinism. *In*: **8th International Symposium on Particles, Strings and Cosmology**. **Proceedings** [...]. [*S.l.: s.n.*], 2001. p. 275–285.

HOOFT, G. 't. Quantization of space and time in 3 and in 4 space-time dimensions. *In*: **Quantum Fields and Quantum Space Time**. [*S.l.: s.n.*], 1997. p. 151–163.

HOROWITZ, C. J.; BERRY, D. K. The shear viscosity and thermal conductivity of nuclear pasta. **Phys. Rev. C**, v. 78, p. 035806, 2008.

HOROWITZ, C. J. *et al.* Neutrino-"pasta" scattering: The opacity of nonuniform neutron-rich matter. **Physical Review C**, v. 69, p. 045804, 2004.

HOROWITZ, C. J.; PIEKAREWICZ, J. Constraining urca cooling of neutron stars from the neutron radius of ^{208}pb. **Physical Review C**, v. 66, p. 055803, 2002.

HOYOS, C.; JOKELA, N.; FERNáNDEZ, D. R.; VUORINEN, A. Holographic quark matter and neutron stars. **Physical Review Letters**, v. 117, n. 3, 2016.

HøYE, G. K. **Oscillations in Neutron Stars**. Thesis (Doutorado) — Norwegian University of Science and Technology (NTNU), Trondheim, Norway, 1999.

ITSIOS, G.; JOKELA, N.; RAMALLO, A. V. Collective excitations of massive flavor branes. **Nuclear Physics B**, v. 909, p. 677–724, 2016.

JARVINEN, M.; KIRITSIS, E. Holographic Models for QCD in the Veneziano Limit. **JHEP**, v. 03, p. 002, 2012. Available at: https://doi.org/10.1007/JHEP03(2012)002.

KARAPETYAN, G.; PAULA, W. de; ROCHA, R. da. Configurational information measure of mesonic states in 4-flavor AdS/QCD. **Physics Letters B**, v. 846, p. 138174, 2023.

KARCH, A.; KATZ, E. Adding flavor to AdS/CFT. **Journal of High Energy Physics**, v. 2002, n. 06, p. 043, 2002.

KARCH, A.; KATZ, E.; SON, D. T.; STEPHANOV, M. A. Linear confinement and AdS/QCD. **Physical Review D**, v. 74, n. 1, p. 015005, 2006.

KARCH, A.; O'BANNON, A. Holographic thermodynamics at finite baryon density: some exact results. **Journal of High Energy Physics**, v. 2007, n. 11, p. 074–074, 2007.

KARCH, A.; SON, D. T.; STARINETS, A. O. Holographic quantum liquid. **Physical Review Letters**, v. 102, n. 5, p. 051602, 2009.

KATAGIRI, T.; IKEDA, T.; CARDOSO, V. Parametrized Love numbers of nonrotating black holes. **Phys. Rev. D**, v. 109, n. 4, p. 044067, 2024.

KLEBANOV, I. R.; STRASSLER, M. J. Supergravity and a confining gauge theory: Duality cascades and χsb-resolution of naked singularities. **Journal of High Energy Physics**, v. 2000, n. 08, p. 052, 2000.

KOGUT, J. B. The lattice gauge theory approach to quantum chromodynamics. **Reviews of Modern Physics**, v. 55, n. 3, p. 775–836, 1983.

LALAZISSIS, G.; KONIG, J.; RING, P. New parametrization for the Lagrangian density of relativistic mean field theory. **Phys. Rev. C**, v. 55, p. 540–543, 1997. Available at: https://doi.org/10.1103/PhysRevC.55.540.

LALAZISSIS, G. A.; KARATZIKOS, S.; FOSSION, R.; ARTEAGA, D. P.; AFANASJEV, A. V.; RING, P. The effective force NL3 revisited. **Phys. Lett. B**, v. 671, p. 36–41, 2009.

LATTIMER, J. M.; PRAKASH, M. Neutron star observations: Prognosis for equation of state constraints. **Physics Reports**, v. 442, n. 1–6, p. 109–165, 2007.

LENZI, C. H.; DUTRA, M.; LOURENÇO, O.; LOPES, L. L.; MENEZES, D. P. Dark matter effects on hybrid star properties. **The European Physical Journal C**, Springer, v. 83, n. 3, p. 266, 2023.

LENZI, C. H.; LUGONES, G.; VASQUEZ, C. Hybrid stars with reactive interfaces: Analysis within the nambu–jona-lasinio model. **Phys. Rev. D**, v. 107, p. 083025, 2023.

LI, B.-A.; CHEN, L.-W.; KO, C. M. Recent Progress and New Challenges in Isospin Physics with Heavy-Ion Reactions. **Phys. Rept.**, v. 464, p. 113–281, 2008.

LI, J. J.; SEDRAKIAN, A.; ALFORD, M. Relativistic Hybrid Stars with Sequential First-order Phase Transitions in Light of Multimessenger Constraints. **Astrophys. J.**, v. 944, n. 2, p. 206, 2023.

LOGOTETA, D.; BOMBACI, I. Constraints on Microscopic and Phenomenological Equations of State of Dense Matter from GW170817. **Universe**, v. 5, n. 10, p. 204, 2019.

LOPE-OTER, E.; LLANES-ESTRADA, F. J. Maximum latent heat of neutron star matter independently of General Relativity. **Phys. Rev. C**, v. 105, p. L052801, 2022.

LUGONES, G.; GRUNFELD, A. G. Phase Conversions in Neutron Stars: Implications for Stellar Stability and Gravitational Wave Astrophysics. **Universe**, v. 7, n. 12, p. 493, 2021.

LUGONES, G.; MARIANI, M.; RANEA-SANDOVAL, I. F. A model-agnostic analysis of hybrid stars with reactive interfaces. **JCAP**, v. 03, p. 028, 2023.

MALDACENA, J.; NUNEZ, C. Supergravity description of field theories on curved manifolds and a no go theorem. **International Journal of Modern Physics A**, v. 16, n. 05, p. 822–855, 2001.

MALDACENA, J. M. The Large N limit of superconformal field theories and supergravity. **Adv. Theor. Math. Phys.**, v. 2, p. 231–252, 1998.

MAMANI, L. A. H.; FLORES, C. V.; ZANCHIN, V. T. Phase diagram and compact stars in a holographic QCD model. **Physical Review D**, v. 102, n. 6, p. 066006, 2020.

MATEOS, D.; MYERS, R. C.; THOMSON, R. M. Thermodynamics of the brane. **Journal of High Energy Physics**, v. 2007, n. 05, p. 067, 2007.

MATHEW, A.; SHAFEEQUE, M.; NANDY, M. K. Stellar structure of quark stars in a modified starobinsky gravity. **The European Physical Journal C**, v. 80, n. 7, p. 615, 2020.

MATSUMOTO, M. Tricritical phenomena in holographic chiral phase transitions. **Journal of High Energy Physics**, v. 2022, n. 11, p. 1–34, 2022.

MCGREEVY, J. Holographic duality with a view toward many-body physics. **Adv. High Energy Phys.**, v. 2010, p. 723105, 2010.

MELTZER, D. W.; THORNE, K. S. Normal modes of radial pulsation of stars at the end point of thermonuclear evolution. **Astrophysical Journal**, v. 145, p. 514–529, 1966. Available at: https://doi.org/10.1086/148792.

MILLER, M. C.; LAMB, F. K.; DITTMANN, A. J.; BOGDANOV, S.; ARZOUMANIAN, Z.; GENDREAU, K. C.; GUILLOT, S.; HARDING, A. K.; HO, W. C. G.; LATTIMER, J. M.; AL. et. PSR J0030+0451 mass and radius from nicer data and implications for the properties of neutron star matter. **Astrophysical Journal Letters**, v. 887, n. 1, p. L24, 2019.

MILLER, M. C.; LAMB, F. K.; DITTMANN, A. J.; BOGDANOV, S.; ARZOUMANIAN, Z.; GENDREAU, K. C.; GUILLOT, S.; HO, W. C. G.; LATTIMER, J. M.; LOEWENSTEIN, M.; AL. et. The radius of PSR J0740+6620 from NICER and XMM-Newton Data. **Astrophysical Journal Letters**, v. 918, n. 2, p. L28, 2021.

NAKAHARA, M. **Geometry, Topology and Physics**. New York: Taylor Francis, 2003.

NAKAMURA, S. Comments on Chemical Potentials in AdS/CFT. **Prog. Theor. Phys.**, v. 119, p. 839–847, 2008.

NAKAZATO, K.; SUMIYOSHI, K.; YAMADA, S. Astrophysical implications of equation of state for hadron-quark mixed phase: Compact stars and stellar collapses. **Physical Review D**, v. 77, n. 10, p. 103006, 2008.

NAMBU, Y.; JONA-LASINIO, G. Dynamical model of elementary particles based on an analogy with superconductivity. I. **Phys. Rev.**, v. 122, p. 345–358, 1961. Available at: https://doi.org/10.1103/PhysRev.122.345.

NATSUUME, M. **AdS/CFT Duality User Guide**. 2016.

NEGREIROS, R.; DEXHEIMER, V. A.; SCHRAMM, S. Quark core impact on hybrid star cooling. **Physical Review C**, v. 85, n. 03, p. 035805, 2012.

NIJS, G.; SCHEIHING-HITSCHFELD, B.; YAO, X. Quarkonium transport in strongly coupled plasmas. *In*: **Proceedings of Hard Probes 2023**. **Proceedings** [...]. [*S.l.: s.n.*], 2024. HardProbes2023, p. 101.

OLIVEIRA, O.; SILVA, P. J.; SKULLERUD, J.-I.; STERNBECK, A. Quark propagator with two flavors of O(a)-improved Wilson fermions. **Phys. Rev. D**, v. 99, n. 9, p. 094506, 2019.

OPPENHEIMER, J. R.; VOLKOFF, G. M. On massive neutron cores. **Physical Review**, v. 55, n. 4, p. 374–381, 1939. Available at: https://link.aps.org/doi/10.1103/PhysRev.55.374.

ORTíN, T. **Gravity and Strings**. 2nd. ed. [*S.l.: s.n.*], 2015. (Cambridge Monographs on Mathematical Physics). ISBN 978-0-521-76813-9. Available at: https://doi.org/10.1017/CBO9781139019750.

PALHARES, L. F.; FRAGA, E. S. Surface tension in the cold and dense chiral transition and astrophysical applications. **PoS**, FACESQCD, p. 014, 2010.

PARISI, A.; FLORES, C. V.; LENZI, C. H.; CHEN, C.-S.; LUGONES, G. Hybrid stars in the light of the merging event GW170817. **Journal of Cosmology and Astroparticle Physics**, v. 2021, n. 06, p. 042, 2021.

PAULA, W. de; FREDERICO, T. Scalar mesons within a dynamical holographic QCD model. **Physics Letters B**, v. 693, p. 287–291, 2010.

PAULA, W. de; FREDERICO, T.; FORKEL, H.; BEYER, M. Dynamical AdS/QCD with area-law confinement and linear Regge trajectories. **Phys. Rev. D**, v. 79, p. 075019, 2009.

PAULA, W. de; FREDERICO, T.; SALMÈ, G.; VIVIANI, M. Advances in solving the two-fermion homogeneous bethe-salpeter equation in minkowski space. **Physical Review D**, v. 94, n. 7, p. 071901, 2016.

PAULA, W. de; JI, C.-R.; MELO, J. P. B. C. de; FREDERICO, T.; LOURENÇO, O. The holographic paradigm of hadron dynamics for medium modified nuclear matters. **Physics Letters B**, v. 803, p. 135339, 2020.

PEREIRA, J. P.; FLORES, C. V.; LUGONES, G. Phase transition effects on the dynamical stability of hybrid neutron stars. **Astrophys. J.**, v. 860, n. 1, p. 12, 2018.

PIEKAREWICZ, J. The nuclear physics of neutron stars. **arXiv preprint arXiv:2209.14877**, 2022.

POLCHINSKI, J. Dirichlet branes and ramond-ramond charges. **Physical Review Letters**, v. 75, n. 26, p. 4724–4727, 1995.

POLCHINSKI, J.; STRASSLER, M. J. Hard scattering and gauge/string duality. **Physical Review Letters**, v. 88, n. 3, p. 031601, 2002.

RAMALLO, A. V. Introduction to the AdS/CFT correspondence. **Springer Proc. Phys.**, v. 161, p. 411–474, 2015.

RAU, P. B.; SEDRAKIAN, A. Two first-order phase transitions in hybrid compact stars: Higher-order multiplet stars, reaction modes, and intermediate conversion speeds. **Phys. Rev. D**, v. 107, n. 10, p. 103042, 2023.

RILEY, T. E.; WATTS, A. L.; BOGDANOV, S.; RAY, P. S.; LUDLAM, R. M.; GUILLOT, S.; ARZOUMANIAN, Z.; BAKER, C. L.; BILOUS, A. V.; CHAKRABARTY, D.; AL. et. A NICER view of PSR J0030+0451: Millisecond pulsar parameter estimation. **Astrophysical Journal Letters**, v. 887, n. 1, p. L21, 2019.

RILEY, T. E.; WATTS, A. L.; RAY, P. S.; BOGDANOV, S. G. S.; MORSINK, S. M.; BILOUS, A. V.; ARZOUMANIAN, D. C. Z.; DENEVA, J. S.; AL. et. A NICER view of the massive pulsar PSR J0740+6620 informed by radio timing and XMM-Newton spectroscopy. **Astrophys. J. Lett.**, v. 918, n. 2, p. L27, 2021.

ROBERTS, C. D.; WILLIAMS, A. G. Dyson-schwinger equations and their application to hadronic physics. **Progress in Particle and Nuclear Physics**, v. 33, p. 477–575, 1994.

ROCHA, R. da. AdS graviton stars and differential configurational entropy. **Phys. Lett. B**, v. 823, p. 136729, 2021.

ROCHA, R. da. Holographic entanglement entropy, deformed black branes, and deconfinement in AdS/QCD. **Phys. Rev. D**, v. 105, n. 2, p. 026014, 2022.

RODRIGUEZ, M. C.; RANEA-SANDOVAL, I. F.; MARIANI, M.; ORSARIA, M. G.; MALFATTI, G.; GUILERA, O. M. Hybrid stars with sequential phase transitions: the emergence of the g_2 mode. **JCAP**, v. 02, p. 009, 2021.

ROMANI, R. W.; KANDEL, D.; FILIPPENKO, A. V.; BRINK, T. G.; ZHENG, W. PSR J0952−0607: The Fastest and Heaviest Known Galactic Neutron Star. **Astrophys. J. Lett.**, v. 934, n. 2, p. L17, 2022.

RYDER, L. H. **Quantum Field Theory**. 2nd. ed. Cambridge: Cambridge University Press, 1996. (Quantum Field Theory). ISBN 9780521478144.

SAKAI, T.; SUGIMOTO, S. Low energy hadron physics in holographic QCD. **Prog. Theor. Phys.**, v. 113, p. 843–882, 2005. Available at: https://doi.org/10.1143/PTP.113.843.

SCHERTLER, K.; GREINER, C.; SCHAFFNER-BIELICH, J.; THOMA, M. H. Quark phases in neutron stars and a 'third family' of compact stars as a signature for phase transitions. **Nucl. Phys. A**, v. 677, p. 463–490, 2000.

SCHWARTZ, M. D. **Quantum Field Theory and the Standard Model**. 1st. ed. Cambridge: Cambridge University Press, 2014. ISBN 978-1-107-03473-0.

SCHWARZSCHILD, K. On the gravitational field of a mass point according to einstein's theory. **Sitzungsberichte der Königlich Preußischen Akademie der Wissenschaften. Berlin. (Math. Phys.)**, v. 1916, p. 189–196, 1916.

SEIDOV, Z. F. The stability of a star with a phase change in general relativity theory. **Soviet Astronomy**, v. 15, p. 347, 1971.

SEN, A. Non-BPS D-branes in string theory. **Classical and Quantum Gravity**, v. 17, n. 5, p. 1251–1256, 2000.

SHAPIRO, S. L.; TEUKOLSKY, S. A. **Black Holes, White Dwarfs, and Neutron Stars: The Physics of Compact Objects**. 1. ed. Weinheim: WILEY-VCH Verlag GmbH & Co. KGaA, 2004.

SOTANI, H.; KUMAR, B. Universal relations between the quasinormal modes of neutron star and tidal deformability. **Phys. Rev. D**, v. 104, n. 12, p. 123002, 2021.

SPINELLA, W. M.; WEBER, F.; CONTRERA, G. A.; ORSARIA, M. G. Quark matter in neutron stars. *In*: **Discoveries at the Frontiers of Science**. Springer, 2020, (FIAS Interdisciplinary Science Series). p. 95–106. Available at: https://doi.org/10.1007/978-3-030-34234-0_9.

SUN, B.; BHATTIPROLU, S.; LATTIMER, J. M. Compiled properties of nucleonic matter and nuclear and neutron star models from nonrelativistic and relativistic interactions. **Phys. Rev. C**, v. 109, n. 5, p. 055801, 2024.

SUSSKIND, L. The world as a hologram. **Journal of Mathematical Physics**, American Institute of Physics, v. 36, n. 11, p. 6377–6396, 1995.

SUSSKIND, L.; WITTEN, E. **The Holographic bound in anti-de Sitter space**. may 1998. Available at: `https://arxiv.org/abs/hep-th/9805114`. Accessed on: 02 aug. 2025.

THORN, C. B. Reformulating string theory with the 1/n expansion. *In*: **The First International A.D. Sakharov Conference on Physics**. **Proceedings** [...]. [*S.l.: s.n.*], 1991. Available at: `https://arxiv.org/abs/hep-th/9405069`. Accessed on: 02 aug. 2025.

TOLMAN, R. C. Static solutions of einstein's field equations for spheres of fluid. **Phys. Rev.**, v. 55, n. 4, p. 364–373, 1939. Available at: https://link.aps.org/doi/10.1103/PhysRev.55.364.

VELTEN, H.; OLIVEIRA, A. M.; WOJNAR, A. A free parametrized tov: Modified gravity from newtonian to relativistic stars. **arXiv preprint arXiv:1601.03000**, 2016.

VERBIEST, J. P. W.; BAILES, M.; COLES, W. A.; HOBBS, G. B.; STRATEN, W. van; CHAMPION, D. J.; JENET, F. A.; MANCHESTER, R. N.; BHAT, N. D. R.; SARKISSIAN, J. M.; YARDLEY, D.; BURKE-SPOLAOR, S.; HOTAN, A. W.; YOU, X. P. Timing stability of millisecond pulsars and prospects for gravitational-wave detection. **Monthly Notices of the Royal Astronomical Society**, v. 400, n. 2, p. 951–968, 2009.

VOSKRESENSKY, D. N.; YASUHIRA, M.; TATSUMI, T. Charge screening at first order phase transitions and hadron–quark mixed phase. **Nucl. Phys. A**, v. 723, n. 1-2, p. 291–339, 2003. Available at: https://doi.org/10.1016/S0375-9474(03)01313-7.

WILSON, K. G. Confinement of Quarks. **Phys. Rev. D**, v. 10, p. 2445–2459, 1974. Available at: https://doi.org/10.1103/PhysRevD.10.2445.

WITTEN, E. Cosmic separation of phases. **Physical Review D**, v. 30, n. 2, p. 272–285, 1984.

WITTEN, E. Anti de Sitter space and holography. **Adv. Theor. Math. Phys.**, v. 2, p. 253–291, 1998.

WOOSLEY, S. E.; HEGER, A.; WEAVER, T. A. The evolution and explosion of massive stars. **Rev. Mod. Phys.**, v. 74, p. 1015–1071, 2002. Available at: https://doi.org/10.1103/RevModPhys.74.1015.

XU, J.; CHEN, L.-W.; LI, B.-A.; MA, H.-R. Locating the inner edge of neutron star crust using terrestrial nuclear laboratory data. **Phys. Rev. C**, v. 79, p. 035802, 2009.

XU, J.; CHEN, L.-W.; LI, B.-A.; MA, H.-R. Nuclear constraints on properties of neutron star crusts. **Astrophys. J.**, v. 697, p. 1549–1568, 2009.

ZAVLIN, V. E.; PAVLOV, G. G. Modeling neutron star atmospheres. **arXiv preprint astro-ph/0206025**, 2002.

ZEL'DOVICH, Y. B.; NOVIKOV, I. D. **Relativistic Astrophysics, Vol. 1: Stars and Relativity**. Chicago: University of Chicago Press, 1971. ISBN 9780226979557.

ZHANG, C.; REN, J. Hybrid stars may have an inverted structure. **Phys. Rev. D**, v. 108, n. 6, p. 063012, 2023.

ZHANG, L.; HUANG, M. Holographic cold dense matter constrained by neutron stars. **Phys. Rev. D**, v. 106, n. 9, p. 096028, 2022.

ZWIEBACH, B. **A First Course in String Theory**. 2nd. ed. Cambridge University Press, 2009. ISBN 978-0-521-88032-9. Available at: https://doi.org/10.1017/CBO9780511811233.

ÖZEL, F.; FREIRE, P. Masses, Radii, and the Equation of State of Neutron Stars. **Annual Review of Astronomy and Astrophysics**, v. 54, p. 401–440, 2016. Available at: https://doi.org/10.1146/annurev-astro-081915-023322.

Appendix A - Tension for Dq-brane

The tension on the Dq-brane is defined on the Polchinski's article (POLCHINSKI, 1995).

In article (ALWIS, 1996), we can find the equations (0.1) and (0.4). These equations can help us find the equation presented in (ITSIOS *et al.*, 2016)

$$T_{Dq} = \sqrt{\frac{2\pi\,(4\,\pi\,\alpha')^{\,3-p}}{2\,\kappa^2}} \tag{A.1}$$

$$2\,\kappa^2 = (2\pi)^3\,(2\,\pi\,\alpha')^4\,g_s^2, \tag{A.2}$$

where κ, related to the Newton's gravitational constant, is defined in terms of the Regge slope term and the effective string coupling g_s.

Replacing the last equation in the first one, we get

$$T_{Dq} = \sqrt{\frac{2\pi\,(4\,\pi^2\,\alpha')^{\,3-q}}{(2\pi)^3\,(2\,\pi\,\alpha')^4\,g_s^2}} = \frac{1}{\sqrt{(2\pi)^{2q}\,\alpha'^p\,\alpha'\,g_s^2}}$$

$$\boxed{T_{Dq} = \frac{1}{(2\pi)^q\,\sqrt{\alpha'}^{\,p+1}\,g_s}} \tag{A.3}$$

The dependence of the Dp-brane tension on the string length arises from dimensional analysis, considering that $\alpha' = l_s^2$, where l_s is the fundamental string length. The inverse dependence on the string coupling constant g_s is a common feature of solitonic objects in

quantum field theory (CASALDERREY-SOLANA *et al.*, 2014).

The perturbative limit is defined by taking $g_s \to 0$, in which case the brane tension becomes infinitely large. As a result, the D-brane becomes dynamically rigid and difficult to excite, allowing it to be treated as a fixed classical object—or defect—embedded in a static background.

A key difference between the tension of D-branes and that of typical solitons in quantum field theory lies in how they scale with the coupling constant. In conventional field theories, solitonic objects usually have tensions that scale as $1/g_s^2$. In contrast, the tension of D-branes scales as $1/g_s$.

This weaker dependence on the coupling indicates that D-branes are less massive than traditional solitons at weak coupling, which makes them more relevant in string theory even within the perturbative regime.

Appendix B - The Volume of S^{q-n-1}

The volume V_{q-n} for a sphere $\mathrm{S}^{\mathrm{q-n-1}}$ has the form

$$V_{q-n}\left(\mathrm{S}^{\,q-n-1}\right)=\frac{\pi^{\frac{q-n}{2}}}{\Gamma\left(\frac{q-n}{2}+1\right)}\,R^{\,q-n}. \tag{B.1}$$

Since the Euler's gamma exhibits the property $\Gamma(z+1)=z\,\Gamma(z)$, one can find the following expression

$$\Gamma\left(\frac{q-n}{2}+1\right)=\frac{q-n}{2}\;\Gamma\left(\frac{q-n}{2}\right) \tag{B.2}$$

Using this expression, we can get

$$\boxed{V_{q-n}\left(\mathrm{S}^{\,q-n-1}\right)=\frac{2\,\pi^{\frac{q-n}{2}}}{(q-n)\;\Gamma\left(\frac{q-n}{2}\right)}\,R^{\,q-n}.} \tag{B.3}$$

Using this expression we can find the explicit form for V_3, i.e., for the regular sphere defined in three dimensions

$$V_3\left(S^2\right)=\frac{2\,\pi^{\frac{3}{2}}}{3\;\Gamma\left(\frac{3}{2}\right)}\,R^{\,3}\;=\;\frac{4\,\pi\,R^3}{3}, \tag{B.4}$$

where we considered $\Gamma(\frac{1}{2})=\sqrt{\pi}$.

Appendix C - The derivation of the DBI term

To start the derivation of the DBI term we need to resume the definition of wedge product.

The **wedge product** or **exterior product** can be defined as follows.

Consider two 1-forms ω and η. They are defined by $\omega = \omega_i\, dx^i$ and $\eta = \eta_j\, dx^j$, respectively. The wedge product between them will be a 2-form

$$\begin{aligned}\omega \wedge \eta &= (\omega_i\, dx^i) \wedge (\eta_j\, dx^j) \\ &= (\omega_i\, \eta_j)\, dx^i \wedge dx^j \\ &= (\omega_i\, \eta_j)\, (dx^i \otimes dx^j - dx^j \otimes dx^i), \end{aligned} \tag{C.1}$$

where $\otimes$ is the tensor product. From this structure, it is easy to recognize the curl structure ($\vec{\nabla}\times$) between two vectors, by using the vectorial product.

Our target here is to prove the (4.20), i.e.

$$\sqrt{-\det(g + 2\,\pi\,\alpha'\,F)} = \rho^{\,q-n-1}\, g_{rr}^{\ \frac{q-n-1}{2}}\ g_{xx}^{\ \frac{n}{2}}\ \sqrt{(1+z'^2)\,|g_{tt}|\,g_{rr} - (2\,\pi\,\alpha'\,A_t')^2} \tag{C.2}$$

Let us start to draw a g matrix before constructing the gauge field F. The structure of this matrix comes from equation (4.12), i.e.

$$ds^2_{q+1} = g_{tt}(\rho)\, dt^2 + g_{xx}(\rho)\, [(dx^1)^2 + \cdots + (dx^n)^2] + \\ + g_{rr}(\rho)\, [(1 + z'^2)\, d\rho^2 + \rho^2 d\Omega^2_{q-n-1}] \tag{C.3}$$

Just to check: we have one term for the time component, n terms for common directions, one term for ρ with the multiplier $(1 + z'^2)$ and $q - n - 1$ for the last directions with the multiplier ρ^2.

The most general form of this matrix could be written as it follows

$$g = \begin{pmatrix} g_{tt} & & 0 & & 0 \\ & \overbrace{g_{xx} \quad \ddots \quad g_{xx}}^{n} & \vdots & & \\ 0 & \cdots & (1 + z'^2)\, g_{rr} & & \\ & & & \overbrace{\rho^2\, g_{rr} \quad \ddots \quad \rho^2\, g_{rr}}^{q-n-1} & \\ 0 & & & & \end{pmatrix} \tag{C.4}$$

Now we can focus on the gauge field F. It is defined by equation (4.14), that is

$$F = \frac{\partial A_t}{\partial \rho}\, d\rho \wedge dt = (\partial_\rho A_t)\ \ d\rho \wedge dt = A'_t\, d\rho \wedge dt \tag{C.5}$$

As we discussed above, the wedge product can be rewriten in a form

$$d\rho \wedge dt = d\rho \otimes dt \ - \ dt \otimes d\rho \tag{C.6}$$

Once we actually know that the general term "$dx \otimes dx$" will be always at a main diagonal of the metric tensor, the term "$dt \otimes d\rho$", for example, will be outside the main diagonal. It will be located in the line defined by "dt" and in the column defined by "$d\rho$".

Therefore, the gauge field on its matricial form is

$$F = \begin{pmatrix} 0 & & & A'_t & & 0 \\ & 0 & & \vdots & & \\ & & \ddots & \vdots & & \\ & & & 0 & & \\ -A'_t & & \dots & 0 & & \\ & & & & 0 & \\ & & & & & \ddots \\ 0 & & & & & 0 \end{pmatrix} \tag{C.7}$$

For this reason, the term inside the square root, $g + 2\pi\alpha' F$, can be written on that form

$$g + 2\pi\alpha' F = \begin{pmatrix} g_{tt} & & & 2\pi\alpha' A'_t & & 0 \\ & \overbrace{g_{xx} & & \vdots & & \\ & & \ddots & \vdots & & \\ & & g_{xx}}^{n} & & & \\ -2\pi\alpha' A'_t & & \dots & (1+z'^2)\, g_{rr} & & \\ & & & & \overbrace{\rho^2\, g_{rr} & & \\ & & & & & \ddots & \\ & & & & & & \rho^2\, g_{rr}}^{q-n-1} \\ 0 & & & & & & \end{pmatrix} \tag{C.8}$$

The next step is finding the determinant of this matrix. One can think that it is so hard because we do not have a specific number of n or $q - n - 1$ to do that. But there is one detail that help us find it with no other problems.

Let us simplify this matrix and try to calculate the determinant of M as follows

$$M = \begin{pmatrix} g_{tt} & 0 & 2\pi\alpha' A'_t & 0 \\ 0 & g_{xx} & 0 & 0 \\ -2\pi\alpha' A'_t & 0 & (1+z'^2)\, g_{rr} & 0 \\ 0 & 0 & 0 & \rho^2\, g_{rr} \end{pmatrix} \tag{C.9}$$

Choosing the term "a_{22}" to apply the Laplace's rule, we get

$$\det M = g_{xx} \cdot (-1)^{2+2} \det \begin{bmatrix} g_{tt} & 2\pi\alpha' A'_t & 0 \\ -2\pi\alpha' A'_t & (1+z'^2)\, g_{rr} & 0 \\ 0 & 0 & \rho^2 g_{rr} \end{bmatrix}$$

$$= g_{xx} \left((1+z'^2)\, \rho^2\, g_{rr}^2\, g_{tt} + (2\pi\alpha' A'_t)^2\, \rho^2\, g_{rr} \right) \tag{C.10}$$

We can try to extend this process to construct a new matrix N with a small change of this last one. This new matrix has the following form

$$N = \begin{pmatrix} g_{tt} & 0 & 0 & 2\pi\alpha' A'_t & 0 \\ 0 & g_{xx} & 0 & 0 & 0 \\ 0 & 0 & g_{xx} & 0 & 0 \\ -2\pi\alpha' A'_t & 0 & 0 & (1+z'^2)\, g_{rr} & 0 \\ 0 & 0 & 0 & 0 & \rho^2\, g_{rr} \end{pmatrix} \tag{C.11}$$

As we can easily see, this new matrix has a new g_{xx} term, and it will help us understand how the determinant will be modified by its introduction. Applying the Laplace's rule,

we get

$$\det N = g_{xx} \cdot (-1)^{2+2} \det \begin{bmatrix} g_{tt} & 0 & 2\pi\alpha' A'_t & 0 \\ 0 & g_{xx} & 0 & 0 \\ -2\pi\alpha' A'_t & 0 & (1+z'^2)\, g_{rr} & 0 \\ 0 & 0 & 0 & \rho^2 g_{rr} \end{bmatrix}. \tag{C.12}$$

But we can recognize that this matrix is the M matrix, as you can check with (C.9). Therefore, we actually know the result of the determinant. Then, we get

$$\det N = g_{xx} \cdot (-1)^{2+2} \underbrace{g_{xx} \left((1+z'^2)\, \rho^2\, g_{rr}^2\, g_{tt} + (2\pi\alpha' A'_t)^2\, \rho^2\, g_{rr} \right)}_{\text{determinant of M}} \tag{C.13}$$

Instead of adding a g_{xx} in M, one could add a $\rho^2\, g_{rr}$ term to form a new matrix T. The result would be

$$\det T = \rho^2\, g_{rr} \cdot (-1)^{j+j} \underbrace{g_{xx} \left((1+z'^2)\, \rho^2\, g_{rr}^2\, g_{tt} + (2\pi\alpha' A'_t)^2\, \rho^2\, g_{rr} \right)}_{\text{determinant of M}} \tag{C.14}$$

Note that the exponent of the *sign term* is "$j + j$". Even though we do not know about the order of the matrix, because this term is one of the $q - n - 1$ terms, we can say, precisely, that this term will be located at the main diagonal of the matrix and there, all the terms have the row number equals to the column number. It will always generate an **even number**, that is, a +1 sign.

Generalizing this discussion, the matrix Z assumes the form

$$Z = g + 2\pi\alpha' F = \begin{pmatrix} g_{tt} & & 2\pi\alpha' A'_t & & 0 \\ & \overbrace{g_{xx} \quad \ddots \quad g_{xx}}^{n} & \vdots & & \\ -2\pi\alpha' A'_t & \dots & (1+z'^2)\, g_{rr} & & \\ & & & \overbrace{\rho^2\, g_{rr} \quad \ddots \quad \rho^2\, g_{rr}}^{q-n-1} & \\ 0 & & & & \end{pmatrix} \tag{C.15}$$

whose determinant is

$$\det Z = {g_{xx}}^{n}\ (\rho^2)^{q-n-1}\ {g_{rr}}^{q-n-1}\ \left((1+z'^2)\, g_{rr}\, g_{tt} + (2\pi\alpha' A'_t)^2\right). \tag{C.16}$$

On the DBI action we have $\sqrt{-\det Z}$. There is just one more detail to finish this expression. The minus sign will act on the terms in parenthesis. The positive sign of the last term will be replaced by the minus sign, whereas the sign of the first term will be changed by the module of the time component, that is

$$\begin{aligned} \sqrt{-detZ} &= \sqrt{-\det(g + 2\,\pi\,\alpha'\,F)} \\ &= \sqrt{{g_{xx}}^{n}\ (\rho^2)^{q-n-1}\ {g_{rr}}^{q-n-1}\ ((1+z'^2)\, g_{rr}\, g_{tt} + (2\pi\alpha' A'_t)^2)} \\ &= \rho^{\,q-n-1}\, {g_{rr}}^{\frac{q-n-1}{2}}\ {g_{xx}}^{\frac{n}{2}}\ \sqrt{(1+z'^2)\,|g_{tt}|\, g_{rr} - (2\,\pi\,\alpha'\,A'_t)^2}. \end{aligned} \tag{C.17}$$

Therefore

$$\boxed{\sqrt{-\det(g + 2\,\pi\,\alpha'\,F)} = \rho^{\,q-n-1}\, {g_{rr}}^{\frac{q-n-1}{2}}\ {g_{xx}}^{\frac{n}{2}}\ \sqrt{(1+z'^2)\,|g_{tt}|\, g_{rr} - (2\,\pi\,\alpha'\,A'_t)^2}.} \tag{C.18}$$

Appendix D - Thermodynamic potential

Our objective here is to demonstrate the thermodynamic relation

$$P = -\mathcal{F}$$

Imagine you have a potential $y(x)$ and you want to create a new one with a new variable p. That new potential $\psi(p)$ can be found by applying the Legendre's transform (LT)

$$\psi(p) = y(x) - px \quad , \quad p = \frac{dy}{dx} \tag{D.1}$$

where x is the variable you want to remove and p is the new variable related to the old one from the derivative showed above.

With this discussion, one can construct many functions for thermodynamic potentials as we will do on the following.

We start with the energy U, i.e., a function of the entropy S, the volume V and the

number of particles N. One could write

$$U = U(S, V, N). \tag{D.2}$$

This energy has an important relation called Euler's relation, that is

$$U = TS - PV + \mu N \tag{D.3}$$

where T, P and μ are, respectively, the temperature, the pressure and the chemical potential.

To construct, for example, the Helmholtz free energy, we could apply the LT as it follows

$$\begin{aligned} F(T, V, N) &= U(S, V, N) - S \cdot \underbrace{\left(\frac{\partial U}{\partial S}\right)}_{=T} \\ &= U(S, V, N) - TS. \end{aligned} \tag{D.4}$$

We could do the same with the enthalpy $H(S, P, N)$ and the Gibbs's free energy $G(T, P, N)$. For the enthalpy that is the result

$$\begin{aligned} H(S, P, N) &= U(S, V, N) - V \cdot \underbrace{\left(\frac{\partial U}{\partial V}\right)}_{=-P} \\ &= U(S, V, N) + PV. \end{aligned} \tag{D.5}$$

Similarly, performing the LT twice, the Gibb's free energy is

$$G\left(T,P,N\right)=U\left(S,V,N\right)\ -\ S\cdot\underbrace{\left(\frac{\partial U}{\partial S}\right)}_{=T}-V\cdot\underbrace{\left(\frac{\partial U}{\partial V}\right)}_{=-P}$$

$$=\underbrace{U\left(S,V,N\right)\ +\ PV}_{\text{enthalpy: H(S,P,N)}}-TS. \tag{D.6}$$

There is another thermodynamic potential called **grand potential** (sometimes called Landau's free energy) Φ. That potential is so important in our study because it helps us build the equations of state.

Doing the same with the grand potential, after the LT we could get

$$\Phi\left(T,V,\mu\right)=U\left(S,V,N\right)\ -\ S\cdot\underbrace{\left(\frac{\partial U}{\partial S}\right)}_{=T}-N\cdot\underbrace{\left(\frac{\partial U}{\partial N}\right)}_{=\mu}$$

$$=U\left(S,V,N\right)\ -\ TS\ -\mu N. \tag{D.7}$$

From Euler's relation (D.3) one can write

$$U=TS-PV+\mu N$$

$$\Rightarrow\ U-TS+PV-\mu N=0 \tag{D.8}$$

If we compare it to equation (D.6), we can conclude

$$G-\mu N=0$$

$$\Rightarrow\ G=\mu N \tag{D.9}$$

Replacing Euler's relation into the grand potential equation (D.7), we get

$$\begin{aligned}\Phi &= U - TS - \mu N \\ &= (\cancel{TS} - PV + \cancel{\mu N}) - \cancel{TS} - \cancel{\mu N} \\ &= -PV \end{aligned} \tag{D.10}$$

Right now we have the structure to demonstrate the relation $P = -\mathcal{F}$.

We can start by using the last equation for Φ and divide this equation by the volume V, that is

$$\frac{\Phi}{V} = \frac{U}{V} - T\left(\frac{S}{V}\right) - \mu\left(\frac{N}{V}\right) = -P \tag{D.11}$$

We will redefine these quantities for

$$\frac{U}{V} \equiv \varepsilon \quad ; \quad \frac{S}{V} \equiv s \quad ; \quad \frac{N}{V} \equiv \rho, \tag{D.12}$$

being ε, s and ρ the energy density, the entropy density and the density related to the particle, respectively. And the grand potential Φ divided by the volume can be redefined in that form

$$\frac{\Phi}{V} \equiv \mathcal{F} \tag{D.13}$$

This equation can be rewriten as

$$\frac{\Phi}{V} = \mathcal{F} = \varepsilon - T\,s - \mu\,\rho = -P \tag{D.14}$$

As we can see

$$\boxed{\mathcal{F} = -P} \tag{D.15}$$

At a zero temperature, equation (D.14) becomes

$$-P = \varepsilon - \mu\,\rho \quad \Rightarrow \quad \varepsilon = \mu\,\rho - P \tag{D.16}$$

And as we can check from (D.14) and (D.15)

$$\rho = -\frac{\partial \mathcal{F}}{\partial \mu} = \frac{\partial P}{\partial \mu} \tag{D.17}$$

Therefore

$$\boxed{\varepsilon = \mu \left(\frac{\partial P}{\partial \mu}\right) - P} \tag{D.18}$$

Appendix E - The TOV equations

The Tolman-Oppenheimer-Volkoff equation (TOV) can describe the stars stability when considering hydrostatic equilibrium [1] . This construction is made by modelling a spherically symmetric body in static gravitational equilibrium.

In 1939, two articles appeared written by physicists Richard Tolman (TOLMAN, 1939), J. Robert Oppenheimer and George Volkoff (OPPENHEIMER; VOLKOFF, 1939). The articles basically presented a model capable of providing a super important equation for describing the stability of stars, whose deduction had a line element - static and more general - which contained a generalization of the metric proposed by Karl Schwarzschild (SCHWARZSCHILD, 1916).

The starting point to derive the TOV equations begins in the Einstein equation

$$R_{\mu\nu} - \frac{1}{2} g_{\mu\nu} R = \frac{8\pi G}{c^4} T_{\mu\nu}, \tag{E.1}$$

where $R_{\mu\nu}$ the Ricci tensor, R the scalar of curvature and $T_{\mu\nu}$, the momentum-energy

[1] This condition corresponds to a balance between the inward gravitational pull and the outward pressure generated by the matter inside the star. In other words, at each layer within the star, the pressure gradient is precisely enough to counteract the force of gravity. This construction is obtained by modeling a spherically symmetric body in static gravitational equilibrium.

tensor. The definition we are going to use is

$$R^{\lambda}_{\mu\rho\nu} = \partial_{\rho}\Gamma^{\lambda}_{\mu\nu} - \partial_{\nu}\Gamma^{\lambda}_{\mu\rho} + \Gamma^{\lambda}_{\sigma\rho}\Gamma^{\sigma}_{\mu\nu} - \Gamma^{\lambda}_{\sigma\nu}\Gamma^{\sigma}_{\mu\rho}; \tag{E.2}$$

$$R^{\lambda}_{\mu\lambda\nu} = R_{\mu\nu} = \partial_{\lambda}\Gamma^{\lambda}_{\mu\nu} - \partial_{\nu}\Gamma^{\lambda}_{\mu\lambda} + \Gamma^{\lambda}_{\sigma\lambda}\Gamma^{\sigma}_{\mu\nu} - \Gamma^{\lambda}_{\sigma\nu}\Gamma^{\sigma}_{\mu\lambda}; \tag{E.3}$$

$$R = g^{\mu\nu}R_{\mu\nu}; \tag{E.4}$$

$$T^{\nu\mu} = T^{\mu\nu} = (\varepsilon + P)\ u^{\mu}u^{\nu} - P\ g^{\mu\nu}. \tag{E.5}$$

The energy-momentum tensor $T_{\mu\nu}$ is the part of Einstein's equations that represents **matter**, unlike the R terms that are related to **geometry**. In the case of considering a perfect fluid - as will be done -, such tensor $T^{\mu\nu}$ assumes the form previously presented, where $\varepsilon = \rho c^2$ is the density of energy and P is the isotropic pressure exerted on the fluid.

There is a standard way to set this process. We consider the *co-motion*, that is, the frame is at rest with the matter where we can consider the four velocity such as $u^{\mu} = \frac{dx^{\mu}}{ds} = (1, 0, 0, 0)$. Being $g^{00} = 1$ and $g^{11} = g^{22} = g^{33} = -1$, the components of the energy-momentum tensor $T^{\mu\nu}$ can be calculated easily by the equation

$$T^{\mu\nu} = (\varepsilon + P)\ u^{\mu}u^{\nu} - P\ g^{\mu\nu}. \tag{E.6}$$

Doing that, we get

$$T^{00} = \varepsilon = \rho c^2 \quad ; T^{11} = T^{22} = T^{33} = P.$$

This space has a metric whose line element is a Schwarzschild generalization. The

most general possible form of this line element that preserves its spherical symmetry is

$$ds^2 = U(r)\,c^2\,dt^2 - V(r)\,dr^2 - W(r)r^2\,(d\theta^2 + \sin^2\theta\,d\phi^2). \tag{E.7}$$

Without loss of generality, one can choose the functions $U(r)$, $V(r)$ and $W(r)$. The choice is made respecting the positivity and monotonicity of the functions. The family of exponential functions guarantees that, externally, the time-like and space-like coordinates have their characteristics preserved. The line element takes the form

$$ds^2 = e^{\nu}\,c^2\,dt^2 - e^{\lambda}\,dr^2 - r^2\,(d\theta^2 + \sin^2\theta\,d\phi^2), \tag{E.8}$$

with ν and λ functions of r. That is, the metric tensor has the components

$$g_{00} = e^{\nu} \;\;;\;\; g_{11} = -e^{\lambda} \;\;;\;\; g_{22} = -r^2 \;\;;\;\; g_{33} = -r^2\sin^2\theta. \tag{E.9}$$

For simplicity, we will not present all the calculations of each Christoffel symbol and for the Ricci tensor. We will present just one example to be didactic. The Christoffel symbol has the form

$$\Gamma^{\sigma}_{\nu\mu} = \Gamma^{\sigma}_{\mu\nu} = \frac{1}{2}\,g^{\sigma\alpha}\,(\partial_{\mu}g_{\nu\alpha} + \partial_{\nu}g_{\mu\alpha} - \partial_{\alpha}g_{\mu\nu}). \tag{E.10}$$

One possible term could be

$$\Gamma^1_{01} = \Gamma^1_{10} = \frac{1}{2} g^{1\alpha} \left(\partial_1 g_{0\alpha} + \partial_0 g_{1\alpha} - \partial_\alpha g_{10} \right) \tag{E.11}$$

$$= \frac{1}{2} g^{11} (\cancel{\partial_1 g_{01}} + \partial_0 g_{11} - \cancel{\partial_1 g_{10}}) \tag{E.12}$$

$$= \frac{1}{2} g^{11} (\partial_0 g_{11}) \tag{E.13}$$

$$= 0. \tag{E.14}$$

To perform all the calculations of the Christoffel symbols it is necessary to consider that, for diagonal metrics, $g^{\mu\nu}$ is the inverse of $g_{\mu\nu}$ - the same as $g_{\mu\nu}\, g^{\mu\nu} = I$ (*identity*), whose explicit components are

$$g_{00} = e^{\nu} \;\; ; \;\; g_{11} = -e^{\lambda} \;\; ; \;\; g_{22} = -r^2 \;\; ; \;\; g_{33} = -r^2 \sin^2\theta; \tag{E.15}$$

$$g^{00} = e^{-\nu} \;\; ; \;\; g^{11} = -e^{-\lambda} \;\; ; \;\; g^{22} = -r^{-2} \;\; ; \;\; g^{33} = -r^{-2} \sin^{-2}\theta. \tag{E.16}$$

The non-zero terms of $\Gamma^{\sigma}_{\mu\nu}$ are

$$\Gamma^1_{00} = \frac{\nu'}{2}\, e^{\nu-\lambda} \;\; ; \;\; \Gamma^1_{11} = \frac{\lambda'}{2} \;\; ; \;\; \Gamma^1_{22} = -r\, e^{-\lambda} \;\; ; \;\; \Gamma^1_{33} = -r \sin^2\theta\, e^{-\lambda}; \tag{E.17}$$

$$\Gamma^0_{10} = \frac{\nu'}{2} \;\; ; \;\; \Gamma^2_{12} = \Gamma^3_{13} = \frac{1}{r} \;\; ; \;\; \Gamma^3_{23} = \cot\theta \;\; ; \;\; \Gamma^2_{33} = -\sin\theta\cos\theta, \tag{E.18}$$

where the prime ($'$) means the derivative with respect to r.

One can use equation (E.3) to calculate all the Ricci tensor components. It is important to highlight that all the components of the Ricci tensor outside the main diagonal are zero. Similarly, to be didactic we will calculate explicitly just one component of this

tensor. The component R_{11} is

$$
\begin{aligned}
R^{\lambda}_{\mu\rho\nu} &= \partial_\rho \Gamma^{\lambda}_{\mu\nu} - \partial_\nu \Gamma^{\lambda}_{\mu\rho} + \Gamma^{\lambda}_{\sigma\rho}\Gamma^{\sigma}_{\mu\nu} - \Gamma^{\lambda}_{\sigma\nu}\Gamma^{\sigma}_{\mu\rho};\\
R_{11} &= \partial_\lambda \Gamma^{\lambda}_{11} - \partial_1 \Gamma^{\lambda}_{1\lambda} + \Gamma^{\lambda}_{\sigma\lambda}\Gamma^{\sigma}_{11} - \Gamma^{\lambda}_{\sigma 1}\Gamma^{\sigma}_{1\lambda};\\
&= \partial_1 \Gamma^{1}_{11} - \partial_1 \Gamma^{0}_{10} - \partial_1 \Gamma^{1}_{11} - \partial_1 \Gamma^{2}_{12} - \partial_1 \Gamma^{3}_{13} + \Gamma^{0}_{\sigma 0}\Gamma^{\sigma}_{11} + \Gamma^{1}_{\sigma 1}\Gamma^{\sigma}_{11} +\\
&+ \Gamma^{2}_{\sigma 2}\Gamma^{\sigma}_{11} + \Gamma^{3}_{\sigma 3}\Gamma^{\sigma}_{11} - \Gamma^{0}_{\sigma 1}\Gamma^{\sigma}_{10} - \Gamma^{1}_{\sigma 1}\Gamma^{\sigma}_{11} - \Gamma^{2}_{\sigma 1}\Gamma^{\sigma}_{12} - \Gamma^{3}_{\sigma 1}\Gamma^{\sigma}_{13};\\
&= \cancel{\partial_1 \Gamma^{1}_{11}} - \partial_1 \Gamma^{0}_{10} - \cancel{\partial_1 \Gamma^{1}_{11}} - \partial_1 \Gamma^{2}_{12} - \partial_1 \Gamma^{3}_{13} + \Gamma^{0}_{10}\Gamma^{1}_{11} + \Gamma^{1}_{11}\Gamma^{1}_{11} +\\
&+ \Gamma^{2}_{12}\Gamma^{1}_{11} + \Gamma^{3}_{13}\Gamma^{1}_{11} - \Gamma^{0}_{01}\Gamma^{0}_{10} - \Gamma^{1}_{11}\Gamma^{1}_{11} - \Gamma^{2}_{21}\Gamma^{2}_{12} - \Gamma^{3}_{31}\Gamma^{3}_{13};
\end{aligned}
$$

Continuing the calculation, we have

$$
\begin{aligned}
R_{11} = &-\partial_1 \left(\Gamma^{0}_{10} + \Gamma^{2}_{12} + \Gamma^{3}_{13}\right) + \Gamma^{1}_{11}\left(\Gamma^{0}_{10} + \Gamma^{1}_{11} + \Gamma^{2}_{12} + \Gamma^{3}_{13}\right) +\\
&- \Gamma^{0}_{01}\Gamma^{0}_{10} - \Gamma^{1}_{11}\Gamma^{1}_{11} - \Gamma^{2}_{21}\Gamma^{2}_{12} - \Gamma^{3}_{31}\Gamma^{3}_{13}. \qquad \text{(E.19)}
\end{aligned}
$$

Using the already calculated components of the Christoffel symbol, we have

$$
\begin{aligned}
R_{11} &= -\frac{\partial}{\partial r}\left(\frac{\nu'}{2} + \frac{1}{r} + \frac{1}{r}\right) + \frac{\lambda'}{2}\left(\frac{\nu'}{2} + \frac{\lambda'}{2} + \frac{1}{r} + \frac{1}{r}\right) - \frac{\nu'}{2}\frac{\nu'}{2} - \frac{\lambda'}{2}\frac{\lambda'}{2} - \frac{1}{r}\frac{1}{r} - \frac{1}{r}\frac{1}{r};\\
\Rightarrow R_{11} &= -\frac{\nu''}{2} + \frac{\lambda'\nu'}{4} + \frac{\lambda'}{r} - \frac{\nu'^2}{4}. \qquad \text{(E.20)}
\end{aligned}
$$

The other non-zero components are

$$R_{00} = e^{\nu-\lambda}\left[\frac{\nu''}{2} - \frac{\lambda'\nu'}{4} + \frac{\nu'^2}{4} + \frac{\nu'}{r}\right]; \tag{E.21}$$

$$R_{22} = e^{-\lambda}\left(\frac{r\lambda'}{2} - \frac{r\nu'}{2} - 1\right) + 1; \tag{E.22}$$

$$R_{33} = R_{22}\sin^2\theta. \tag{E.23}$$

The curvature scalar R will be calculated by contracting the metric tensor with the Ricci tensor - tr $R_{\mu\nu} = R^{\mu}_{\ \mu}$ -, that is

$$\begin{aligned} R = g^{\mu\nu}R_{\mu\nu} &= g^{00}R_{00} + g^{11}R_{11} + g^{22}R_{22} + g^{33}R_{33} \\ &= e^{-\nu}R_{00} + \left(-e^{-\lambda}\right)R_{11} + \left(-\frac{1}{r^2}\right)R_{22} + \left(-\frac{1}{r^2\sin^2\theta}\right)R_{33} \\ &= e^{-\nu}R_{00} + \left(-e^{-\lambda}\right)R_{11} + \left(-\frac{2}{r^2}\right)R_{22}. \end{aligned} \tag{E.24}$$

After performing an algebraic manipulation and replacing the terms R_{00}, R_{11} and R_{22}, we can get

$$\begin{aligned} R &= e^{-\nu}\left[e^{\nu-\lambda}\left[\frac{\nu''}{2} - \frac{\lambda'\nu'}{4} + \frac{\nu'^2}{4} + \frac{\nu'}{r}\right]\right] + \left(-e^{-\lambda}\right)\left[-\frac{\nu''}{2} + \frac{\lambda'\nu'}{4} + \frac{\lambda'}{r} - \frac{\nu'^2}{4}\right] + \\ &\quad + \left(-\frac{2}{r^2}\right)\left[e^{-\lambda}\left(\frac{r\lambda'}{2} - \frac{r\nu'}{2} - 1\right) + 1\right]; \\ R &= e^{-\lambda}\left[\nu'' - \frac{\lambda'\nu'}{2} + \frac{\nu'^2}{2} + \frac{2}{r}(\nu' - \lambda') + \frac{2}{r^2}\right] - \frac{2}{r^2}. \end{aligned} \tag{E.25}$$

Now it is possible to calculate the Einstein equations, since all (the non-zero) terms of the Christoffel symbols, the Ricci tensor components and the curvature scalar have already been calculated. But there are still steps to be taken. To obtain such a conclusion, it is

enough to observe what was previously defined

$$T^{\mu\nu} = (\varepsilon + P)\ u^{\mu}u^{\nu} - P\ g^{\mu\nu}; \tag{E.26}$$

$$R_{\mu\nu} = \partial_{\lambda}\Gamma^{\lambda}_{\mu\nu} - \partial_{\nu}\Gamma^{\lambda}_{\mu\lambda} + \Gamma^{\lambda}_{\sigma\lambda}\Gamma^{\sigma}_{\mu\nu} - \Gamma^{\lambda}_{\sigma\nu}\Gamma^{\sigma}_{\mu\lambda}; \tag{E.27}$$

It is necessary to manipulate the indexes so that they are used in Einstein equations

$$R_{\mu\nu} - \frac{1}{2}g_{\mu\nu}R = \frac{8\pi G}{c^4}T_{\mu\nu}. \tag{E.28}$$

But what will be done to make it compatible? The metric tensor will be applied in the equation, transforming the (co- and contra-)variant tensors into mixed tensors.

Applying the metric tensor $g_{\sigma\nu}$ in the expression of $T^{\mu\nu}$, considering that $u^{\mu} = \frac{dx^{\mu}}{ds} = (1, 0, 0, 0)$ we have

$$g_{\sigma\nu}T^{\mu\nu} = T^{\mu}_{\sigma} = (\varepsilon + P)\ g_{\sigma\nu}\frac{dx^{\mu}}{ds}\frac{dx^{\nu}}{ds} - g_{\sigma\nu}\ g^{\mu\nu}P, \tag{E.29}$$

which leads to

$$T^{1}_{1} = (\varepsilon + P)\ \underbrace{g_{11}\frac{dx^{1}}{ds}\frac{dx^{1}}{ds}}_{=0} - \underbrace{g_{11}\ g^{11}}_{=1}P = -P. \tag{E.30}$$

Calculating analogously for the other components, the following results can be pre-

sented

$$T_0^0 = \varepsilon; \tag{E.31}$$

$$T_2^2 = T_3^3 = -P. \tag{E.32}$$

By applying the metric tensor $g^{\nu\sigma}$ in Einstein equations we obtain

$$g^{\nu\sigma}\ R_{\mu\nu} - \frac{1}{2} g^{\nu\sigma}\ g_{\mu\nu} R = \frac{8\pi G}{c^4} g^{\nu\sigma}\ T_{\mu\nu} = \frac{8\pi G}{c^4} T_\mu^\sigma. \tag{E.33}$$

Now it is necessary to calculate the terms for $\mu = \sigma = 0, 1, 2$ and 3.

$$\begin{aligned}
\frac{8\pi G}{c^4} T_0^0 &= g^{00}\ R_{00} - \frac{1}{2} \underbrace{g^{00}\ g_{00}}_{=1} R \\
&= e^{-\nu} \left[e^{\nu-\lambda} \left[\frac{\nu''}{2} - \frac{\lambda'\nu'}{4} + \frac{\nu'^2}{4} + \frac{\nu'}{r} \right] \right] \\
&- \frac{1}{2} \left[e^{-\lambda} \left[\nu'' - \frac{\lambda'\nu'}{2} + \frac{\nu'^2}{2} + \frac{2}{r} (\nu' - \lambda') + \frac{2}{r^2} \right] - \frac{2}{r^2} \right] \\
&\Rightarrow\ \frac{8\pi G}{c^4} T_0^0 = e^{-\lambda} \left(\frac{\lambda'}{r} - \frac{1}{r^2} \right) + \frac{1}{r^2}.
\end{aligned} \tag{E.34}$$

Repeating the procedure analogously, we obtain for the other components

$$\frac{8\pi G}{c^4} T_1^1 = -e^{-\lambda} \left(\frac{\nu'}{r} + \frac{1}{r^2} \right) + \frac{1}{r^2}; \tag{E.35}$$

$$\frac{8\pi G}{c^4} T_2^2 = \frac{8\pi G}{c^4} T_3^3 = -\frac{e^{-\lambda}}{2} \left(\nu'' + \frac{\nu'^2}{2} + \frac{\nu' - \lambda'}{r} - \frac{\nu'\lambda'}{2} \right), \tag{E.36}$$

and with

$$\frac{8\pi G}{c^4}T_0^0 = e^{-\lambda}\left(\frac{\lambda'}{r} - \frac{1}{r^2}\right) + \frac{1}{r^2}, \tag{E.37}$$

form the set of equations that will be used to find the TOV equations.

The Einstein equations obtained earlier for each component of the energy-momentum tensor are

$$\kappa\rho = e^{-\lambda}\left(\frac{\lambda'}{r} - \frac{1}{r^2}\right) + \frac{1}{r^2}; \tag{E.38}$$

$$\frac{\kappa P}{c^2} = e^{-\lambda}\left(\frac{\nu'}{r} + \frac{1}{r^2}\right) - \frac{1}{r^2}; \tag{E.39}$$

$$\frac{\kappa P}{c^2} = \frac{e^{-\lambda}}{2}\left(\nu'' + \frac{\nu'^2}{2} + \frac{\nu' - \lambda'}{r} - \frac{\nu'\lambda'}{2}\right). \tag{E.40}$$

where the energy density ε has been replaced by ρc^2 and $\kappa = \frac{8\pi G}{c^2}$. Doing (E.39) - (E.40) to eliminate P we have

$$e^{-\lambda}\left(\frac{\nu'}{r} + \frac{1}{r^2}\right) - \frac{1}{r^2} - \left[\frac{e^{-\lambda}}{2}\left(\nu'' + \frac{\nu'^2}{2} + \frac{\nu' - \lambda'}{r} - \frac{\nu'\lambda'}{2}\right)\right] = 0. \tag{E.41}$$

Multiplying the previous equation by e^{λ} we get

$$\left(\frac{\nu'}{r} + \frac{1}{r^2}\right) - \frac{e^{\lambda}}{r^2} - \left[\frac{1}{2}\left(\nu'' + \frac{\nu'^2}{2} + \frac{\nu' - \lambda'}{r} - \frac{\nu'\lambda'}{2}\right)\right] = 0. \tag{E.42}$$

Isolating the term with exponential in the previous equation

$$\frac{e^{\lambda}}{r^2} = \frac{\nu'\lambda'}{4} - \frac{\nu'^2}{4} - \frac{\nu''}{2} + \frac{\nu' + \lambda'}{2r} + \frac{1}{r^2}. \tag{E.43}$$

Doing (E.38) + (E.39), we have

$$\kappa\rho + \frac{\kappa P}{c^2} = e^{-\lambda}\left(\frac{\lambda'}{r} - \cancel{\frac{1}{r^2}}\right) + \cancel{\frac{1}{r^2}} + e^{-\lambda}\left(\frac{\nu'}{r} + \cancel{\frac{1}{r^2}}\right) - \cancel{\frac{1}{r^2}};$$
$$\kappa\left(\rho + \frac{P}{c^2}\right) = \frac{e^{-\lambda}}{r}\left(\nu' + \lambda'\right). \tag{E.44}$$

Differentiating equation (E.39) with respect to r, we have

$$\frac{d}{dr}\left(\frac{\kappa P}{c^2}\right) = \frac{d}{dr}\left[e^{-\lambda}\left(\frac{\nu'}{r} + \frac{1}{r^2}\right) - \frac{1}{r^2}\right];$$
$$\Rightarrow \frac{8\pi G}{c^4}\frac{dP}{dr} = \frac{2}{r^3} + e^{-\lambda}\left(-\frac{\lambda'}{r^2} - \frac{\lambda'\nu'}{r} - \frac{2}{r^3} + \frac{\nu''}{r} - \frac{\nu'}{r^2}\right). \tag{E.45}$$

Multiplying the equation (E.43) by $\frac{2e^{-\lambda}}{r}$, we get

$$\frac{2e^{-\lambda}}{r}\frac{e^{\lambda}}{r^2} = \frac{2e^{-\lambda}}{r}\left(\frac{\nu'\lambda'}{4} - \frac{\nu'^2}{4} - \frac{\nu''}{2} + \frac{\nu'+\lambda'}{2r} + \frac{1}{r^2}\right);$$
$$\Rightarrow \frac{2}{r^3} = e^{-\lambda}\left(\frac{\nu'\lambda'}{2r} + \frac{\nu'\lambda'}{2r} - \frac{\nu'\lambda'}{2r} - \frac{\nu'^2}{2r} - \frac{\nu''}{r} + \frac{\nu'+\lambda'}{r^2} + \frac{2}{r^3}\right);$$
$$\Rightarrow \frac{2}{r^3} = e^{-\lambda}\left(\frac{\nu'\lambda'}{r} - \frac{\nu'\lambda'}{2r} - \frac{\nu'^2}{2r} - \frac{\nu''}{r} + \frac{\nu'+\lambda'}{r^2} + \frac{2}{r^3}\right);$$
$$\Rightarrow 0 = -\frac{2}{r^3} - e^{-\lambda}\left(\frac{\nu'^2}{2r} + \frac{\nu'\lambda'}{2r}\right) - e^{-\lambda}\left(-\frac{\nu'\lambda'}{r} - \frac{(\nu'+\lambda')}{r^2} + \frac{\nu''}{r} - \frac{2}{r^3}\right).$$

One can rewrite equation (E.45) such as

$$\frac{8\pi G}{c^2}\left(\rho + \frac{P}{c^2}\right) = \frac{e^{-\lambda}}{r}\left(\nu' + \lambda'\right). \tag{E.46}$$

Adding the last two equations, we get

$$\frac{8\pi G}{c^4}\frac{dP}{dr} = -e^{-\lambda}\left(\frac{\nu'^2}{2r} + \frac{\nu'\lambda'}{2r}\right) = -\frac{\nu'}{2}\frac{e^{-\lambda}(\nu'+\lambda')}{r}. \tag{E.47}$$

But equation (E.44) is

$$\frac{8\pi G}{c^2}\left(\rho + \frac{P}{c^2}\right) = \frac{e^{-\lambda}}{r}\left(\nu' + \lambda'\right). \tag{E.48}$$

After comparing, one can get

$$\begin{aligned} &\frac{1}{c^2}\frac{8\pi\cancel{G}}{\cancel{c^2}}\frac{dP}{dr} = -\frac{\nu'}{2}\frac{8\pi\cancel{G}}{\cancel{c^2}}\left(\rho + \frac{P}{c^2}\right); \\ &\Rightarrow \frac{1}{c^2}\frac{dP}{dr} = -\frac{1}{2}\frac{d\nu}{dr}\left[\rho(r) + \frac{P(r)}{c^2}\right]. \end{aligned} \tag{E.49}$$

□

Equation (E.38) multiplied by r^2 becomes

$$\begin{aligned} &r^2\left(\frac{8\pi G}{c^2}\rho\right) = r^2\left[e^{-\lambda}\left(\frac{\lambda'}{r} - \frac{1}{r^2}\right) + \frac{1}{r^2}\right]; \\ &\Rightarrow \frac{8\pi G r^2}{c^2}\rho = e^{-\lambda}\left(\lambda' r - 1\right) + 1; \\ &\Rightarrow 1 - \frac{8\pi G r^2}{c^2}\rho = e^{-\lambda}\left(1 - \lambda'\, r\right). \end{aligned} \tag{E.50}$$

But observing the equality below

$$\frac{d}{dr}\left(r\; e^{-\lambda}\right) = e^{-\lambda} + r\;(-\lambda')\; e^{-\lambda} = e^{-\lambda}\;(1 - \lambda'\; r), \tag{E.51}$$

comparing, one gets

$$\frac{d}{dr}\left(r\ e^{-\lambda}\right) = 1 - \frac{8\pi G r^2}{c^2}\rho. \tag{E.52}$$

Integrating the previous expression with respect to $\tilde{r}$ we have

$$\begin{aligned}
&\int_0^r \frac{d}{d\tilde{r}}\left(\tilde{r}\ e^{-\lambda}\right) d\tilde{r} = \int_0^r \left(1 - \frac{8\pi G \tilde{r}^2}{c^2}\rho\right) d\tilde{r};\\
&\Rightarrow r\ e^{-\lambda} = r - \frac{2G}{c^2}\underbrace{\int_0^r 4\pi\tilde{r}^2\rho d\tilde{r}}_{=M_r};\\
&\Rightarrow e^{-\lambda} = 1 - \frac{2GM_r}{rc^2},
\end{aligned} \tag{E.53}$$

where we have considered

$$\frac{dM_r}{dr} = 4\pi r^2 \rho(r). \tag{E.54}$$

The term M_r is the gravitational mass within r related to the continuity equation describing the stellar structure. So in the limit where $r \to R$, $M_r \to M$, that is, M becomes the gravitational mass of the star obtained by a distant observer via, for example, orbit effects.

Rewriting equation (E.49) we have

$$\begin{aligned}
&\frac{1}{c^2}\frac{dP}{dr} = -\frac{1}{2}\frac{d\nu}{dr}\left[\rho(r) + \frac{P(r)}{c^2}\right];\\
&\Rightarrow \frac{d\nu}{dr} = -2\ \frac{dP}{dr}\left(\frac{1}{\rho c^2 + P}\right).
\end{aligned} \tag{E.55}$$

Using the previous equation in equation (E.39) we get

$$\frac{8\pi GP}{c^4} = e^{-\lambda}\left[-\frac{2}{r}\,\frac{dP}{dr}\left(\frac{1}{\rho c^2 + P}\right) + \frac{1}{r^2}\right] - \frac{1}{r^2}. \tag{E.56}$$

And using what was obtained in equation (E.53), we find

$$\frac{8\pi GP}{c^4} = \left(1 - \frac{2GM_r}{rc^2}\right)\left[-\frac{2}{r}\,\frac{dP}{dr}\left(\frac{1}{\rho c^2 + P}\right) + \frac{1}{r^2}\right] - \frac{1}{r^2}. \tag{E.57}$$

Manipulating only algebraically the previous equation, it is possible to find the long-awaited Tolman-Oppenheimer-Volkoff equation

$$\boxed{\frac{dP}{dr} = -\frac{GM_r\rho}{r^2}\left(1 + \frac{4\pi r^3 P}{M_r c^2}\right)\left(1 + \frac{P}{\rho c^2}\right)\left(1 - \frac{2GM_r}{rc^2}\right)^{-1}.} \tag{E.58}$$

That equation with (E.54) and (E.55) form the set of equations which is responsible to describe the stars hydrostatic equilibrium.

A quick and important consideration that can be made through this last equation is to analyze the limit in which $c^2 \to \infty$, leaving only

$$\frac{dP}{dr} = -\frac{GM_r\rho}{r^2}, \tag{E.59}$$

which recovers the condition of Newtonian hydrostatic equilibrium.

FOLHA DE REGISTRO DO DOCUMENTO

1. CLASSIFICAÇÃO/TIPO	2. DATA	3. REGISTRO N°	4. N° DE PÁGINAS
TD	08 de agosto de 2025	DCTA/ITA/TD-033/2025	205

5. TÍTULO E SUBTÍTULO:

Compact stars properties from a D3/D7 holographic model.

6. AUTOR(ES):

Michael Aleixo dos Santos

7. INSTITUIÇÃO(ÕES)/ÓRGÃO(S) INTERNO(S)/DIVISÃO(ÕES):

Instituto Tecnológico de Aeronáutica – ITA

8. PALAVRAS-CHAVE SUGERIDAS PELO AUTOR:

Modelos Holográficos; Estrelas Híbridas; Objetos Compactos.

9.PALAVRAS-CHAVE RESULTANTES DE INDEXAÇÃO:

Estrelas compactas; Matéria de quark; Equações de estado; Estruturas híbridas; Física nuclear; Física.

10. APRESENTAÇÃO: **(X) Nacional ( ) Internacional**

ITA, São José dos Campos. Curso de Doutorado. Programa de Pós-Graduação em Física. Área de Física Nuclear. Orientador: Prof. Dr. Wayne Leonardo Silva de Paula; coorientador: Prof Dr. José Abdalla Helayel Neto. Defesa em 07/07/2025. Publicada em 2025

11. RESUMO:

The behavior of nuclear matter at extreme densities remains one of the most compelling frontiers in modern astrophysics. This work investigates compact star configurations composed of quark matter within the framework of the AdS/CFT holographic correspondence, employing a flavor-independent top-down D3/D7 holographic model. The study focuses on two types of compact objects: pure quark stars and hybrid stars with quark cores, incorporating dynamical stability criteria and comparisons with recent observational constraints. In the case of pure quark stars, the equation of state is derived from the holographic model, with the constituent quark mass treated as a free parameter. While the resulting stable configurations reach high masses consistent with some observational bounds, they fail to simultaneously satisfy the tidal deformability limits inferred from the GW170817 event. As a second application, we investigate hybrid stars composed of a hadronic crust — described by the NL3* parameterization of the relativistic mean-field model — and a deconfined quark core governed by the same flavor-independent holographic model. Assuming slow, first-order phase transitions and adopting the Maxwell construction, we perform a dynamical stability analysis based on radial oscillations. The results reveal stable hybrid star configurations with quark cores, reaching maximum masses near 2.7 solar masses. Among the most significant outcomes are the compatibility with observational mass-radius relations, the preservation of causality, and the estimation of quark core sizes.

12. GRAU DE SIGILO:

(X) OSTENSIVO **( ) RESERVADO** **( ) SECRETO**